Adaptive Servo Schemes using Micromachined Accelerometers for Increased Disturbance Rejection for Magnetic Hard Disk Drives

by

Satinderpall Singh Pannu

B.S. (University of California, Berkeley) 1992
M.S. (University of California, Berkeley) 1994

A dissertation submitted in partial satisfaction of the

requirements for the degree of

Doctor of Philosophy

in

Engineering - Mechanical Engineering

in the

GRADUATE DIVISION

of the

UNIVERSITY of CALIFORNIA, BERKELEY

Comittee in charge:

Professor Roberto Horowitz
Professor Albert P. Pisano
Professor Roger T. Howe

Spring 1998

The dissertation of Satinderpall Singh Pannu is approved:

Professor Roberto Horowitz, Chair	Date
Professor Albert P. Pisano	Date
Professor Roger T. Howe	Date

University of California, Berkeley

1998

Adaptive Servo Schemes using Micromachined Accelerometers for Increased Disturbance Rejection for Magnetic Hard Disk Drives

by

Satinderpall Singh Pannu

Abstract

Adaptive Servo Schemes using Micromachined Accelerometers for Increased Disturbance Rejection for Magnetic Hard Disk Drives

by

Satinderpall Singh Pannu

Doctor of Philosophy in Mechanical Engineering

University of California, Berkeley

Professor Roberto Horowitz, Chair

Hard disk drive track widths of 1 μm are needed to achieve 10 GBit/in^2. Since it is desired to keep the tracking error below an eighth of the track width, the magnetic hard disk drive servo must maintain the tracking error below 0.12 μm at the above track width. In a low disturbance environment, some hard disk drive manufactures believe that they can achieve this tracking error accuracy without the addition of new sensors and/or actuators. However, conventional hard disk drives are used in a wide variety of environments which subject them to a significant amount of shock and vibrations. External disturbances excite lightly damped internal resonances in the hard disk drive which can cause the tracking error to easily exceed acceptable levels. Hence, a new direct adaptive servo scheme is presented which utilizes a micromachined accelerometer to improve the external disturbance rejection capability of the track following servo in hard disk drives. The objective of the control scheme is to minimize the variance of the position error signal in the presence of external disturbances. The adaptive controller acts as an add-on compensator to an existing fixed compensator. The micromachined accelerometer is mounted on the base casting of the hard disk drive in order to obtain a measure of the external disturbance.

A magnetic hard disk drive was subjected to a number of different external vibrations tests: rotational about the center of the actuator pivot and translational in the x, y, and z

directions. For a 10 tap adaptive FIR controller, experimental results display 15 dB attenuation and 89% reduction in the variance of the position error signal for the random external rotational disturbance. Similar performances were obtained in the x and y directions; while in the z direction, 15 dB attenuation and 53% reduction in the variance of the position error signal were experimentally verify for a random external disturbance. The rates of convergence of the FIR filter parameters averaged approximately 50 msec.

The hard disk drive was also subjected to external shocks about the center of rotation of the actuator bearing. Half sine waves of 3 rad/sec^2 in magnitude and 2.7 msec in duration were used as the external shocks. The maximum magnitude of the position error signal as a result of the shock was reduced by 68% using the adaptive accelerometer servo. The duration of the effect of the shock was also decreased by 10 msec.

Overall, the adaptive accelerometer control scheme successfully reduced the effects of external vibrations and shocks on the hard disk drive. Under these external disturbances, the hard disk drive was not able to read nor write without the utilization of the micromachined accelerometer based adaptive control scheme.

_____

Professor Roberto Horowitz, Chair Date

I dedicate this dissertation to my loving family.

LIST OF FIGURES

LIST OF TABLES

LIST OF SYMBOLS

$a(k)$	Discrete time accelerometer signal sampled at T.
a_i	ith coefficient of $A(q^{-1})$.
$\bar{a}_i$	ith coefficient of $A(q^{-1})$.
$\hat{a}_i(k)$	ith estimated coefficient of $\hat{A}(q^{-1})$ at sample k.
a_{di}	ith coefficient of $A_d(q^{-1})$.
a_{vi}	ith coefficient of $A_v(q^{-1})$.
$ac(k)$	Auto-correlation of kth value.
acc_i	ith coefficient of $A_{acc}(q^{-1})$.
$A(q^{-1})$	Denominator polynomial which is the convolution of $A_d(q^{-1})$ and $A_v(q^{-1})$.
$\bar{A}(q^{-1})$	Converged denominator polynomial of the nominal plant dynamics.
$\hat{A}(k, q^{-1})$	Estimate of denominator polynomial of the nominal plant dynamics.
$A^*(q)$	Non causal denominator polynomial of the nominal plant dynamics.
$A_{acc}(q^{-1})$	Denominator polynomial of the nominal accelerometer dynamics.
$A_d(q^{-1})$	Denominator polynomial of the nominal hard disk drive dynamics.
$A_v(q^{-1})$	Denominator polynomial of the nominal noise dynamics.
b_i	ith coefficient of $B(q^{-1})$.
$\bar{b}_i$	ith coefficient of $B(q^{-1})$.
$\hat{b}(k)$	Plant regressor vector multiplied by the plant parameter error.
$\hat{b}_i(k)$	ith estimated coefficient of $\hat{B}(q^{-1})$ at sample k.
b_{di}	ith coefficient of $B_d(q^{-1})$.
bcc_i	ith coefficient of $B_{acc}(q^{-1})$.
$B(q^{-1})$	Numerator polynomial which is the convolution of $B_d(q^{-1})$ and $A_v(q^{-1})$.
$B_d(q^{-1})$	Numerator polynomial of the nominal controller dynamics.
$B'(q^{-1})$	Non-delayed version of $B(q^{-1})$.
$B^-(q^{-1})$	Roots of $B'(q^{-1})$ outside the unit circle.
$B^{-*}(q^{-1})$	Roots of $B^-(q^{-1})$ reflected about the unit circle.
$B^+(q^{-1})$	Roots of $B'(q^{-1})$ inside the unit circle.
$\bar{B}(q^{-1})$	Converged numerator polynomial of the nominal plant dynamics.
$\bar{B}'(q^{-1})$	Non-delayed version of $\bar{B}(q^{-1})$.
$\bar{B}^-(q^{-1})$	Roots of $\bar{B}'(q^{-1})$ outside the unit circle.

ACRONYMS

ADC	Analog to Digital Converter
ARX	AutoRegressive eXogenous
ARMAX	AutoRegressive Moving Average eXogenous
ATA	AT-Attachment
BIOS	Basic Input Output System
bpi	Bits per Inch
BSAC	Berkeley Sensor and Actuator Center
CML	Computer Mechanics Laboratory
DAC	Digital to Analog Converter
DIP	Dual Inline Package
DOS	Disk Operating System
DSP	Digital Signal Processor
FIR	Finite Impulse Response
HDD	Hard Disk Drive
IACK	Interrupt ACKnowledge
IIR	Infinite Impulse Response
ISR	Interrupt Service Routine
LMS	Least Mean Squares
MFLOPS	Millions of FLoating point Operations Per Second
MIMO	Multiple Input Multiple Output
MISO	Multiple Input Single Output
MIPS	Million Instructions Per Second
NRRO	Non-Repetitive RunOut
PAA	Parameter Adaptation Algorithm
PC	Personal Computer
PCB	Printed Circuit Board
PES	Position Error Signal
RAID	Redundant Array of Independent disk Drives
ROM	Read Only Memory
RPM	Revolutions Per Minute
RRO	Repetitive RunOut
R/W	Read and Write
SAM	Servo Address Mark
SGA	Stochastic Gradient Algorithm
SISO	Single Input Single Output
SNR	Signal to Noise Ratio
SPR	Strictly Positive Real
TMR	Track MisRegistration
tpi	Tracks per Inch
TRK	Tracks
TTL	Transistor Transistor Logic
VCM	Voice Coil Motor

ACKNOWLEDGMENTS

I thank Professor Roberto Horowitz, Professor Albert P. Pisano, and Professor Roger T. Howe for their input and help in construction of this dissertation. I would especially like to thank Professor Roberto Horowitz for his support and guidance throughout the latter part of my graduate career. I would also like to express my gratitude to Professor Andrew Packard who was always available to help me. I also thank Patricia Giddings who put up with my endless chatter about football and question about why I did not get paid.

I express my sincerest gratitude to fellow labmates. Through the course of my graduate career, I have had the privilege to cross paths with many. I especially like to thank the following people for making my time away from research rewarding: Madhu Babu, Tsunglin Chen, Carlo Cloet, Steve Gaudio, Daniel Hernandez, Scott Keane, Martin Krucinski, and Lawrence Lee. I also thank Ahrie Moon who had to put up with my endless hours of complaints.

Of course, I cannot forget my labmate, roommate, and friend David Horsley who always had to listen to me say, “Hey, Dave. Can you look at this for a sec?” He not only helped me get through my research, but he also helped me waste countless hours in the gym.

Special thanks to John Ridgely and Pam Sirivedhin. Our movie nights not only got me out of lab, but they provided me with some delicious food. I also thank John for the countless hours he spent helping me out with everything under the sun. Jason Jones and Beth Ko also deserve special thanks. They made me feel like family by giving me a place to escape the madness of graduate school, not to mention a home cooked meal during Monday Football. Of course, I thank Henry and Angela Hong. They are the very definition of the Thousandth man and put up with my pains and complaints about life in general. I also thank Samuel Ho who has had to put up with me from the beginning of my stay at Berkeley, Daniel Magana who has been there since the beginning of time, and Tamra Dodson who has been my dearest friend throughout my college years.

1. INTRODUCTION

1.1 PROBLEM DESCRIPTION

The areal density of magnetic hard disk drives is increasing at an annual rate of 60% and is expected to reach 10 GBit/in^2 by the turn of the century[28]. The areal density is the product of the radial density (number of tracks per inch on the disk surface) and the linear density (number of bits per inch in each track). The radial density is directly related to the tracking accuracy of the servo of the HDD, while the linear density is directly related to the flying height of the read/write head. Current areal densities are at 1.6 GBit/in^2, with a radial density of 11,000 tpi (2.54 μm per track) and a linear density of 150,000 bpi. Track densities of 25,000 tpi (1 μm per track) are needed to achieve 10 GBit/in^2[39], assuming an appropriate increase in linear density. Since it is desired to keep the tracking error below an eighth of the track width[23], the servo of the HDD must maintain the tracking error below 0.12 μm at these track widths. In a relatively disturbance free environment, current hard disk drive manufactures believe that this level of tracking accuracy can be achieved at 25,000 tpi without the addition of new sensors nor actuators. In the presence of external shock and vibrations however, a new servo architecture may be needed[19]. External disturbances excite lightly damped internal resonances in the HDD which can cause the tracking error to exceed acceptable levels. As the track density increases, the effects of external shock and vibrations consume more of the allowable tracking error budget since the allowable tracking error decreases. Conventional HDD's are being used in a wide variety of environments which subject them to a significant amount of shock and vibrations. For example, computers are being used on factory floors, and portable computers and personal data assistants are becoming increasingly popular. Moreover, the video camcorder and mobile communication industries may also soon be utilizing hard disk drives in their hand-held products.

Throughout the history of magnetic storage, two different technologies have been leap- frogging each other to advance areal density: servo mechanics and head-media. In the beginning, servo mechanics exceeded head-media technology. However, it was not

long before head-media technology surpassed the positioning technology, and it fell upon the servo engineers to improve tracking accuracy. This back and forth nature has continued to this day. Currently, it is the servo mechanics that is the governing parameter in determining maximum areal density[30].

Two major functions are provided by the servos: track seeking and track following. The track seeking servo moves the read/write head from one track to another in minimal time. The track following servo maintains the R/W head position over the center of a selected track. The measured deviation of the R/W head from the center of the track is called the position error signal. It is the performance of the track following servo which limits the achievable radial density. Typical tracking accuracies of 12% of the track width are required from the track following servos. The tracking accuracy of HDD's is often listed as a 3σ number, assuming a Gaussian distribution. This performance measure is called the track misregistration. With the narrow track widths in today's HDDs, the effect of shocks and external vibrations can easily cause the TMR to exceed 12%.

Many technologies are being explored to improve tracking performance in HDDs. One feasible option is integrating a micropositioner between the R/W head and the suspension[18,19,39]. The micropositioner will allow for the collocated control of the R/W head. Another option is to add piezoelectric elements to the suspension[41] in order to actuate the head. A third option is to mount transducers on the HDD to obtain a measure of the disturbance and to feedforward this signal through some control scheme. The third approach is examined here. The purpose of this dissertation is to develop and evaluate a new direct adaptive servo scheme which utilizes a micromachined accelerometer to improve the external disturbance rejection capability of the track following servo in hard disk drives. The objective of the control scheme is to minimize the variance of the position error signal in the presence of external disturbances.

A micromachined accelerometer is placed on the base casting of the HDD to measure external disturbances. This acceleration signal is fed through an adaptive feedforward compensator which minimizes the variance of the tracking error produced by the disturbance. The micromachined accelerometer is placed on the base casting to allow for

ease of integration and use of low cost accelerometers. At present, placement of accelerometers on other parts of HDD, such as the suspension, is not feasible because of added complexity and cost involved in such accelerometers, though this option may become viable in the near future. Current HDDs are being manufactured with accelerometers which are used to prevent reading or writing after a shock has been detected. These accelerometers, however, are not used in a control loop to attenuate the effect of the disturbances.

1.2 PREVIOUS RESEARCH

A number of researchers have investigated the feasibility of using accelerometers to improve the rejection of disturbances. Listed below is a brief, partial history of the use of accelerometers in HDD's.

R. White[90] proposed an accelerometer based scheme to compensate for disturbances parallel to the spindle axis. The accelerometer was mounted on the base casting of the HDD. Even in 1977, White realized that disturbances which cause the head to come in contact with the disk were potentially the most damaging types of disturbances. Head crashes can easily destroy the disk media, or worse, tear the R/W head off the suspension. He developed two methods to actuate the flying height of the slider. First he considered using a pneumatic valve to change the air pressure inside the chassis of the HDD, but he realized that pneumatic actuation could not provide the necessary bandwidth. Hence he proposed using a DC motor to actuate the slider to obtain the desired bandwidth. The accelerometer compensator was not adaptive, but determined off-line.

In 1986, D. Hanks[31] proposed mounting accelerometers to the head disk assembly to attenuate both external rotary disturbances and internally generated rotary disturbances caused by the spindle motor or rotary actuator. These disturbances were assumed to be in the plane of the disk platters. A single constant gain was used to feed the accelerometer signal to the voice coil motor. The value of the gain was determined off-line.

In 1991, D. Davies and M. Sidman[81,82,83] also proposed using an accelerometer based scheme to compensate for angular acceleration in the plane of the hard disk drives's

actuator during both track seeking and following in 1991. They assumed a balanced rotary actuator assembly. A single constant gain was used to feed the acceleration signal forward to the VCM. As in the previous schemes, the gain was determined off-line. Experimental results were obtained for both seeking and track following modes of a 5.25" HDD. Seek times were reduced by 10 ms and external disturbances were attenuated by 12 dB.

C. Lee *et al.*[52] used piezoelectric accelerometers mounted on the base casting to reject external disturbances. Both rotary and linear disturbances were attenuated since an unbalanced rotary actuator model was used to determine off-line the value of the single constant gain.

D. Abramovitch[1,2] used an adaptive scheme to estimate the value of a single feedforward parameter. A least mean squares algorithm[93] was used for the adaptation algorithm. A multirate scheme was utilized to sample the accelerometer signal at a faster rate to improve performance of the feedforward scheme. Experimental results for rotary disturbances were obtained for the track following servo of a 1.3" HP Kitty Hawk HDD. A 10 dB attenuation was demonstrated over a frequency range of 0 to 600 Hz; however, no stability or convergence proofs were presented.

M. White and M. Tomizuka[88,89] used a multiple tap adaptive FIR filter to reduce the effect of rotary external disturbances. A constant gain, filtered-x LMS algorithm[93] was used. Stability and convergence analysis were presented. Experiments were conducted on a 5.25" HDD in track following mode. Approximately 30 dB of attenuation were obtained from 40 to 100 Hz for a 40 tap FIR filter. The estimate of the plant of the HDD which was needed for the filtered-x LMS algorithm was determined off-line.

The contribution presented in this dissertation is the formulation and convergence analysis of a new direct adaptive control scheme which uses an accelerometer signal to attenuate the effect of external disturbances on magnetic HDD's. The scheme consists of two Parameter Adaptation Algorithms which are run simultaneously to estimate both the plant dynamics of the HDD and the optimal FIR filter to minimize the variance of the position error signal caused by the external disturbance. Instead of using a LMS algorithm

as previous researchers have done, the stochastic gradient approximation algorithm is used. Further, a complete convergence analysis of the adaptive control scheme was performed using the ODE approach. Furthermore, experimental validation was conducted about three translational and one rotational axes of the HDD instead of just a rotational axis. Additionally, attenuation of the disturbance due to external shocks was also demonstrated.

1.3 OUTLINE OF CHAPTERS

This dissertation is organized as follows. In Chapter 2, a description of the components used in current HDD's is described. It details the possible sources of error in the position error signal during nominal operation and when the HDD is subjected to external shock and vibrations. The nominal servo loop for HDDs along with the detection scheme used to generate the position error signal is explained. Finally, experimental models describing the nominal plant and controller dynamics for a commercially available HDD are identified.

In Chapter 3, the description of the experimental setup used for testing of the adaptive accelerometer algorithm on a commercially available HDD is explained. It gives an overview of the devices involved and their electrical/mechanical properties. The issues involved with interfacing with the HDD and the digital signal processor, as well as the design of the interface board, are discussed. Sample C code which was used to send HDD commands over the ATA interface is given along with the C code of the interrupt service routine on the DSP.

In Chapter 4, the formulation of the adaptive feedforward algorithm using accelerometers is presented. It describes the relationship between the adaptive scheme and Wiener filtering. It then goes on to discuss the two parameter adaptation algorithms used within the adaptive feedforward algorithm. The theoretical work justifying the algorithm is also presented with the theoretical validation given in Appendix A. Simulation results using experimental models of the HDD from Chapter 2 are also presented.

In Chapter 5, the testing methods and the experimental results of the adaptive feedforward algorithm are presented. The HDD is tested with both single and random frequency external vibrations about four different axes. The performance is compared with two previous disturbance rejection schemes. Lastly, the performance of the algorithm with respect to external shocks is also investigated.

In the final chapter, Chapter 6, the major results and achievements of this research are summarized. Further, a recommendation for future work is also outlined.

.

2. BASIC HARD DISK DRIVE MECHANICS

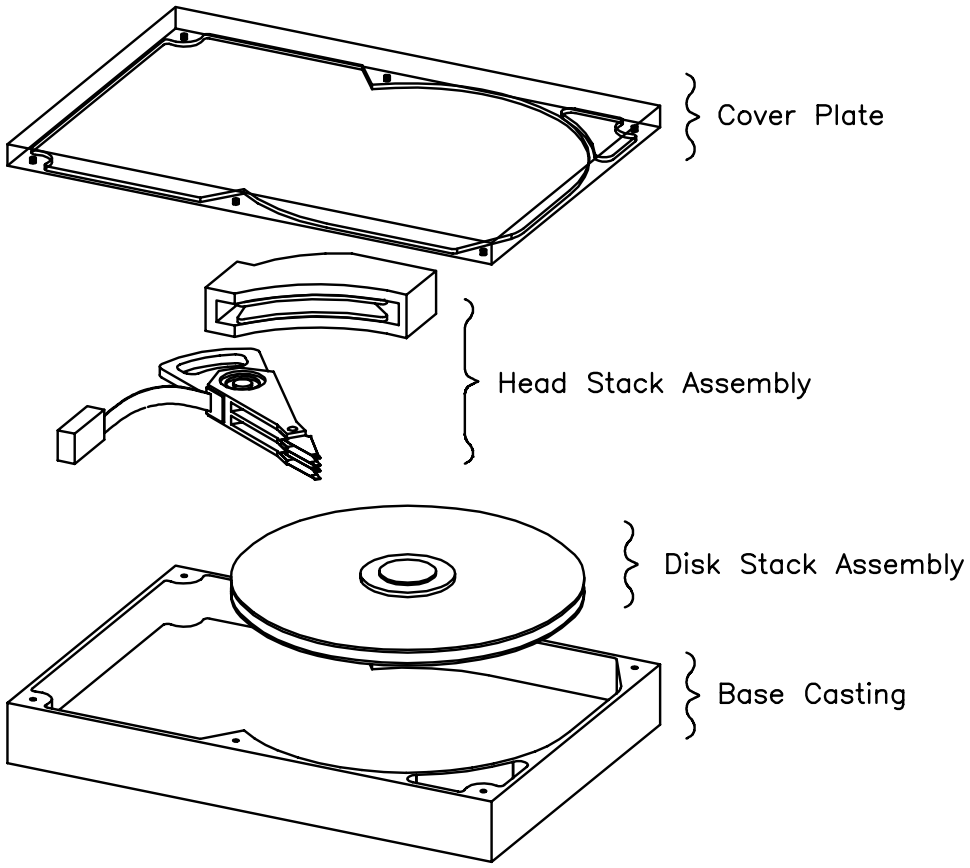

Figure 2-1. *Overview of conventional rotary HDD. It consists of the head stack assembly, disk stack assembly, and the housing (base casting and cover plate).*

Most HDD's use a rotary actuator to position the R/W head over a specific track. The configuration of a conventional rotary HDD is displayed in Fig. 2-1. The HDD consists of three major parts: the head stack assembly, the disk stack assembly, and the housing (base casting and cover plate).

The head stack assembly, shown in Fig. 2-2, contains the rotary actuator as well as the magnetic heads used to read or write data from the disks. The rotary actuator is driven by a VCM. The VCM is composed of a coil of wire attached to the rear of the actuator. This coil is placed in a magnetic field generated by a pair of rare earth permanent magnets. A torque on the actuator is generated when a current is passed through the coil. The actuator

.

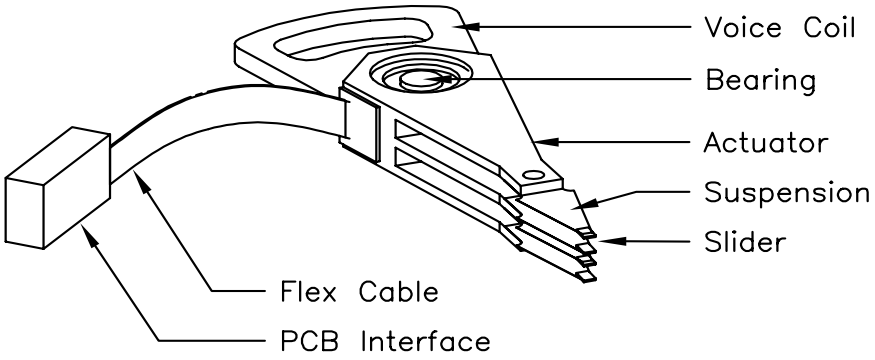

Figure 2-2. *Head stack assembly containing the voice coil, actuator, actuator bearing, suspension, slider, and the flex cable.*

is free to rotate about a bearing which is attached to the base casting. The actuator is balanced such that the center of mass is positioned at the center of rotation of the bearing. The flex circuit which contains the power leads for the VCM as well as the signal wires for each head is attached to the actuator near the bearing. Each slider is mounted to the actuator by a suspension. The purpose of the suspension is to allow the slider to follow the vertical runout of the disk in order to maintain the required submicron flying height. The slider is attached by a gimbal to the end of the suspension. It allows for the formation of an air bearing between the slider and disk surface. The R/W head is attached at the trailing edge of the slider.

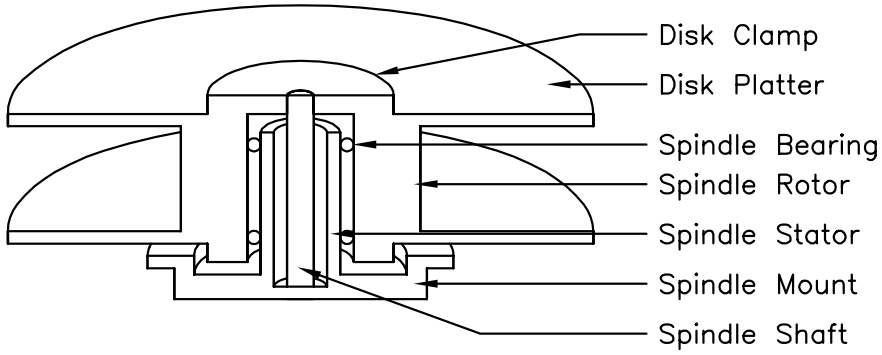

Figure 2-3. *Disk stack assembly containing the disk platters, spindle assembly, and spindle shaft.*

The disk stack assembly contains the disk platters and the spindle motor as shown in Fig. 2-3. The spindle motor rotates the disk platters within 0.25% of the specified rotational velocity. The disk platters are made out of aluminum disks which are 95 mm in diameter and 0.8 mm thick. They are mounted to the rotational hub of the spindle motor.

The spindle motor assembly is mounted at the bottom of the base casting and at the top by the cover plate.

The base casting and cover plate are designed such that the spindle shaft is rigidly supported at both ends. As will be discussed in Section 2.2.2.3, a rigid spindle shaft will reduce PES due to spindle vibration modes.

2.1 POSITION ERROR SIGNAL

2.1.1 POSITION SENSING SCHEMES

In order to perform closed-loop control of the actuator, a method to determine the position of the R/W head relative to the center of the data track must be developed. This measurement is commonly referred to as the position error signal in the industry. In early HDD's, the position of the R/W head was determined by an angular or linear encoder attached to the actuator. However, this method did not provide a direct measurement. Mechanical resonances, temperature variations, and encoder resolution limited the track density[44]. Since the actual position of the R/W head relative to the track was desired, HDD manufacturers quickly moved to incorporating the PES information onto the magnetic disks. This change allowed the R/W head to read the position directly, ensuring more exact knowledge of the R/W head position. There are three methods currently being used in HDD's to measure PES: dedicated, embedded, and hybrid.

Dedicated servo technology used one whole surface of a disk to record position information in reference tracks. One R/W head was *dedicated* to reading the reference tracks. The position of the other R/W heads were assumed to be equal to the reference R/W head since all the R/W heads are vertically stacked above each other. In the late 1960s, dedicated servo technology began to replace encoder mechanical positioning technology[21]. A major drawback of the dedicated servo was that mechanical resonances and thermal effects caused variations in the positions of the other R/W heads in the stack assembly with respect to the reference R/W head. Again, track densities were limited by the position sensing technology.

In the late 1970's, HDD manufacturers began using embedded servo technology[21]. Position information was recorded on each disk, allowing the active R/W head to sense its position relative to the track. A common arrangement of embedded servo sectors is displayed in Fig. 2-4. The concentric data tracks are divided into pie shaped regions. The servo sectors are placed as radial spokes on each disk platter. Because position information is only available in these servo sectors, the servo system is a sampled data system. Hence, all the challenges associated with sampling, i.e. aliasing, Nyquist frequency, and phase delay must be considered in the servo design. Most commercially available HDD's use embedded servo sectors to generate the position error signal.

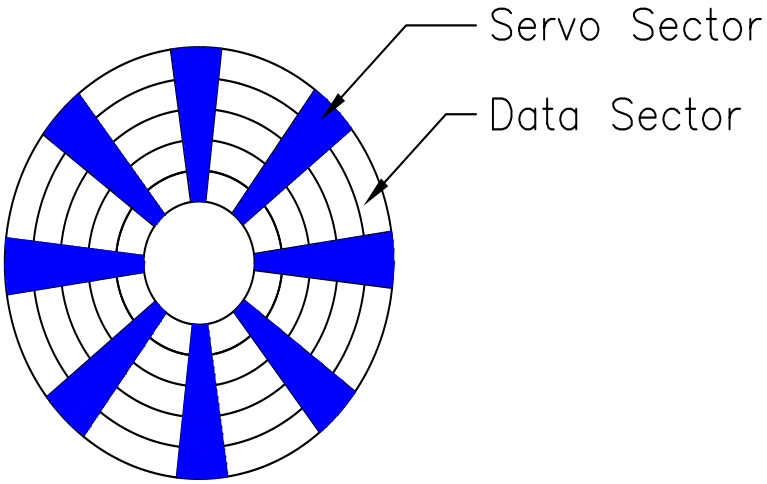

Figure 2-4. *Embedded Servo Sectors. The shaded pie shaped regions are the servo sectors. Note that the servo sector to data sector aspect ratio is not drawn to scale.*

Hybrid servo technology combined both the dedicated and embedded servo technology. The embedded servo sectors were recorded at a much lower density than in the embedded servo alone. The dedicated surface was used as the primary servo with sparse embedded sectors to compensate for the thermal and mechanical effects. The hybrid system minimized the disadvantages of both the dedicated and embedded technologies, but it required more storage space. Hence, it was not very common in production HDD's.

2.1.2 DECODING OF POSITION ERROR SIGNAL

Since embedded servo technology is the most common PES measuring method, and it

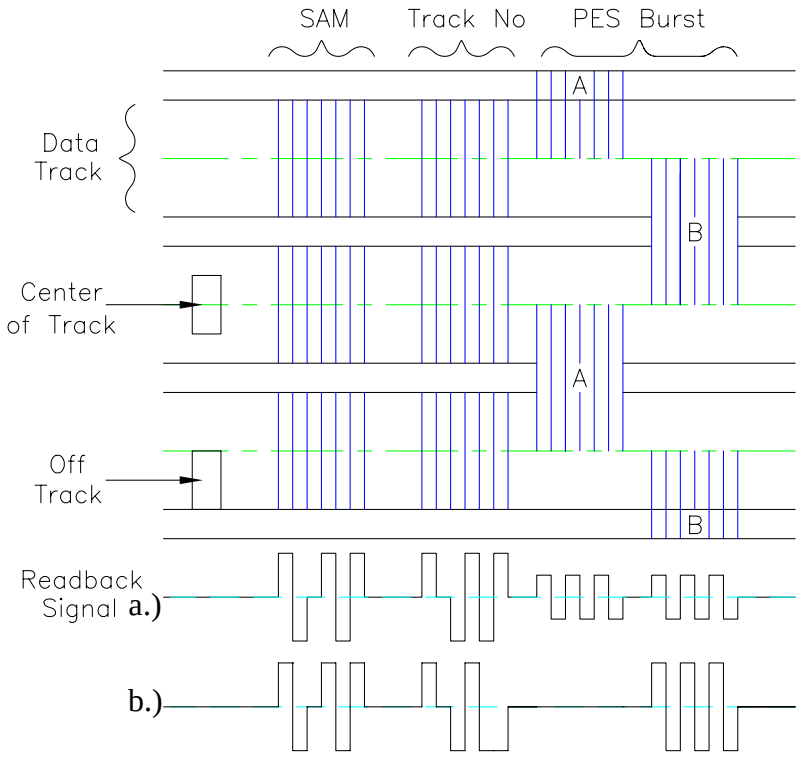

Figure 2-5. *Schematic of a servo sector. The readback signal is shown for various head positions.*

was used in the HDD's used in the experimental testbed for this dissertation, it will be the only method described in detail. A simplified schematic of a servo sector is shown in Fig. 2-5. As the R/W head flies over the servo sector, it first reaches the servo address mark. The SAM identifies the beginning of the servo sector and signals the processor of the HDD to begin the servo algorithm. No data or any other information stored on the magnetic disk is allowed to have the magnetic signature of the SAM. Next the R/W head reads a grey coded number which represents the track number. At the end of the servo sector, a series of patterns called bursts are written. Each burst is the width of a track and is written between the center of the current track and the centers of adjacent tracks.

By subtracting the difference in the amplitude of the A and B burst, the position of the R/W head can be determined. Assuming the width of the read head is half of a track width, then equal amounts of burst A and B correspond to the R/W head being at the center of the track. The readback signal for the above case is displayed in Fig. 2-5a. If the position of the R/W head is 25% of a track width toward the outer diameter, then no

amount of burst A and a maximum amount of burst B will be read. The readback signal for this case is shown in Fig. 2-5b. The relationship between burst amplitude and R/W head position is given by Eq. (2-1)

$$\Delta x = W_r \frac{v_a - v_b}{2v_m}, \tag{2-1}$$

where W_r is the width of the read head, v_a amplitude of the A burst, v_b is the amplitude of the B burst, and v_m is the maximum amplitude for the bursts[47]. Notice that with the two-burst pattern, the maximum detectable excursion is 25% of a track width. To eliminate this problem, two or more bursts are added to increase the dynamic range of the PES.

2.2 SOURCES OF TRACK RUNOUT

Track runout in HDD's is decomposed into two categories: repetitive and nonrepetitive. Runout that is the same for every revolution of the disk is called repetitive runout. Hence the identical magnitude of runout is obtained at each servo sector of a track. For example, if the runout was 0.1% of a track at servo sector 10 during the n^{th} revolution of the disk, then it will be 0.1% again at servo sector 10 during the $(n+1)^{th}$ revolution. Since RRO is synchronized with the frequency of rotation of the disk, it will only appear at the spindle rotation frequency and its harmonics. Any other type of runout is nonrepetitive runout. It has many periodic components as well, but the magnitude of the runout is not identical for each revolution of the disk.

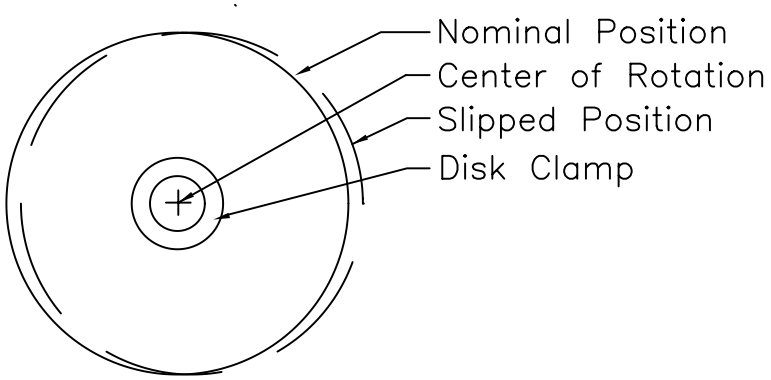

Figure 2-6. *Translation of disk platter is the major cause of repetitive runout.*

2.2.1 REPETITIVE RUNOUT

Disk slip is one of the biggest contributors to track runout and is the main cause of RRO. It refers to the physical translation of a disk in the disk stack assembly. The effect of disk slip is that the disk platter and the axis of rotation of the spindle motor are no longer concentric. Radial eccentricity resulting from disk slip is depicted in Fig. 2-6. It can occur when the drive undergoes an external shock or when there is a mismatch between the thermal expansion coefficients of the disk platters and the spindle hub. The radial eccentricity will cause the runout to occur on every revolution.

Another source of RRO occurs during servo-writing. Servo-writing is the process of writing the data and servo sectors onto the magnetic disks. Any tracking errors during servo-writing are permanently written onto each track and become RRO during the normal operation of the HDD. Other sources of RRO arise from imperfections in the spindle bearings and magnetic imbalance in the spindle motor.

2.2.2 NON REPETITIVE RUNOUT

There are many sources of NRRO. A HDD has a plethora of mechanical structures that can vibrate and introduce tracking errors. A few of the major causes will be summarized below.

2.2.2.1 SUSPENSION RESONANCES

In general, the suspension is designed to be very soft in the vertical direction and as stiff as possible in all other directions. The suspension resonance modes which contribute to TMR budget also limit the bandwidth of the controller. The current HDD positioning system is non-collocated which means that the control actuation and sensing are physically separated. The control actuation occurs at the VCM and the position sensing occurs at the R/W head. The suspension and the actuator separate these two elements, and hence the mechanical resonance modes in between them have a tremendous effect on the closed-loop bandwidth. Further, since multiple low frequency resonances modes exist, extending the bandwidth of the controller of the HDD is difficult.

Two typical suspension modes are shown in Fig. 2-7. The resonant frequencies of the

first bending and first torsional modes for a typical suspension are 220 Hz and 2700 Hz respectively[24]. Since the 1st bending mode is an out-of-plane and as long as the suspension is balanced, it does not have much effect on the PES. However, the 1st torsional mode has a significant effect on the PES.

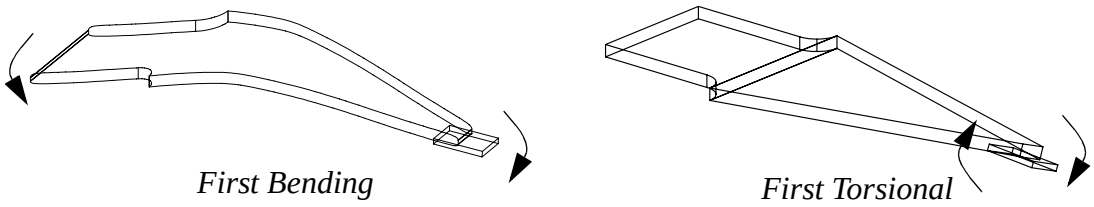

Figure 2-7. *First two suspension modes of which the first torsional has a significant effect on the position error signal.*

2.2.2.2 DISK PLATTER RESONANCES

The disk platters are 95 x 0.8 mm aluminum disks. These platters have mechanical resonance modes which contribute to PES. The resonance modes are excited by the turbulent air flow over the disk surfaces [13,73]. With no external vibration, disk flutter can contribute up to 0.16 μm to the PES[61]. Hence at 6,000 tpi up to 37% of the allowable TMR is consumed. Since all disk drives currently use these platters, the contribution of disk flutter to PES will increase as tpi increases.

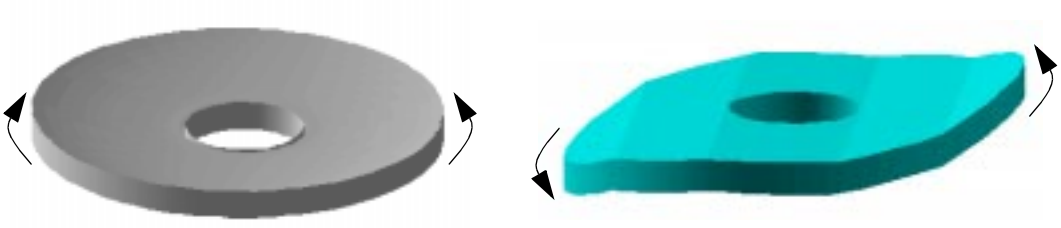

Figure 2-8. *Disk platter modes. a.) Mode (0,0) where all portions of disk move in phase. b.) Mode(0,1) where portions of disk move out of phase about a diametrical lines.*

Many vibration modes exist for a stationary annular platter with its inner diameter clamped. The modes are denoted as (m, n) where m denotes the number of nodal circles and n denotes the number of nodal diameters in the mode[14]. Nodal circles are concentric circles on the platter where there is no displacement. Nodal diameters are diametrical lines where there is also no displacement. The frequencies of these modes are

denoted as ω_{mn}. The first two modes of the disk platter are displayed in Fig. 2-8. Mode $(0, 0)$ is the "bowl" shaped mode and is depicted in Fig. 2-8a. The deflection of all concentric circles are in phase. Fig. 2-8b depicts mode (0,1). It is the first mode with a nodal diameter. Half of the platter deflects upward while the other half deflects downward. Other low frequency vibration modes of interest are the (0,2) and (0,3) modes. The natural frequencies of these modes are listed in Table 2-1[61].

Mode	Frequency
(0,0)	608 Hz
(0,1)	616 Hz
(0,2)	729 Hz
(0,3)	1168 Hz

Table 2-1: Natural frequencies of selected disk platter modes.

As the disk platters are rotated to the operating frequency, the stationary modes increase in frequency because of the apparent increase in stiffness of the platter due to the centrifugal acceleration. For example, the natural frequency of mode (0,0) rises to 638 Hz due to this effect[61]. Further, the stationary modes also bifurcate into forward and backward traveling waves whose natural frequencies are given by

$$\omega_{mn}^{f} = \omega_{mn} + n\Omega \tag{2-2}$$

$$\omega_{mn}^{b} = \omega_{mn} - n\Omega \tag{2-3}$$

where ω_{mn}^{f} is the frequency of the forward mode, ω_{mn}^{b} is the frequency of the backward mode, ω_{mn} is the frequency of the stationary mode after the increase in stiffness, and Ω is the frequency of rotation of the spindle[14]. For example, if the spindle frequency was 75 Hz, mode (0,1) splits into two modes with natural frequencies of 574 Hz and 724 Hz. However, mode (0,0) does not bifurcate since it has no nodal diameters. A waterfall plot of the vibration modes of a disk platter as the frequency of rotation of the disk is varied is shown in Fig. 2-9. (A waterfall plot displays the power spectral density of axial motion of the disk platters as the spindle frequency is varied.) The natural frequency of the stationary mode (0,0) is approximately 625 Hz regardless of the spindle frequency, while

the natural frequencies of the bifurcated modes of (0,1) vary as the spindle frequency varies. At a spindle frequency of 150 Hz, the forward and backward modes are 300 Hz apart from each other.

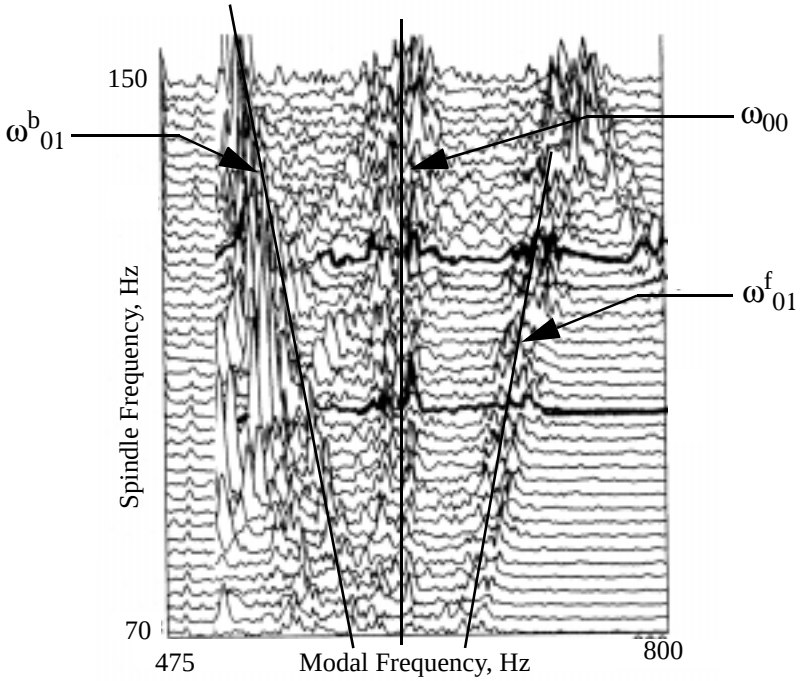

Figure 2-9. *Waterfall plot of disk platter resonances versus spindle motor rpm.*

2.2.2.3 SPINDLE RESONANCES

The spindle motor and its assembly also affect the tracking error in magnetic HDD's. The spindle vibration modes can be induced by unbalanced magnetic forces in the motor, defects in the bearing, or external vibrations. NRRO is very sensitive to the spindle frequency since bearing defects can excite spindle vibration modes. The cross-section of a typical ball bearing spindle assembly is displayed in Fig. 2-10.

G. Frees explored the effect of spindle dynamics on PES[23], and he conducted his experimental tests on a 3.5" HDD with ball bearings. The first two rigid-body modes of the ball bearing spindle are shown in Fig. 2-10. The measured frequencies of the pitch and radial modes are 318 Hz and 841 Hz respectively. The pitch mode also exhibits the bifurcation of its mode as the disk stack is spun up to speed[23]. For the particular HDD tested, Frees showed that the total contribution of these modes can cause up to 0.405 μm

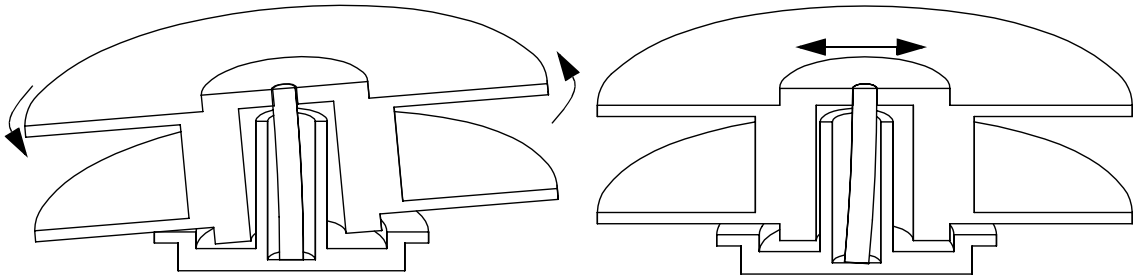

Figure 2-10. *First two modes for ball bearing spindle.*

of TMR. Although their contribution in current HDD's is much lower, spindle resonance modes still contribute to a significant fraction of TMR.

With increasing spindle frequencies, the magnitude of NRRO generally increases since bearing imperfections excite the mechanical resonances of the spindle assembly. Therefore, bearing defects have limited the spindle frequency. Typical HDD spin at approximately 7,200 rpm with just one production drive spinning at 12,000 rpm.

A number of steps have been taken to minimize the spindle resonances effect. Until recently, many HDD's have contained disk stack assemblies that were supported only at the bottom end of the shaft in the interest of cost. Harrison showed that a spindle shaft supported at both ends reduces both RRO and NRRO, and the presence of the upper support renders RRO and NRRO less dependent on spindle frequency[32].

Many companies are also investigating the use of hydrodynamic bearings instead of ball bearings. The hydrodynamic bearings use a liquid such as air or oil as the load bearing element. The major advantage of these bearings is the low NRRO even at high spindle frequencies. Swann demonstrated that air bearings can reduce NRRO by a factor of 20 dB[77]. Further, NRRO induced by a hydrodynamic bearing is also less dependent on spindle frequency[23] and a considerable amount of damping is introduced. Commercial HDD's which use hydrodynamic bearings are currently available.

2.2.2.4 EXTERNAL DISTURBANCES

External disturbances and shocks which excite any of the above resonance modes will cause an increase in TMR. Since bearing friction is rather small, disturbances in the plane

of the disk platters can also cause rigid-body rotation between the R/W head and the track. Disturbances which rotate the base of the HDD about the center of the actuator bearing are the most damaging[2]. Further, since the actuator arm can be unbalanced, i.e. the center of mass not coinciding with the center of the pivot bearing, HDD's can be sensitive to external disturbances. Under a 25 G shock lasting 2 msec, even eccentricities as small as 90 μm of the center of mass of the actuator from the center of rotation of the pivot can cause a TMR of 20% of a track width[69].

External disturbances and shocks parallel to the spindle axis can also cause an increase in TMR. Disk platter resonances as well as suspension resonances can be excited[30]. Even more potentially damaging are large shocks which cause the R/W head to overcome the preload and separate from the surface. The magnetic disk surface is then damaged as the slider strikes the surface. The slider can impact the surface of the disk platter multiple times per shock and cause pitting of the magnetic disk surface[5]. Shocks of short duration cause more damage than shocks of long duration[50] because of their higher frequency components.

2.2.2.5 Actuator Bearing Friction

There are many other sources which can cause tracking error. Friction in the actuator pivot bearing limits the tracking performance of the actuator. The friction in the actuator pivot consists of many components: Coulomb friction, viscous friction, stiction, and hysteresis[26]. Further, the bearings have a low frequency resonance at approximately 35 Hz which further causes an increase in TMR.

2.3 Servo Architecture

As stated above, there are two major functions provided by the nominal servo of a HDD: track seeking and track following. It is the performance of the track following servo which limits the achievable radial density. Improved performance of this servo, especially under external vibrations and shock, is the goal of this research. The objective of the track following servo is to minimize the variance of the PES. More precisely, the objective is to minimize the variance of the PES while a track is being written and

minimize the variance of the PES with respect to the written track while the track is being read. For example, suppose that the only component of the runout is RRO. Since the open-loop system has finite gain, there is some nominal RRO which remains after it is attenuated by the closed-loop sensitivity transfer function. This nominal RRO is written on each data track. Hence the data tracks are no longer concentric but have eccentricities due to RRO. An exaggerated data track caused by RRO is depicted in Fig. 2-11. Since RRO is repetitive and as long as the closed-loop performance is not changed, the R/W head will track the written data track. However, if the closed-loop properties are changed, the attenuation of RRO change. The R/W head no longer tracks the written track, but a new profile. Tracking the new profile introduces a repetitive error between the R/W head and the written track. Hence the properties of the closed-loop system must remain constant after the data is written. If NRRO is included in the runout, the above discussion

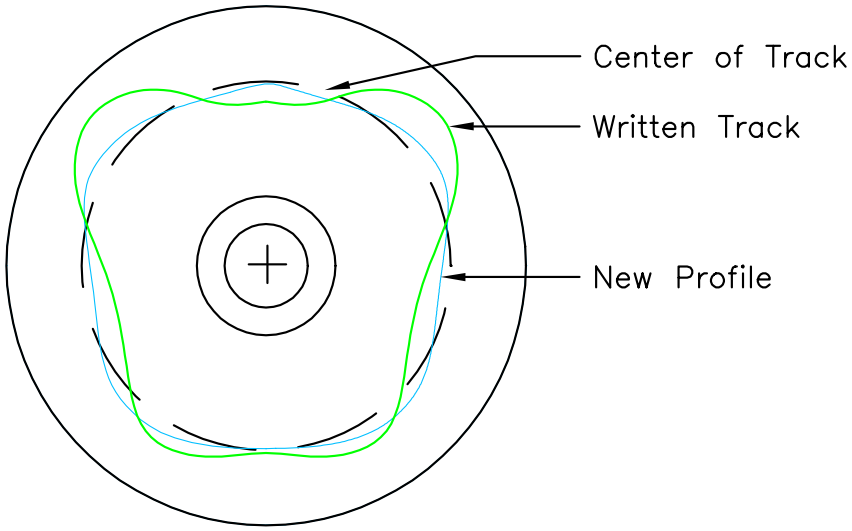

Figure 2-11. *Comparison of the track eccentricities caused by different attenuation of RRO.*

still holds. Once the data has been written onto a data track, the optimal tracking strategy is to track the mean of NRRO. Since the nominal controller has integral action, the mean of NRRO is generally zero. Hence for NRRO, the variance of the PES from the center of the track should be minimized.

Most commercially available HDD's today have DSP's which implement the nominal digital servo algorithm. The nominal block diagram[71] for a typical HDD control loop is

shown in Fig. 2-12. The electrical dynamics of the power amplifier which converts the control signal voltage to the appropriate voltage for the VCM is denoted by $G_{pa}(s)$. The dynamics of a notch filter are represented by $G_n(s)$. The notch filter prevents the control inputs from exciting the first suspension resonance mode[86]. A low pass filter which prevents the VCM from responding to high frequency noise is denoted by $G_{lp}(s)$. The dynamics of the VCM which converts the input voltage signal to the appropriate torque on the actuator are represented by $G_{vcm}(s)$. It is generally a constant over the frequency range of interest. A torque disturbance which effects the actuator is given by $\tau_c(t)$. The mechanical dynamics of the actuator and suspension which convert the VCM torque to R/W head position are represented by $G_{arm}(s)$. The R/W head position is added to the total runout, $r_c(t)$, to form the PES, $y_c(t)$.

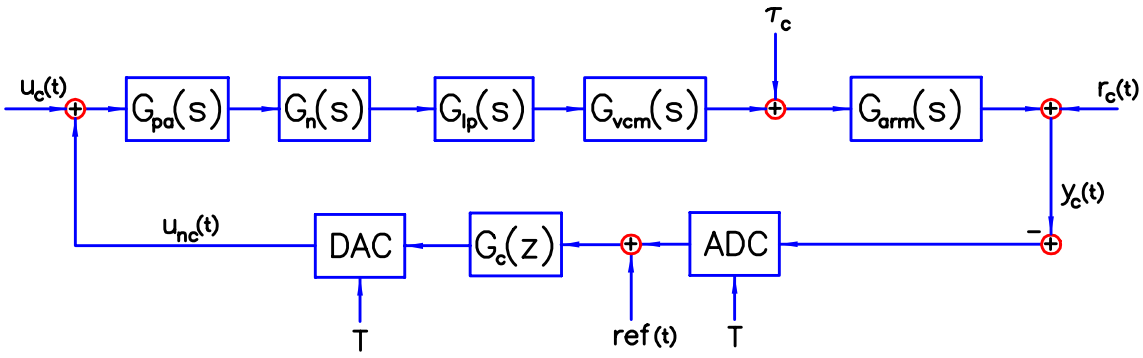

Figure 2-12. *Nominal block diagram for a HDD plant and controller.*

All the above signals and systems are represented in the continuous time domain. The Analog-to-Digital converter then samples $y_c(t)$ with a certain sampling period T, and the result is added to the reference position, $ref(t)$, which is nominally zero (center of track). The resultant signal is then sent to the digital controller, $G_c(z^{-1})$, to calculate the nominal control output. The nominal control output is then converted back to an analog signal by the Digital-to-Analog converter. The nominal control voltage, $u_{nc}(t)$, is then summed with the auxiliary control, $u_c(t)$, to produce the input voltage to the power amplifier.

The block diagram in Fig. 2-12 can be simplified to the block diagram in Fig. 2-13. The discrete time version of the series combination of the continuous time dynamics represented by $G_{pa}G_nG_{lp}G_{vcm}G_{arm}(s)$ is denoted by $P(q^{-1})$. The series combination of the gains represented by the ADC and the DAC and the discrete time controller

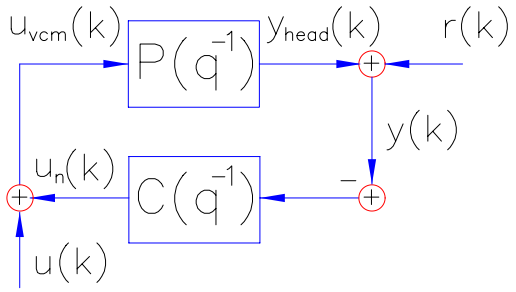

Figure 2-13. *Simplified discrete time block diagram of a HDD control loop.*

$G_c(z^{-1})$ is represented by $K(q^{-1})$. The reference signal was taken to be zero, $u(k)$ is the sampled auxiliary control input, $r(k)$ is the sampled runout signal which contains the combination of $r_c(t)$ and $G_{arm}\tau_c(t)$, and $y(k)$ is the sampled PES signal. This model is used to represent the HDD throughout the rest of this dissertation.

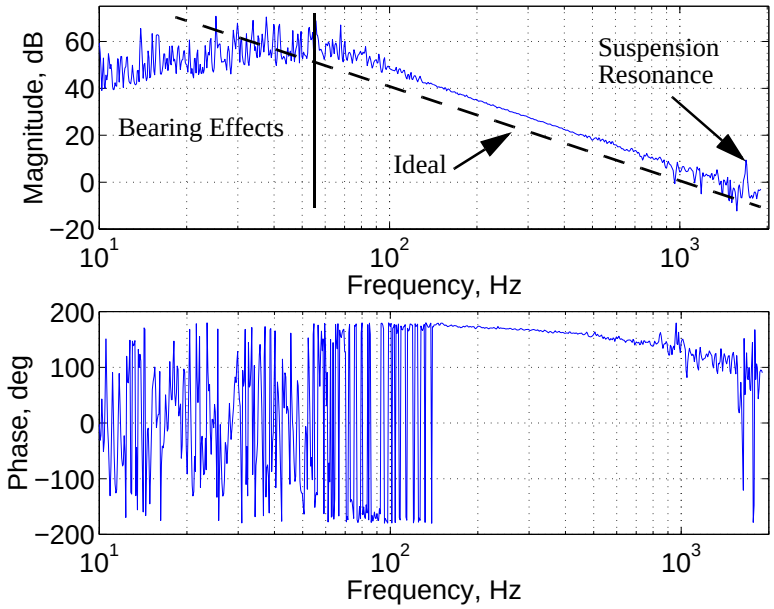

Figure 2-14. *Experimentally measured plant transfer function. Dashed line represents the ideal behavior of the plant of a HDD.*

The transfer function of $P(q^{-1})$ for a typical HDD is displayed in Fig. 2-14. Since the input to $P(q^{-1})$ is a torque and the output is position, the transfer function for $P(q^{-1})$ should be a double integrator if $P(q^{-1})$ was a pure inertia. The frequency response for a double integrator is shown as a dashed line in Fig. 2-14 below the measured response for clarity. However, as stated in Section 2.2.2.1 and Section 2.2.2.5, suspension resonances and bearing effects alter the transfer function. Between 60 Hz and 1 kHz, the plant

behaves as a double integrator with a gain and a one step delay due to the sampling of the PES. At 1.8 kHz, the first torsional mode of the suspension is visible even after the application of the notch filter.

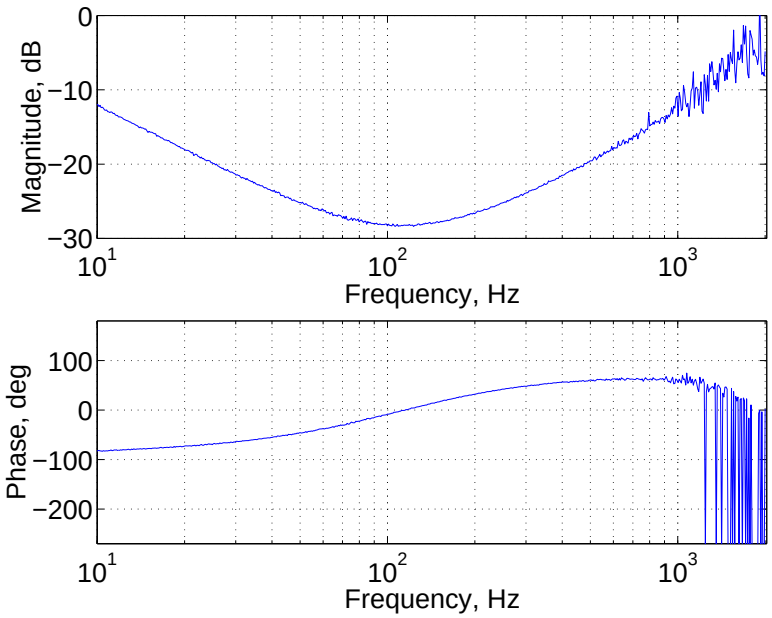

Figure 2-15. *Experimentally measured nominal controller transfer function.*

The transfer function of a typical HDD nominal controller, $K(q^{-1})$, is shown in Fig. 2-15. The compensator is simple in structure. At low frequencies integral action is included to reduce steady state error and reduce frictional effects. The integral action is followed by a lead-lag compensator to get the desired gain and phase margins.

The open-loop transfer function for the system described above is displayed in Fig. 2-16. The phase margin is 38^{o} at 383 Hz; and the gain margin is 5 dB at 1120 Hz. These transfer function measurements were taken from a HDD that has been in production for several years. Current HDD's have much higher phase and gain crossover points.

2.4 SYSTEM MODELING

This section describes the models which were used to generate simulation results. The models are based on experimental data obtained from a Seagate 2.5" HDD which was used to experimentally validate the adaptive algorithm. The Seagate HDD has a sampling

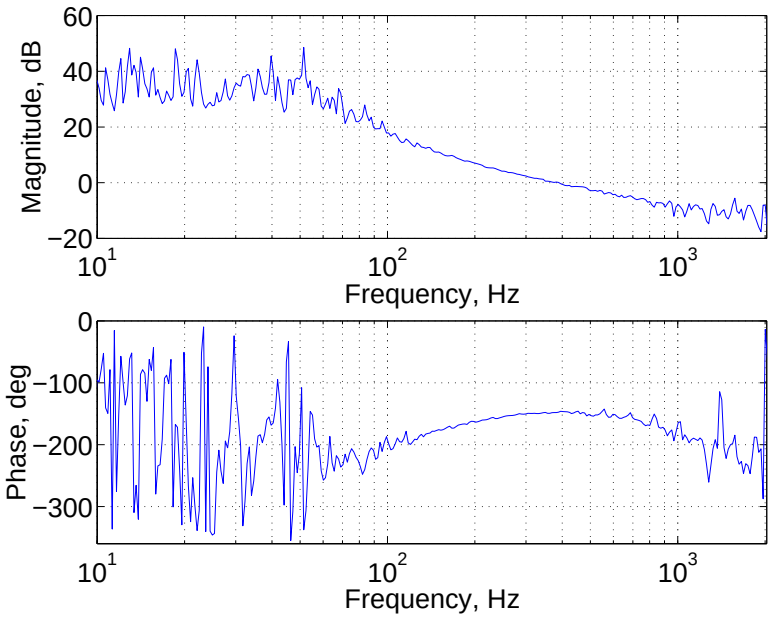

Figure 2-16. *Experimentally measured open-loop transfer function.*

frequency of 4050 Hz. This HDD will be further described in Section 3.1.5 as well as the details on how the experimental data was collected.

The experimentally measured frequency response of the plant, $P(q^{-1})$, for the Seagate 2.5" HDD is shown in Fig. 2-17. Between 50 Hz and 2 kHz, the plant behaves as a double integrator with a one step delay due to the sampling of the PES. Below 50 Hz, bearing effects dominate the double integrator response. The suspension modes are not evident since the first torsional mode as well as the other modes are above 2 kHz, and hence, above the Nyquist frequency of the HDD. This frequency response was modeled by the following discrete time transfer function

$$\frac{Y_{head}(z^{-1})}{U_{vcm}(z^{-1})} = \frac{0.8923z^{-1} + 2.4425z^{-2} + 0.3769z^{-3}}{1 - 2.1412z^{-1} + 1.3191z^{-2} - 0.1749z^{-3}}. \qquad (2\text{-}4)$$

The frequency response of the system described by Eq. (2-4) is depicted as the dashed line in Fig. 2-17. The model deviates below 50 Hz because the nonlinear effects of bearing friction and the flex circuit which are not modeled. However, above 50 Hz to 1 kHz, the frequency response of the model approximates the frequency response of the actual system quite well.

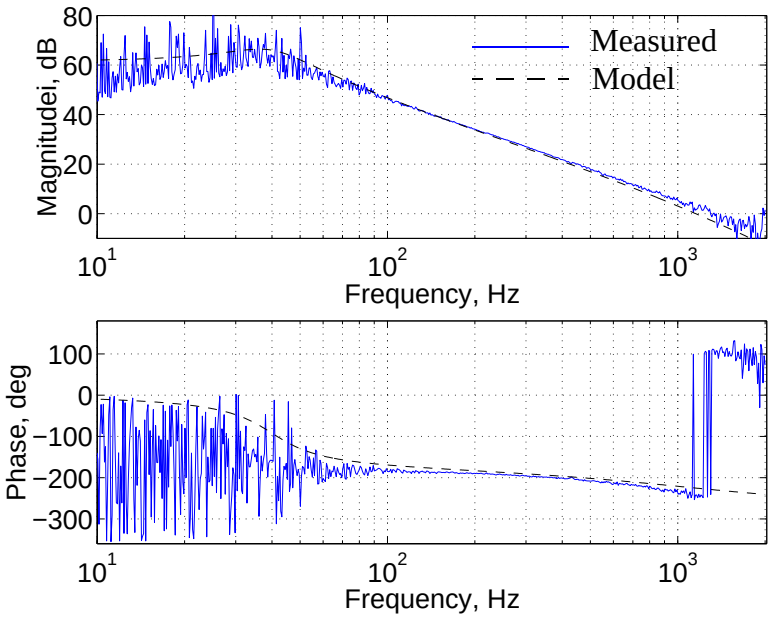

Figure 2-17. *Comparison of actual and modeled plant for the Seagate 2.5" HDD.*

The experimentally measured frequency response of the controller, $K(q^{-1})$ for the Seagate 2.5" HDD is shown in Fig. 2-18. It has the same structure as the response of the controller described in Section 2.3. The transfer function was modeled by the following discrete time transfer function

$$\frac{U_n(z^{-1})}{Y(z^{-1})} = \frac{0.3160 - 0.7445z^{-1} + 0.5661z^{-2} - 0.1357z^{-3}}{1 - 1.5766z^{-1} + 0.6540z^{-2} - 0.0773z^{-3}}. \qquad (2\text{-}5)$$

The frequency response of the system described by Eq. (2-5) is depicted as the dashed line in Fig. 2-18. Below 1 kHz, the frequency response of the model matches the frequency response of the actual controlled system very closely. Above 1 kHz, the frequency response of the actual system continues to rise because of the signal to noise ratio of the measurement is small and the electrical noise present in the measurement system dominates.

The experimentally measured frequency response of $(P(q^{-1}))/(1 + P(q^{-1})K(q^{-1}))$, i.e. the transfer function from $u(k)$ to $y(k)$, for the Seagate 2.5" HDD is shown in Fig. 2-19. The transfer function estimates of $P(q^{-1})$ and $K(q^{-1})$ were used to generated

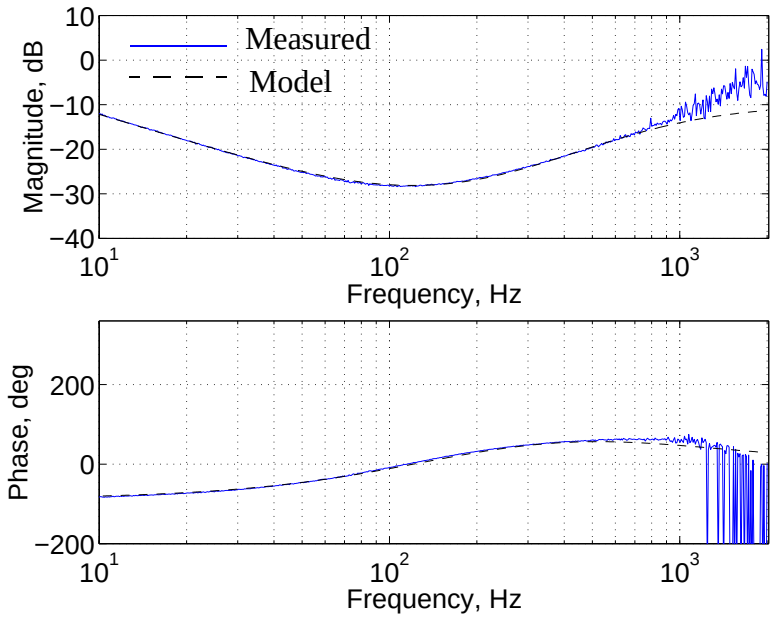

Figure 2-18. *Comparison of actual and modeled controller for the Seagate 2.5" HDD.*

the model of the following discrete time transfer function

$$\frac{Y_{head}(z^{-1})}{U(z^{-1})} = \frac{0.2436z^{-1} + 0.3192z^{-2} - 0.4831z^{-3} - 0.0798z^{-4}}{1 - 2.3860z^{-1} + 2.0886z^{-2} - 0.7889z^{-3} + 0.1071z^{-4}} \tag{2-6}$$

The frequency response of the system described by Eq. (2-6) is depicted by the dashed line in Fig. 2-19. Below 2 kHz, the frequency response of the model approximates the frequency response of the actual system quite adequately. Above 1 kHz, the frequency response diverges due to the low SNR of the experimental measurement.

The experimentally measured open-loop transfer function for the Seagate 2.5" HDD is shown in Fig. 2-20. The estimate of the open-loop transfer function was generated by multiplying Eq. (2-4) and Eq. (2-5) together. Below 50 Hz and above 1 kHz, the frequency response diverges from the model due to the modeling errors of $P(q^{-1})$ and $K(q^{-1})$. The phase and gain margins for the actual system are 31^o at 382 Hz and 6 dB at 753 Hz, respectively; while the phase and gain margins for the modeled system are 31^o at 382 Hz and 7 dB at 789 Hz, respectively. The models described by Eqs. (2-4) through (2-6) are used to generate the simulation results given in Section 4.5..

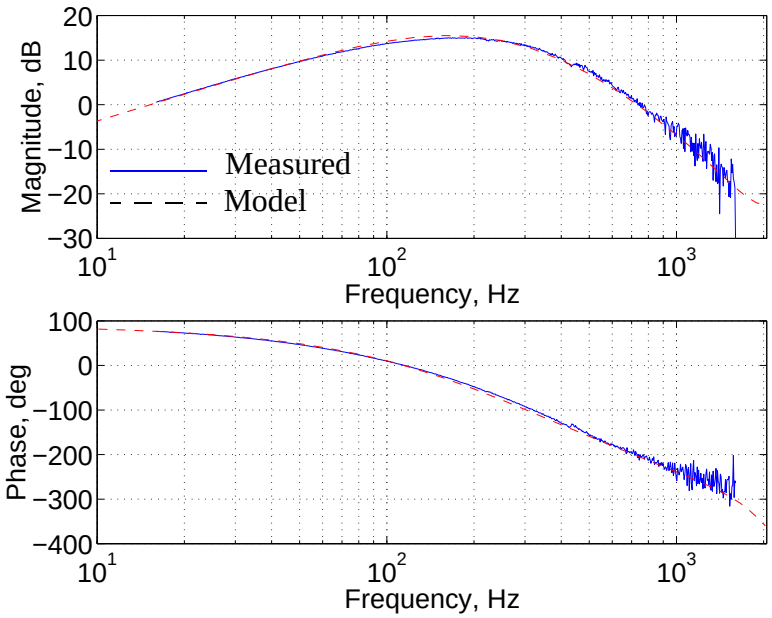

Figure 2-19. *Comparison of actual and modeled transfer function from u to y_{head} for the Seagate 2.5" HDD*

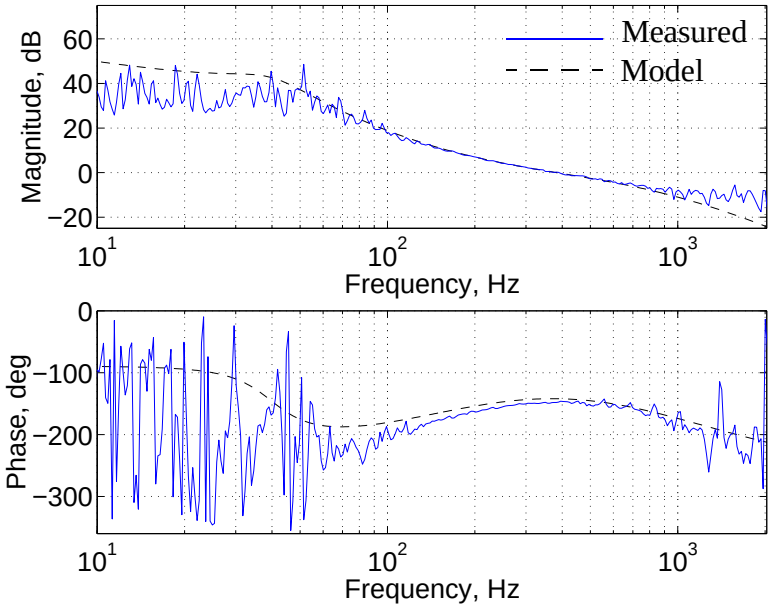

Figure 2-20. *Comparison of actual and modeled open-loop transfer function for the Seagate 2.5" HDD.*

3. EXPERIMENTAL SETUP

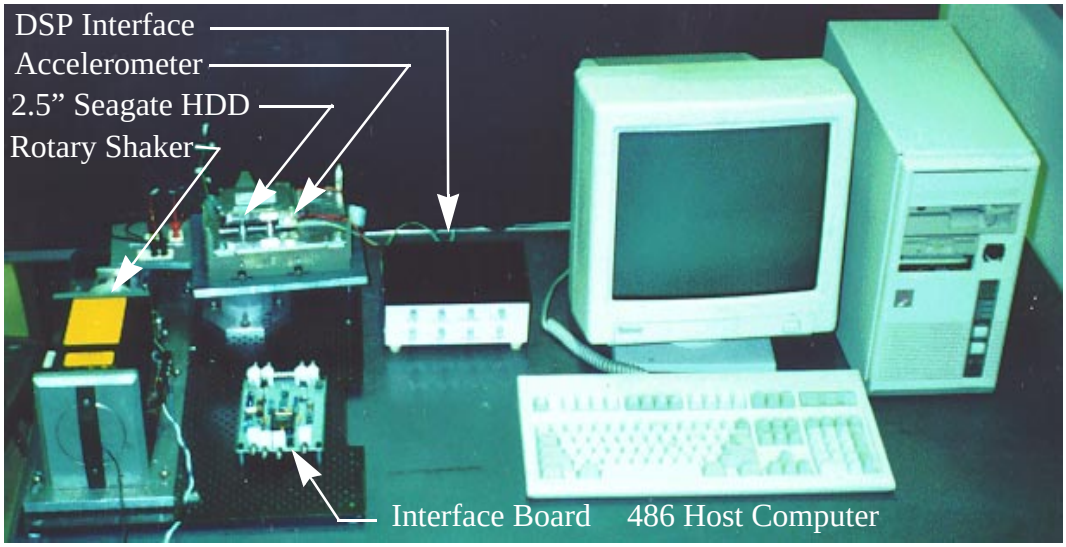

Figure 3-1. *Overview of experimental setup with all major components.*

3.1 OVERVIEW

The components involved in the experimental apparatus for testing the adaptive algorithm on HDD’s are shown in Fig. 3-1. These components are: Texas Instruments TMS320C40 Digital Signal Processor in a ‘486 host computer, Analog Devices ADXL05 accelerometers, shaker tables, interface board, and a 2.5” Seagate HDD. The ‘486 computer serves as the host computer for the HDD and the carrier board of the DSP. The motherboard of the DSP is mounted directly in the back plane of the ‘486 host computer. The HDD is located outside the ‘486 host since it must be mounted on a shaker table. Commands to the HDD are sent by the standard ATA interface used in the ‘486 host. The DSP and the HDD communicate through the interface board.

3.1.1 TMS320C40 DIGITAL SIGNAL PROCESSOR

The TMS320C40 is a 32-bit floating point DSP optimized for parallel processing. It can deliver up to $30 MIPS$ or $60 MFLOPS$. It is mounted on a Spectrum motherboard which can host up to 4 individual ‘C40 processors. Only one processor was used in the

experiments described in this dissertation.

A separate Burr-Brown analog daughter module was used for I/O. It housed two 16 bit ADC and DAC converters which communicate directly with the DSP. Both channels have a dynamic range of ±3 V. The maximum frequencies at which the ADC and DAC can be triggered were 200 kHz and 500 kHz respectively. These converter channels can either be triggered from an external convert pulse or an internal clock. The ADC and DAC samples were initiated on the rising edge of a TTL signal of minimum pulse width of 80 nsec. For implementation of the adaptive algorithm, the ADCs were triggered from an external signal synchronized with the PES (see Section 3.2.2). The DACs were triggered from an internal clock running at 200 kHz.

3.1.2 ACCELEROMETER SPECIFICATIONS

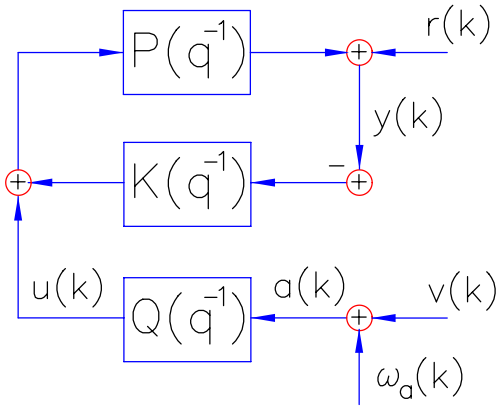

Figure 3-2. *Block diagram of a HDD system including the runout signal, the auxiliary controller signal, and the accelerometer signal.*

A number of factors must be considered when choosing an accelerometer for use in the disturbance rejection scheme presented in this dissertation. A simplified block diagram of a HDD system with the PES $y(k)$, the runout signal, $r(k)$, the auxiliary controller signal, $u(k)$, and the accelerometer signal, $a(k)$, is shown in Fig. 3-2. The runout is generated by the external disturbance, $v(k)$. The adaptive feedforward servo is represented by $Q(q^{-1})$. A more complete block diagram will be given in Section 4.1.

Ideally, an accelerometer should provide a perfect measurement of the external disturbance. However, electrical noise, sensing bandwidth, saturation, and other effects

contribute to the non-ideal behavior of accelerometers. In order to chose an accelerometer for this application, the first issue that should be addressed is the noise floor of the accelerometer. Electrical noise in accelerometers is modeled as the sum of a white noise signal and the measured disturbance. This white noise signal is denoted by $\omega_a(k)$ in Fig. 3-2. The magnitude of the variance for this white noise signal must be limited since it should not cause significant variations in the PES, $y(k)$. The relation between the variance of the PES and the accelerometer noise is

$$\Phi_{yy} = \left|\frac{PQ}{1+PK}\right|^2 \Phi_{aa}, \tag{3-1}$$

where Φ_{yy} is the variance of the PES and Φ_{aa} is the variance of the accelerometer noise.

As will be shown later, to minimize the variance of the PES with respect to external disturbances, $Q(q^{-1})$ should converge to the FIR filter which best approximated $P^{-1}(q^{-1})G_{shk}(q^{-1})$, neglecting the accelerometer dynamics, where $G_{shk}(q^{-1})$ represents the mechanical dynamics which convert the external disturbance to runout. Hence Eq. (3-1) becomes

$$\Phi_{yy} = \left|\frac{G_{shk}}{1+PK}\right|^2 \Phi_{aa}. \tag{3-2}$$

The transfer function given in Eq. (3-2) can be experimentally measured since it is the transfer function from external disturbance to PES. Hence, a measurement of the spectrum of the PES while the HDD was subjected to a random external disturbance will provide a means of obtaining the transfer function used in Eq. (3-2). Further, since experimentally generated models for the nominal plant and controller of the HDD are available and an estimate of $G_{shk}(q^{-1})$ can be obtained as will be shown in Section 5.2.2, the transfer function in Eq. (3-2) can be estimated. Employing either method, an upper bound for the accelerometer output noise variance can be calculated. Using the models from Section 2.4 and Section 5.2.2, the following relation can be obtained

$$\Phi_{yy} = \left(22.86\ \frac{TRK}{G}\right)^2 \Phi_{aa}, \tag{3-3}$$

where the units for Φ_{yy} are TRK^2/Hz and the units for Φ_{aa} are G^2/ Hz. Hence, for a

given upper bound of Φ_{yy}, the upper bound for Φ_{aa} can be determined from the following expression

$$\Phi_{aa} \leq \frac{1}{\left(22.86\ \frac{TRK}{G}\right)^2}\Phi_{yymax}. \tag{3-4}$$

In general, since the power spectral density of the nominal PES from a HDD is fairly flat excluding the repetitive runout, the nominal variance of the PES can be measured. This nominal Φ_{yy} is a logical choice for Φ_{yymax} since it is the noise floor of the PES. For the Seagate 2.5" HDD used in the experiments discussed here, the nominal Φ_{yy} was 0.0004 TRK^2/Hz. Hence, by Eq. (3-4), the upper bound for the variance for the output noise for the accelerometer is calculated to be $765*10^{-9}$ G^2/Hz. Taking the square root to get the standard deviation yields 875 $\mu G/Hz^{1/2}$. Hence, the noise floor of the accelerometer must be below 875 $\mu G/Hz^{1/2}$ to prevent the accelerometer output noise from affecting the variance of the PES.

The sensitivity of the accelerometer can be obtained from the maximum supply voltage available on the HDD and the maximum desired acceleration measurement. The voltage supplies for a 2.5" and 3.5" HDD's are +5 V and +12 V respectively. A degree of freedom is available in choosing the maximum desirable acceleration. Typical HDD are designed to reject external vibrational disturbances whose maximum value of acceleration is 2 G with just the nominal controller. Therefore the maximum detectable acceleration should be greater than 2 G. However, this level of external disturbance varies not only from different form factors of HDD's, but it also varies among different HDD manufactures. For example, 2.5" HDD's can undergo external vibrations exceeding 5 G in certain conditions. If 5 G is chosen as the maximum detectable acceleration, then for a 2.5" HDD, the sensitivity should be less than 500 mV/G since the supply voltage is +5 V. For a more thorough treatment of the design of accelerometers and the trade-offs between noise floor, sensitivity, and output swing, the reader is referred to [55].

The accelerometers used in these experiments were Analog Devices ADXL05s. The ADXL05 is a force-balanced capacitive single axis accelerometer which can be configured with the ability to measure ±5 G of acceleration[6]. The accelerometers were

configured such that they exhibited the properties listed in Table 3-1, including a single pole response with the bandwidth listed below. The ADXL05 satisfied the constrains given in the discussion above.

Characteristic	Value
Maximum Acceleration	±5 G
Sensitivity	200 mV/G
Noise Performance	500 μg/Hz$^{1/2}$
0 G output level	2.5 V
Full-scale swing about 0 G	±1 V
-3 dB crossover	1.6 kHz

Table 3-1. *Properties of ADXLO5 Accelerometer.*

Two accelerometers were mounted on the base casting of the HDD as shown in Fig. 3-3. The configuration displayed is for detecting rotary vibrational disturbances and shocks.

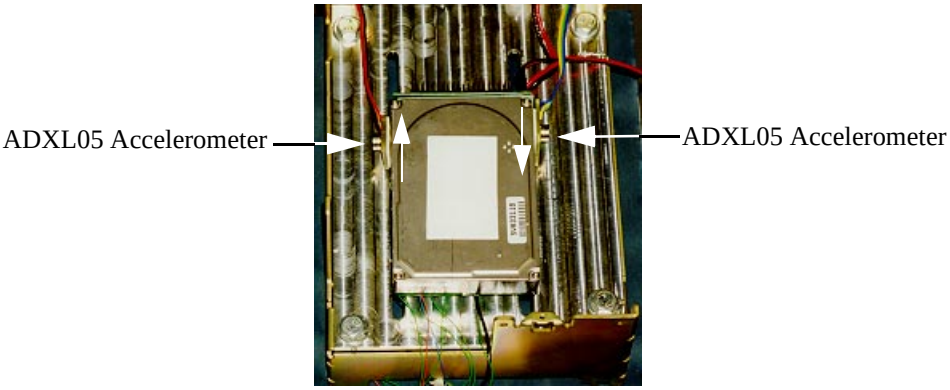

Figure 3-3. *Placement of single axis ADXL05 accelerometers for detection of rotary vibrations with axis of sensitivity marked with arrows on HDD.*

3.1.3 SHAKER TABLES

A custom fabricated rotary shaker was used to generate vibrational disturbances in the plane of the disk platters of the HDD. This rotary shaker was designed and built by a previous CML student, Matthew T. White[88]. It consisted of a VCM from an old HDD connected to a rotary platform. It is displayed in Fig. 3-1. The HDD can be subject to rotary and linear disturbances by varying the mounting configuration. It has the capacity

of producing linear accelerations of ±4 G over a 300 Hz bandwidth. A Bruel & Krael shaker was used to subject the HDD to vibrational disturbances parallel to the spindle axis. It has the capacity of producing linear accelerations of ±10 G over a 10 kHz bandwidth.

3.1.4 INTERFACE BOARD

The interface board received the PES data from the HDD and the accelerometer signals and shifted them to the proper level to be read by the ADCs of the DSP. It also accepted the control signal from the DACs of the DSP and shifted it to the appropriate level to be injected into the HDD. Further it generated a digital signal used to trigger the DSP to sample the PES signal. The interface board will be described more fully in Section 3.2.

3.1.5 SEAGATE 2.5" HARD DISK DRIVE

The HDD used in the experiments was a Seagate 2.5" ST-9816AG. This HDD was released to the market early in 1995. The properties of the HDD are listed in Table 3-2.

Characteristic	Value
Form Factor	2.5"
Formatted Capacity	810 Mb
Volts per Track	3.43 V
Tracks per Inch	3807
Bits per Inch	90,000
Spindle Frequency	75 Hz
Number of Heads	8
Number of Disks	4
Operating Shock	100 G
Nonoperating Shock	250 G

Table 3-2. *Properties of the Seagate 2.5" ST-9816AG HDD.*

The HDD was modified such that various signals including the PES could be extracted and an exogenous signal could be send to the VCM driver. The signals which can be injected and extracted from the HDD are displayed in Fig. 3-4. The exogenous signal $u_c(t)$ is the input to the VCM driver. The PES, the nominal controller signal, and the combined controller signal are denoted by $y_c(t)$, $u_{nc}(t)$, and $u_{tc}(t)$ respectively. All

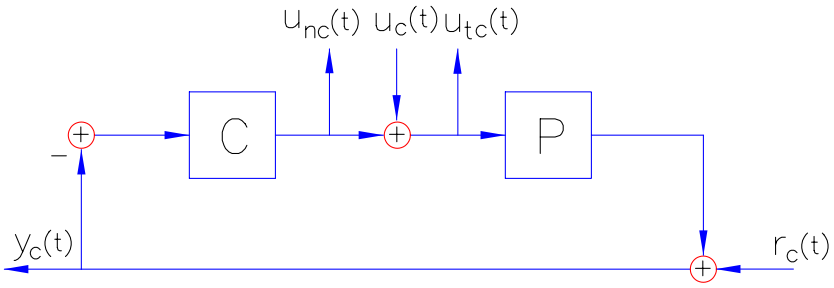

Figure 3-4. *Signals available from Seagate HDD for use in experiments.*

these signals can be measured. The total runout is denoted by $r_c(t)$ and cannot be measured. To measure the various transfer functions in the loop, white noise was injected into the HDD through $u_c(t)$. It had to be of sufficient magnitude to overwhelm the PES caused by the nominal $r_c(t)$. The following transfer functions were measured using this method

$$\begin{aligned} \frac{Y_c(s)}{U_{tc}(s)} &\approx P(s), \\ \frac{U_{nc}(s)}{-Y_c(s)} &\approx K(s), \\ \frac{-U_{nc}(s)}{U_{tc}(s)} &\approx P(s)K(s), \end{aligned} \tag{3-5}$$

and

$$\frac{Y_c(s)}{U_c(s)} \approx \frac{P(s)}{1+P(s)K(s)}. \tag{3-6}$$

This method was used to obtain the experimental data for the figures in Section 2.3 and Section 2.4.

3.2 Interfacing with the Hard Disk Drive

In order to implement the add-on adaptive controller, an interface board had to be developed in order to allow access to PES and send a control signal to the VCM driver. Further, since the PES was available only at discrete intervals, a triggering signal had to be generated in order to synchronize the ADCs of the DSP with the PES.

3.2.1 PES OFFSET

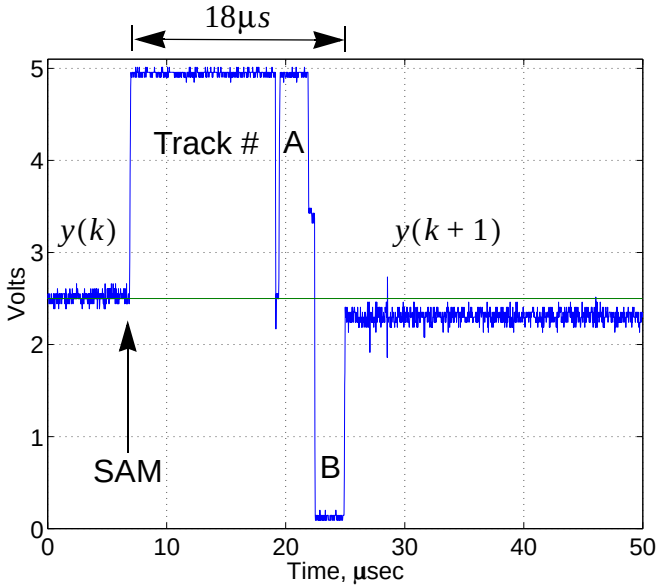

Figure 3-5. *Measured PES directly from HDD. The different features of the servo sector are distinguishable.*

A segment of the PES as read directly from the HDD is displayed in Fig. 3-5. The first section of the signal contains the PES value from the previous servo section $y(k)$ which is held constant until the new servo sector is reached. As stated in Section 2.1.1, the start of each servo sector is marked with a servo address mark. As shown in the Fig. 3-5, the PES transitions to 4.9 V as the R/W head passes over the SAM and the track number. It then transitions from 4.9 V to 0.1 V as the R/W head flies over the A and B bursts. Finally the new value of the PES, $y(k+1)$, is calculated and sent out. The new PES is available approximately 18 μsec after the SAM is reached. This cycle repeats every 250 μsec when a new servo sector is reached. Since the Seagate 2.5" HDD is powered from 5 V supply, the dynamic range of the PES is 0.1 V to 4.9 V, centered about 2.5 V. However, the ADCs of the DSP accepts only ±3 V inputs. To remove the DC bias, the PES is filtered by a passive high pass filter to AC couple the signal. The disadvantage of this method is that DC tracking errors cannot be compensated for by the add-on compensator. However, since the nominal compensator contains integral action, DC tracking errors are already attenuated. Fig. 3-6 shows the circuit used to AC couple the PES. The low frequency pole was placed at 0.4 Hz.

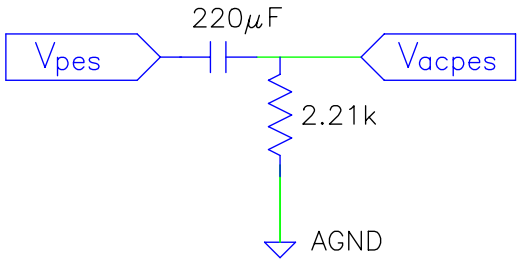

Figure 3-6. *RC filter for AC coupling of the PES.*

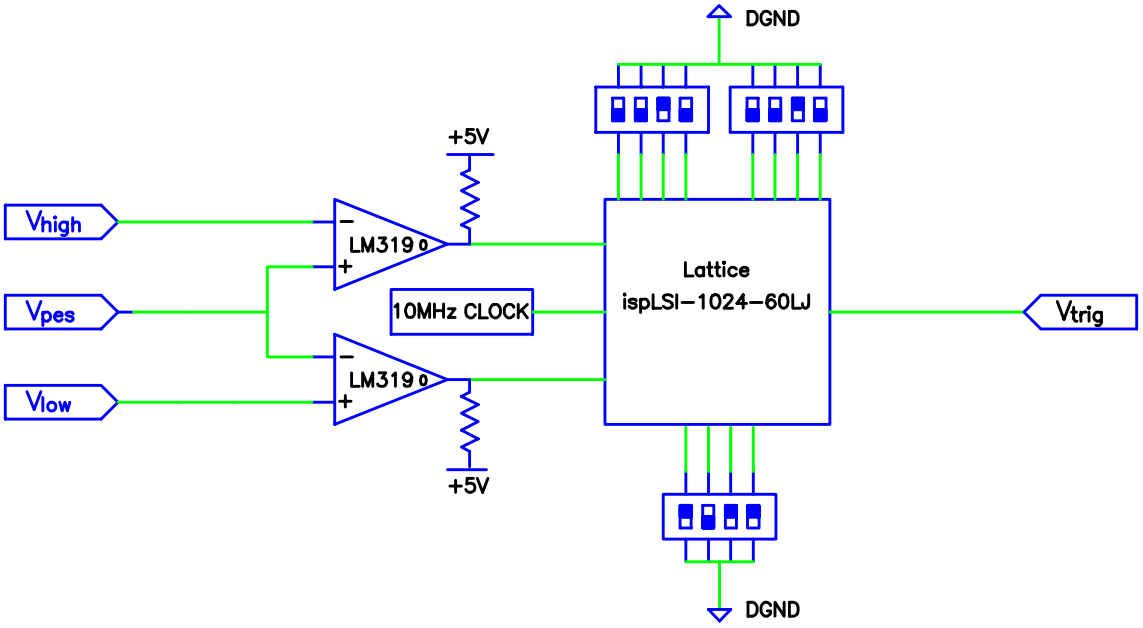

Figure 3-7. *Schematic of circuitry to generate external trigger for the ADCs of the DSP.*

3.2.2 DSP TRIGGER SIGNAL

In order to trigger the ADCs of the DSP with the PES, an external pulse must be generated. For the DSP to read the correct value of the PES, it must be triggered a few mircoseconds after the new PES value is available. Fig. 3-7 shows the circuitry designed to generate the external pulse. It consists of a pair of LM319 comparators, a 10 MHz clock, three 4 pin DIP switches, and an ispLSI-1024-60LJ Lattice chip. The ispLSI-1024-60LJ is an in-system programmable large scale logic device[51]. It allows for a finite state machine to be implemented in digital logic. More detail about the function of this chip will be given in Section 3.2.2. The timing diagram is shown in Fig. 3-8. The comparator's low and high signals are generated when the PES goes below

V_{low} and above V_{high} respectively. V_{low} and V_{high} are set to 4.8 V and 0.2 V. Hence, the transition of the PES from 4.9 V to 0.1 V is captured by the Lattice chip. Using these two inputs, the Lattice chip produces a TTL compatible pulse at the appropriate time to read the PES. After a time delay of *delay 1*, a pulse of width *delay 2* is generated by the Lattice chip. A second pulse of the same width as the first is generated *delay 3* after the first pulse. All these delays are user configurable using the 4 pin DIP switches shown in Fig. 3-7. The reason for the second pulse lies in the way the data is passed from the registers of the ADC and the registers of the 'C40. At the rising edge of the first pulse, the ADC samples the PES and converts the analog signal to a 16 bit digital number stored in the Burr-Brown module's local register. Instead of immediately transferring this data to the 'C40 registers, the Burr-Brown module holds it until the next conversion pulse. Without the second trigger pulse, the 'C40 would receive PES information which was delayed one sampling period. To remove this delay, the second pulse is generated to transfer the sampled PES to the 'C40 resister for use in calculations. Rather than a one sample delay, the delay is now approximately *delay 2* + *delay 3*. The minimum duration of this delay is 5 μsec. This same delay also applies to the DACs. For these experiments, the DACs were triggered from a 200 kHz internal clock which results in a 10 μsec delay.

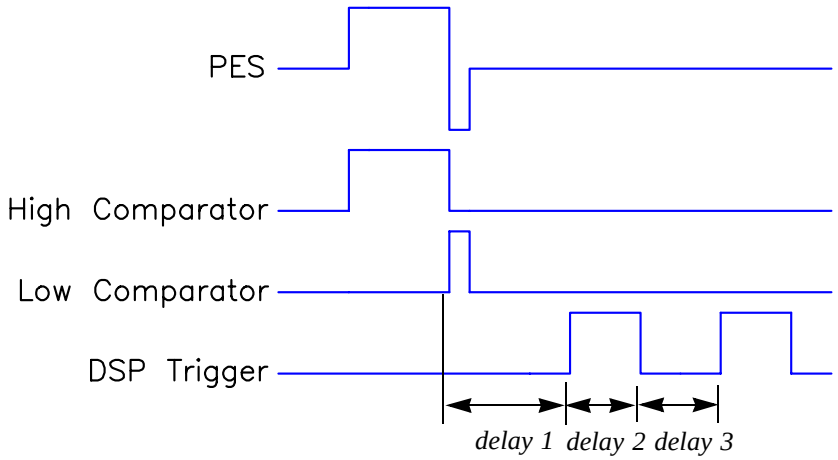

Figure 3-8. *DSP trigger timing diagram with the delays due to the sampling with the 'C40.*

To verify that the above circuit was operating correctly, the AC-coupled PES was sampled and then immediately sent out. These signals along with the trigger were viewed using an oscilloscope and the traces were saved. The comparison of the sampled PES

(from the DSP) and the AC-coupled PES is displayed in Fig. 3-9. The magnitude of the trigger signal was scaled such that it would display in the figure. The sampled PES does not change until 10 μsec after the second triggering pulse because of the two step delay of the DACs. The total delay from the time the new value of PES is available from the HDD to when it is available in the DSP is 20 μsec. There is a bias between the sampled PES and the AC-coupled PES. This bias results from the electrical noise in the circuit. The mean of the difference between these two signals is 0 with a 3σ deviation of 0.14 V. USing the conversion of 3.43 V from volts to tracks, this mean difference is 4% of a track width. Hence, the electrical noise can only cause the sampled PES to be 4% of a track width from the actual PES.

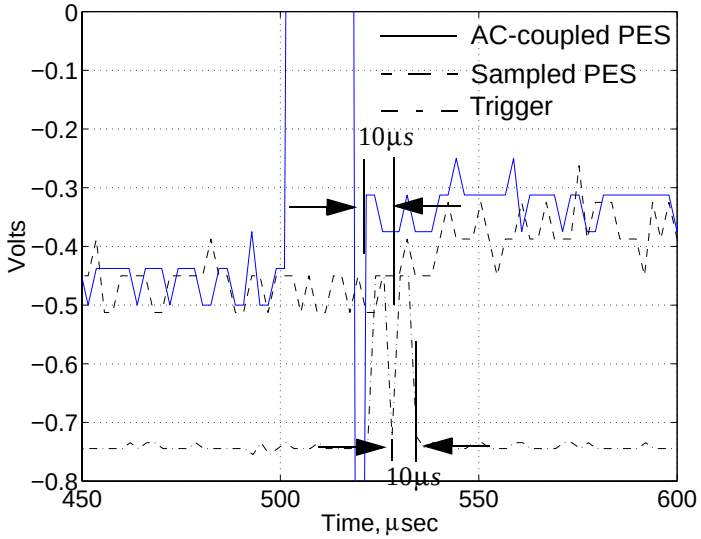

Figure 3-9. *Comparison of sampled PES and AC-coupled PES.*

A ispLSI-1024-60LJ Lattice chip was used to implement the finite state machine that is described by the state transition diagram in Fig. 3-10. There are six states that are needed to generate the trigger signal described in Section 3.2.2. State 0 waits for the high comparator to transition to logical 1 (5 V) which is denoted by the statement 'highc = 1?'. The trigger signal is set to logical 0 (0 V). A counter variable designated as count is set to 0. State 1 waits for the transition of the low comparator to logical 1 with the trigger set to logical 0. Once the transition of the PES signal from 0.1 V to 4.9 V is captured, the system remains in State 2 until the user specified time of *delay 1*. The values of all the

delays are selectable by the 4 pin DIP switches. The delays are 8 bit values inside the Lattice chip with the four least significant bits permanently set to 1. Hence the minimum and maximum delays are 15 and 255 counts respectively with discrete values available in between. Since the Lattice chip is running with a 10 MHz clock, each count represents 100 ns. Hence, delays of 1.5 µs to 25.5 µs are selectable. After *delay 1*, State 2 transitions to State 3 with *count* set to 0. In State 3, *trigger* is set to logical 1, and the transition to State 4 occurs after *delay 2*. State 4 resets *trigger* to logical 0 and waits for time *delay 3* before transitioning in State 5 which generates another pulse. State 5 then transitions to State 0 to wait for the next SAM. Specific details regarding the programming of the Lattice chip is listed in Appendix B2.

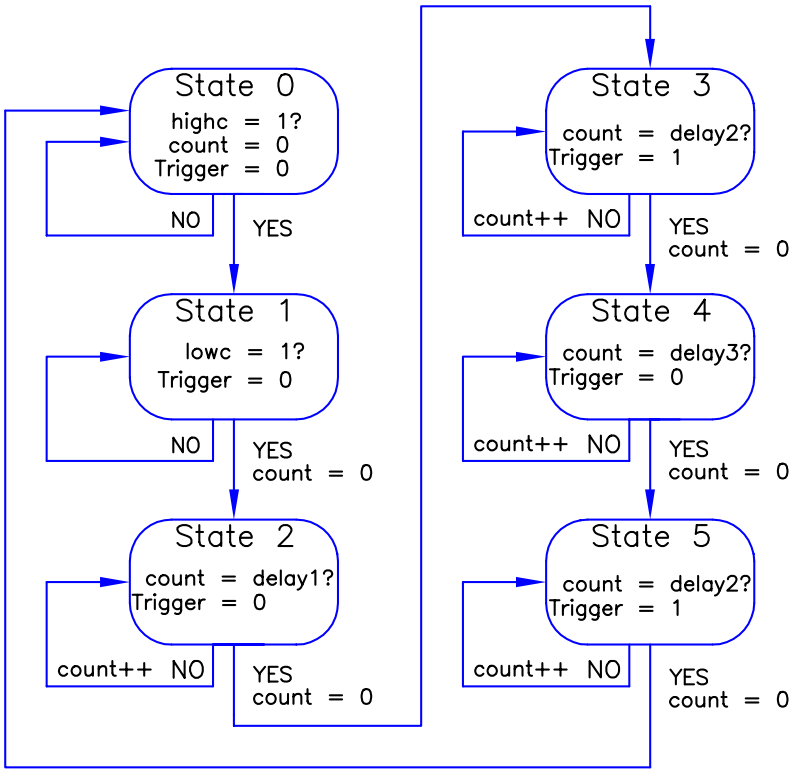

Figure 3-10. *State transition diagram of the program for the programmable logic chip.*

3.2.3 INPUT TO VCM DRIVER

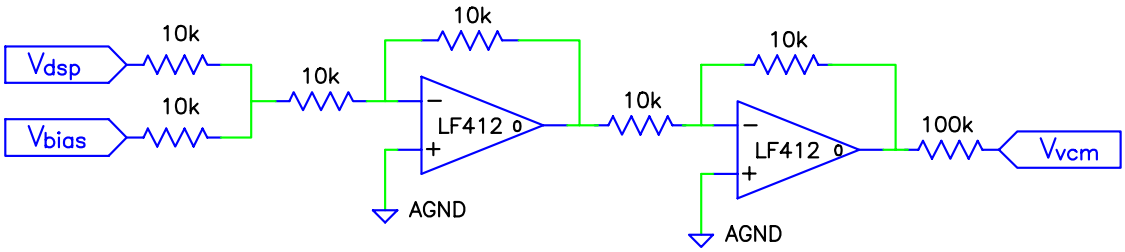

Figure 3-11. *Schematic of output circuitry with summing amplifiers.*

The schematic for the output circuitry is shown in Fig. 3-11. The output circuitry receives the control voltage from the DAC of the DSP, adds the appropriate bias, and scales it to the appropriate level. The input to the VCM driver must be 2.5±0.200 V. The control voltage from the DAC of the DSP is first summed with the bias voltage which is 2.5 V. The combined signal is then passed through an inverting amplifier to correct for the sign inversion from the summer. The result is then sent to the VCM driver of the HDD through a 100 kΩ resistor. Since V_{vcm} is also passed through a summing stage in the PCB of the HDD with a feedback resistance of 16.1 kΩ, the 100 kΩ resistor allows the maximum value of V_{dsp} to be ±1.2 V. The larger output swing from the DAC of the DSP allows for a higher SNR between the calculated value of control and the value sent to the VCM driver.

3.3 SOFTWARE

3.3.1 AT-ATTACHMENT INTERFACE

Standard commands can be sent to the HDD through the ATA interface. The commands are available using interrupt vector 0x13 which is the primary disk interface for the ROM BIOS[43]. A few of the available commands are listed in Table 3-3.

Command	Resistor Value
Reset HDD	0x00
Get Status	0x01
Get HDD Parameter	0x08

Table 3-3. *Brief listing of ATA interface commands for HDD.*

Command	Resistor Value
Initialize HDD Controller	0x09
Seek to Specific Cylinder	0x0c
Recalibrate HDD	0x11
HDD Controller Diagnostic	0x12
HDD Internal Diagnostic	0x14

Table 3-3. *Brief listing of ATA interface commands for HDD.*

These commands must be run with the computer in DOS. These commands will not function properly under Windows™† environment. Listed below is sample code which uses the seek to specified cylinders command.

```
#include<stdio.h>
#include<dos.h>

main(void)
{
   struct REGPACK reg;

// Load CPU registers with the proper data.                    //
// r_ax contains the code which idicated the seek command.     //
// r_cx the upper 8-bits contain the cylinder number.          //
// r_dx selects master or slave drive.                         //

   reg.r_ax = 0x0C00;
   reg.r_cx = 0x0000;
   reg.r_dx = 0x0081;

// Perform command by invoking interrupt13.                    //
   intr(0x13,&reg);
// Print status, 0x00 means successful completion of command.  //
   printf("%d \n",reg.r_ax>>8);
}
```

Modern HDD's have power management features built into their embedded control software. They allow the drive to minimize its power requirements during periods of inactivity. Commonly, the power management features are disabled by default on 3.5" HDD's. The HDD will continue to spin and respond to interface commands immediately no matter how infrequently it is accessed. However, for the Seagate 2.5" HDD used in

†Windows is a trademark of the Microsoft Corporation.

these experiments, the power management features are enabled by default since 2.5” HDD are often used in portable computers where power is limited. After 5 seconds, the HDD enters into an idle mode where the nominal compensator is off and no PES information is available. This feature is detrimental during experiments, so it was disabled. Listed below is the code to disable the power management features. A more detailed description of the commands below can be found in the AT-Attachment interface guide[20].

```
#include<stdio.h>
#include<dos.h>
#include<conio.h>

// Define pointer to store old ISR.                                    //
void interrupt (*oldhandle)(_CPPARGS);

// Define new ISR function which executes old ISR.                     //
void interrupt handle(_CPPARGS)        //
{
   oldhandle();
}

main(void)
{
   unsigned char status;

   disable();                 // Disable all interrupts.
   oldhandle = getvect(0x14); // Get current interrupt vector.
   setvect(0x14,handle);      // Set interrupt vector to handle.
   enable();                  // Enable all interrupts.

   outportb(0x1f0,0x00);      // Disable power management features.
   outportb(0x1f1,0x01);      // Disable power management features.
   outportb(0x1f2,0x55);      // Sector count.
   outportb(0x1f3,0x46);      // Sector number.
   outportb(0x1f4,0x4E);      // Low byte of cylinder number.
   outportb(0x1f5,0x55);      // High byte of cylinder number.
   outportb(0x1f6,0xB0);      // Head number.
   outportb(0x1f7,0xf7);      // Implement command.
   status = inportb(0x1f7);   // Read status of command, 0x50 is
                                 successful completion.
   disable();                 // Disable all interrupts.
   setvect(0x14,oldhandle);   // Set interrupt vector to oldhandle.
   enable();                  // Enable all interrupts.
}
```

3.3.2 DSP SOFTWARE

As stated above, the ADCs were triggered from an external signal synchronized with the PES, and the DACs were triggered from an internal clock running at 200 kHz. The external signal that was used to initiate conversions by the ADCs was also used to cause the DSP to enter an Interrupt Service Routine. It was inside the ISR that the adaptive control output was calculated and the identification algorithms were updated. Listed below is sample code that configures the DSP as stated above. A more complete listing of the DSP program can be found in Appendix B.

```
#include<intpt40.h>        // Realtime interrupt support functions.
#include<carrier.h>        // Pointers to the DSPLINK registers.
#include<stdio.h>

void c_int04(void);        // Function prototype for ISR.

main(void)
{
   volatile unsigned int temp;

// Need to perform an IACK instruction to allow external interrupts //
// through to the ‘C40.                                              //

   asm(“Push AR0”);
   asm(“Push DP”);
   asm(“LDI 030H,AR0”);
   asm(“LSH 16,AR0”);
   asm(“IACK *AR0”);
   asm(“POP DP”);
   asm(“POP AR0”);

   INT_DISABLE();             // Disable all interrupts.

// Set the ISR to be c_int04.  The function c_int04 will contain  //
// the C code to implement the adaptive algorithm.                //
   install_int_vector((void *)c_int04, 0x04);
   load_iif(0x00B0)l          // Set ISR to be level triggered.

   temp = *DM1_RESET;         // Reset Burr Brown board.

// Set ADCs to sample when external trigger occurs and DACs to    //
// trigger off internal clock.                                    //
   *DM1_ROUTE = 0x000E0000;
```

```
    *DM1_AMELIA_CTRL = 0x00A20000;

// Set the ISR to run when ADCs are finished.
    *DM1_INT_MASK = 0x00010000;

// Set the internal clock to 200kHz.
    *DM1_INT_MASK = 0xFFC40000;
    *DM1_CONFIGURATION = 0x8DFF0000;    // Load configuration.
    INT_ENABLE();              // Enable all interrupts.

}
```

3. EXPERIMENTAL SETUP

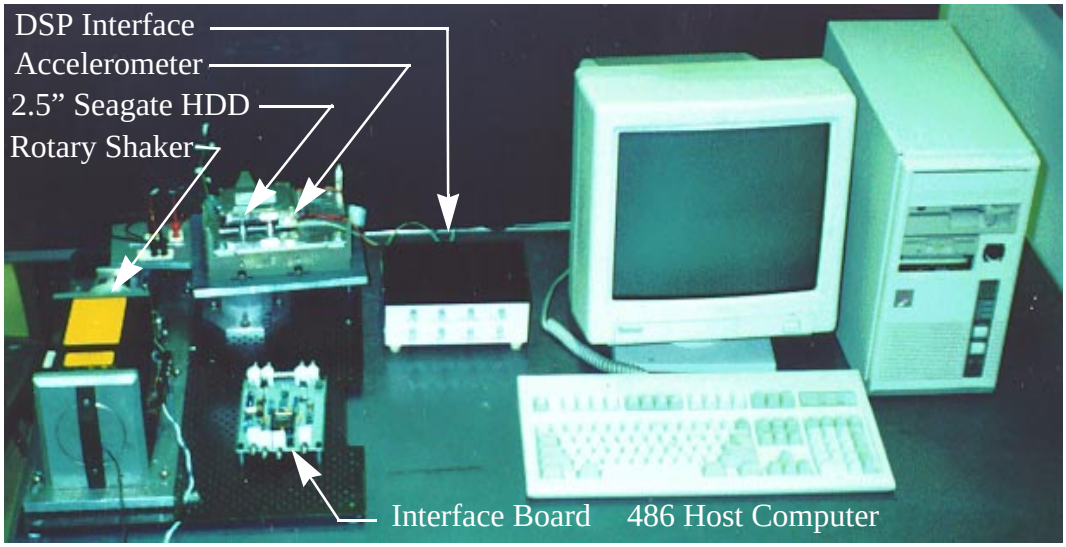

Figure 3-1. *Overview of experimental setup with all major components.*

3.1 OVERVIEW

The components involved in the experimental apparatus for testing the adaptive algorithm on HDD’s are shown in Fig. 3-1. These components are: Texas Instruments TMS320C40 Digital Signal Processor in a ‘486 host computer, Analog Devices ADXL05 accelerometers, shaker tables, interface board, and a 2.5” Seagate HDD. The ‘486 computer serves as the host computer for the HDD and the carrier board of the DSP. The motherboard of the DSP is mounted directly in the back plane of the ‘486 host computer. The HDD is located outside the ‘486 host since it must be mounted on a shaker table. Commands to the HDD are sent by the standard ATA interface used in the ‘486 host. The DSP and the HDD communicate through the interface board.

3.1.1 TMS320C40 DIGITAL SIGNAL PROCESSOR

The TMS320C40 is a 32-bit floating point DSP optimized for parallel processing. It can deliver up to $30 MIPS$ or $60 MFLOPS$. It is mounted on a Spectrum motherboard which can host up to 4 individual ‘C40 processors. Only one processor was used in the

experiments described in this dissertation.

A separate Burr-Brown analog daughter module was used for I/O. It housed two 16 bit ADC and DAC converters which communicate directly with the DSP. Both channels have a dynamic range of ±3 V. The maximum frequencies at which the ADC and DAC can be triggered were 200 kHz and 500 kHz respectively. These converter channels can either be triggered from an external convert pulse or an internal clock. The ADC and DAC samples were initiated on the rising edge of a TTL signal of minimum pulse width of 80 nsec. For implementation of the adaptive algorithm, the ADCs were triggered from an external signal synchronized with the PES (see Section 3.2.2). The DACs were triggered from an internal clock running at 200 kHz.

3.1.2 ACCELEROMETER SPECIFICATIONS

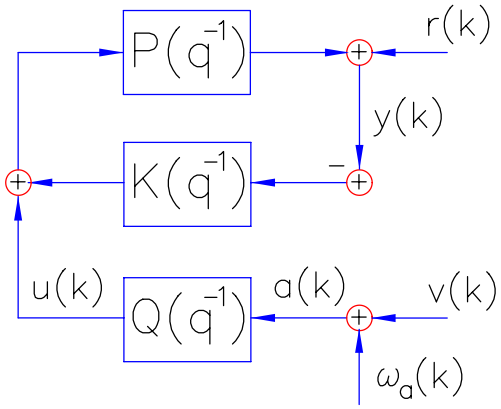

Figure 3-2. *Block diagram of a HDD system including the runout signal, the auxiliary controller signal, and the accelerometer signal.*

A number of factors must be considered when choosing an accelerometer for use in the disturbance rejection scheme presented in this dissertation. A simplified block diagram of a HDD system with the PES $y(k)$, the runout signal, $r(k)$, the auxiliary controller signal, $u(k)$, and the accelerometer signal, $a(k)$, is shown in Fig. 3-2. The runout is generated by the external disturbance, $v(k)$. The adaptive feedforward servo is represented by $Q(q^{-1})$. A more complete block diagram will be given in Section 4.1.

Ideally, an accelerometer should provide a perfect measurement of the external disturbance. However, electrical noise, sensing bandwidth, saturation, and other effects

contribute to the non-ideal behavior of accelerometers. In order to chose an accelerometer for this application, the first issue that should be addressed is the noise floor of the accelerometer. Electrical noise in accelerometers is modeled as the sum of a white noise signal and the measured disturbance. This white noise signal is denoted by $\omega_a(k)$ in Fig. 3-2. The magnitude of the variance for this white noise signal must be limited since it should not cause significant variations in the PES, $y(k)$. The relation between the variance of the PES and the accelerometer noise is

$$\Phi_{yy} = \left|\frac{PQ}{1+PK}\right|^2 \Phi_{aa}, \tag{3-1}$$

where Φ_{yy} is the variance of the PES and Φ_{aa} is the variance of the accelerometer noise.

As will be shown later, to minimize the variance of the PES with respect to external disturbances, $Q(q^{-1})$ should converge to the FIR filter which best approximated $P^{-1}(q^{-1})G_{shk}(q^{-1})$, neglecting the accelerometer dynamics, where $G_{shk}(q^{-1})$ represents the mechanical dynamics which convert the external disturbance to runout. Hence Eq. (3-1) becomes

$$\Phi_{yy} = \left|\frac{G_{shk}}{1+PK}\right|^2 \Phi_{aa}. \tag{3-2}$$

The transfer function given in Eq. (3-2) can be experimentally measured since it is the transfer function from external disturbance to PES. Hence, a measurement of the spectrum of the PES while the HDD was subjected to a random external disturbance will provide a means of obtaining the transfer function used in Eq. (3-2). Further, since experimentally generated models for the nominal plant and controller of the HDD are available and an estimate of $G_{shk}(q^{-1})$ can be obtained as will be shown in Section 5.2.2, the transfer function in Eq. (3-2) can be estimated. Employing either method, an upper bound for the accelerometer output noise variance can be calculated. Using the models from Section 2.4 and Section 5.2.2, the following relation can be obtained

$$\Phi_{yy} = \left(22.86\ \frac{TRK}{G}\right)^2 \Phi_{aa}, \tag{3-3}$$

where the units for Φ_{yy} are TRK^2/Hz and the units for Φ_{aa} are G^2/ Hz. Hence, for a

given upper bound of Φ_{yy}, the upper bound for Φ_{aa} can be determined from the following expression

$$\Phi_{aa} \leq \frac{1}{\left(22.86\ \frac{TRK}{G}\right)^2}\Phi_{yymax}. \tag{3-4}$$

In general, since the power spectral density of the nominal PES from a HDD is fairly flat excluding the repetitive runout, the nominal variance of the PES can be measured. This nominal Φ_{yy} is a logical choice for Φ_{yymax} since it is the noise floor of the PES. For the Seagate 2.5" HDD used in the experiments discussed here, the nominal Φ_{yy} was 0.0004 TRK^2/Hz. Hence, by Eq. (3-4), the upper bound for the variance for the output noise for the accelerometer is calculated to be $765*10^{-9}$ G^2/Hz. Taking the square root to get the standard deviation yields 875 $\mu G/Hz^{1/2}$. Hence, the noise floor of the accelerometer must be below 875 $\mu G/Hz^{1/2}$ to prevent the accelerometer output noise from affecting the variance of the PES.

The sensitivity of the accelerometer can be obtained from the maximum supply voltage available on the HDD and the maximum desired acceleration measurement. The voltage supplies for a 2.5" and 3.5" HDD's are +5 V and +12 V respectively. A degree of freedom is available in choosing the maximum desirable acceleration. Typical HDD are designed to reject external vibrational disturbances whose maximum value of acceleration is 2 G with just the nominal controller. Therefore the maximum detectable acceleration should be greater than 2 G. However, this level of external disturbance varies not only from different form factors of HDD's, but it also varies among different HDD manufactures. For example, 2.5" HDD's can undergo external vibrations exceeding 5 G in certain conditions. If 5 G is chosen as the maximum detectable acceleration, then for a 2.5" HDD, the sensitivity should be less than 500 mV/G since the supply voltage is +5 V. For a more thorough treatment of the design of accelerometers and the trade-offs between noise floor, sensitivity, and output swing, the reader is referred to [55].

The accelerometers used in these experiments were Analog Devices ADXL05s. The ADXL05 is a force-balanced capacitive single axis accelerometer which can be configured with the ability to measure ±5 G of acceleration[6]. The accelerometers were

configured such that they exhibited the properties listed in Table 3-1, including a single pole response with the bandwidth listed below. The ADXL05 satisfied the constrains given in the discussion above.

Characteristic	Value
Maximum Acceleration	±5 G
Sensitivity	200 mV/G
Noise Performance	500 μg/Hz$^{1/2}$
0 G output level	2.5 V
Full-scale swing about 0 G	±1 V
-3 dB crossover	1.6 kHz

Table 3-1. *Properties of ADXLO5 Accelerometer.*

Two accelerometers were mounted on the base casting of the HDD as shown in Fig. 3-3. The configuration displayed is for detecting rotary vibrational disturbances and shocks.

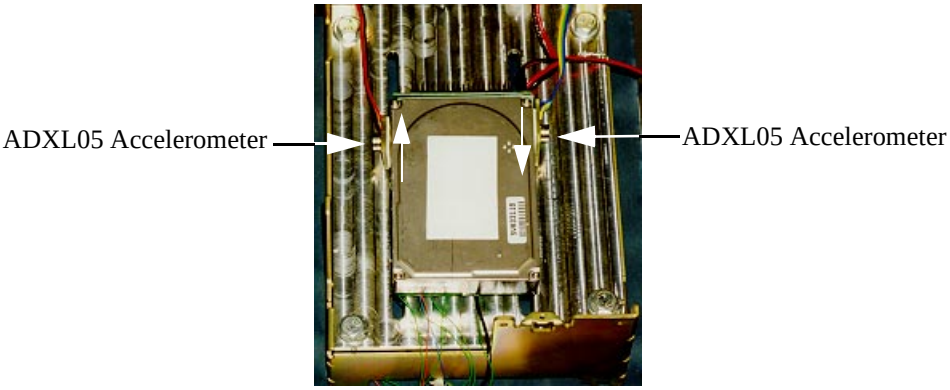

Figure 3-3. *Placement of single axis ADXL05 accelerometers for detection of rotary vibrations with axis of sensitivity marked with arrows on HDD.*

3.1.3 SHAKER TABLES

A custom fabricated rotary shaker was used to generate vibrational disturbances in the plane of the disk platters of the HDD. This rotary shaker was designed and built by a previous CML student, Matthew T. White[88]. It consisted of a VCM from an old HDD connected to a rotary platform. It is displayed in Fig. 3-1. The HDD can be subject to rotary and linear disturbances by varying the mounting configuration. It has the capacity

of producing linear accelerations of ±4 G over a 300 Hz bandwidth. A Bruel & Krael shaker was used to subject the HDD to vibrational disturbances parallel to the spindle axis. It has the capacity of producing linear accelerations of ±10 G over a 10 kHz bandwidth.

3.1.4 INTERFACE BOARD

The interface board received the PES data from the HDD and the accelerometer signals and shifted them to the proper level to be read by the ADCs of the DSP. It also accepted the control signal from the DACs of the DSP and shifted it to the appropriate level to be injected into the HDD. Further it generated a digital signal used to trigger the DSP to sample the PES signal. The interface board will be described more fully in Section 3.2.

3.1.5 SEAGATE 2.5" HARD DISK DRIVE

The HDD used in the experiments was a Seagate 2.5" ST-9816AG. This HDD was released to the market early in 1995. The properties of the HDD are listed in Table 3-2.

Characteristic	Value
Form Factor	2.5"
Formatted Capacity	810 Mb
Volts per Track	3.43 V
Tracks per Inch	3807
Bits per Inch	90,000
Spindle Frequency	75 Hz
Number of Heads	8
Number of Disks	4
Operating Shock	100 G
Nonoperating Shock	250 G

Table 3-2. *Properties of the Seagate 2.5" ST-9816AG HDD.*

The HDD was modified such that various signals including the PES could be extracted and an exogenous signal could be send to the VCM driver. The signals which can be injected and extracted from the HDD are displayed in Fig. 3-4. The exogenous signal $u_c(t)$ is the input to the VCM driver. The PES, the nominal controller signal, and the combined controller signal are denoted by $y_c(t)$, $u_{nc}(t)$, and $u_{tc}(t)$ respectively. All

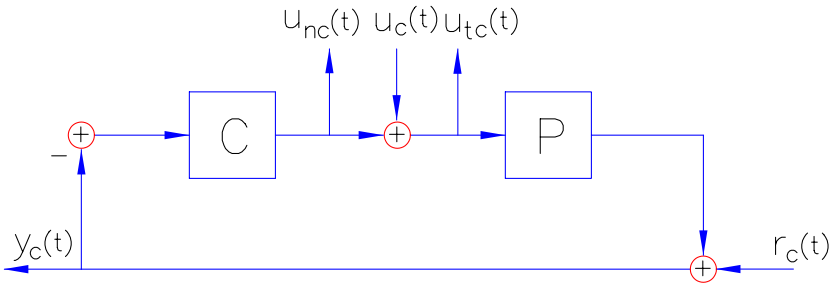

Figure 3-4. *Signals available from Seagate HDD for use in experiments.*

these signals can be measured. The total runout is denoted by $r_c(t)$ and cannot be measured. To measure the various transfer functions in the loop, white noise was injected into the HDD through $u_c(t)$. It had to be of sufficient magnitude to overwhelm the PES caused by the nominal $r_c(t)$. The following transfer functions were measured using this method

$$\begin{aligned} \frac{Y_c(s)}{U_{tc}(s)} &\approx P(s), \\ \frac{U_{nc}(s)}{-Y_c(s)} &\approx K(s), \\ \frac{-U_{nc}(s)}{U_{tc}(s)} &\approx P(s)K(s), \end{aligned} \tag{3-5}$$

and

$$\frac{Y_c(s)}{U_c(s)} \approx \frac{P(s)}{1+P(s)K(s)}. \tag{3-6}$$

This method was used to obtain the experimental data for the figures in Section 2.3 and Section 2.4.

3.2 Interfacing with the Hard Disk Drive

In order to implement the add-on adaptive controller, an interface board had to be developed in order to allow access to PES and send a control signal to the VCM driver. Further, since the PES was available only at discrete intervals, a triggering signal had to be generated in order to synchronize the ADCs of the DSP with the PES.

3.2.1 PES OFFSET

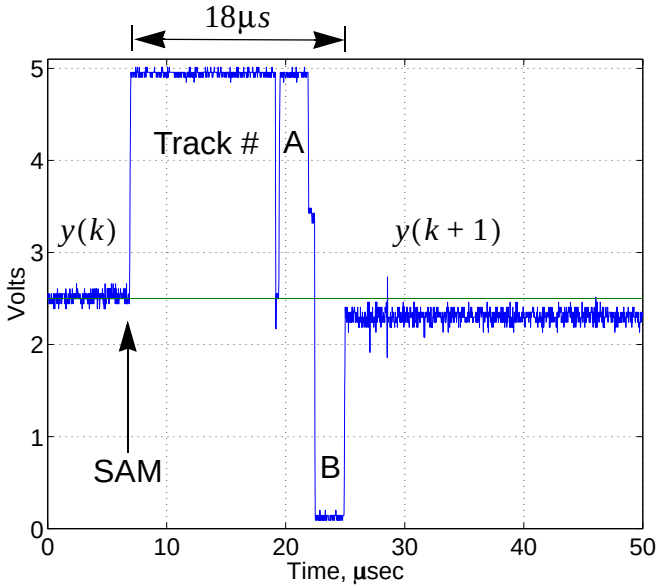

Figure 3-5. *Measured PES directly from HDD. The different features of the servo sector are distinguishable.*

A segment of the PES as read directly from the HDD is displayed in Fig. 3-5. The first section of the signal contains the PES value from the previous servo section $y(k)$ which is held constant until the new servo sector is reached. As stated in Section 2.1.1, the start of each servo sector is marked with a servo address mark. As shown in the Fig. 3-5, the PES transitions to 4.9 V as the R/W head passes over the SAM and the track number. It then transitions from 4.9 V to 0.1 V as the R/W head flies over the A and B bursts. Finally the new value of the PES, $y(k+1)$, is calculated and sent out. The new PES is available approximately 18 μsec after the SAM is reached. This cycle repeats every 250 μsec when a new servo sector is reached. Since the Seagate 2.5" HDD is powered from 5 V supply, the dynamic range of the PES is 0.1 V to 4.9 V, centered about 2.5 V. However, the ADCs of the DSP accepts only ±3 V inputs. To remove the DC bias, the PES is filtered by a passive high pass filter to AC couple the signal. The disadvantage of this method is that DC tracking errors cannot be compensated for by the add-on compensator. However, since the nominal compensator contains integral action, DC tracking errors are already attenuated. Fig. 3-6 shows the circuit used to AC couple the PES. The low frequency pole was placed at 0.4 Hz.

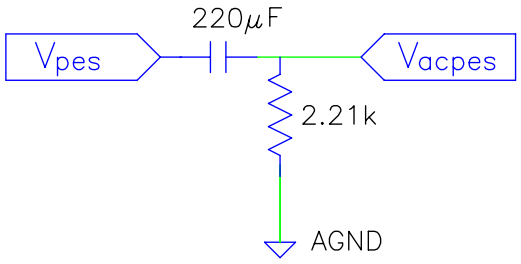

Figure 3-6. *RC filter for AC coupling of the PES.*

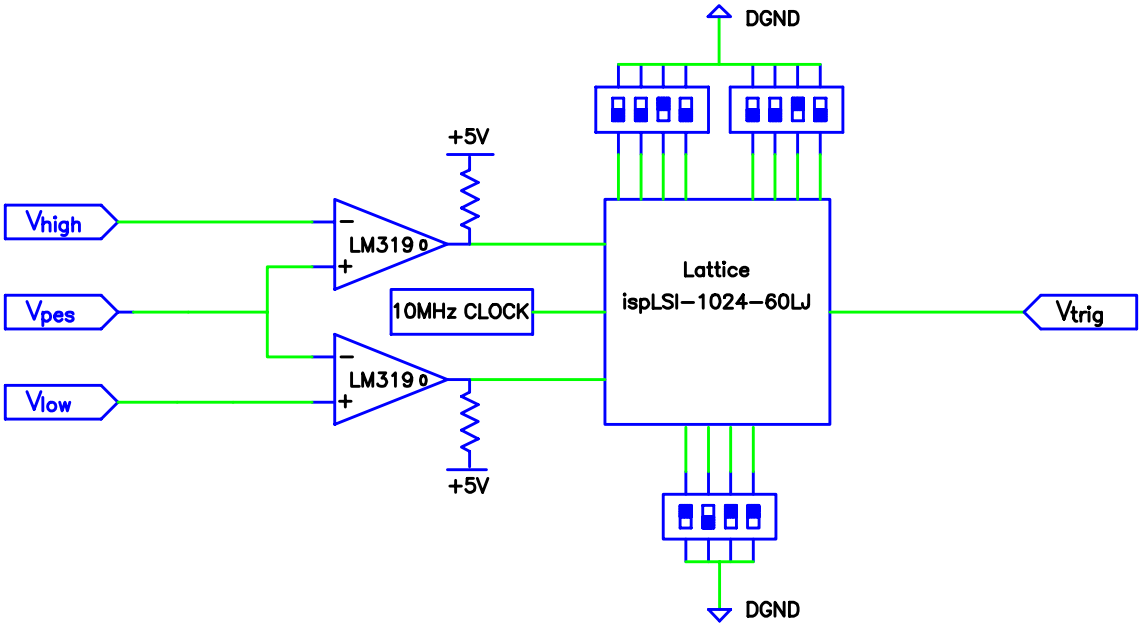

Figure 3-7. *Schematic of circuitry to generate external trigger for the ADCs of the DSP.*

3.2.2 DSP TRIGGER SIGNAL

In order to trigger the ADCs of the DSP with the PES, an external pulse must be generated. For the DSP to read the correct value of the PES, it must be triggered a few mircoseconds after the new PES value is available. Fig. 3-7 shows the circuitry designed to generate the external pulse. It consists of a pair of LM319 comparators, a 10 MHz clock, three 4 pin DIP switches, and an ispLSI-1024-60LJ Lattice chip. The ispLSI-1024-60LJ is an in-system programmable large scale logic device[51]. It allows for a finite state machine to be implemented in digital logic. More detail about the function of this chip will be given in Section 3.2.2. The timing diagram is shown in Fig. 3-8. The comparator's low and high signals are generated when the PES goes below

V_{low} and above V_{high} respectively. V_{low} and V_{high} are set to 4.8 V and 0.2 V. Hence, the transition of the PES from 4.9 V to 0.1 V is captured by the Lattice chip. Using these two inputs, the Lattice chip produces a TTL compatible pulse at the appropriate time to read the PES. After a time delay of *delay 1*, a pulse of width *delay 2* is generated by the Lattice chip. A second pulse of the same width as the first is generated *delay 3* after the first pulse. All these delays are user configurable using the 4 pin DIP switches shown in Fig. 3-7. The reason for the second pulse lies in the way the data is passed from the registers of the ADC and the registers of the 'C40. At the rising edge of the first pulse, the ADC samples the PES and converts the analog signal to a 16 bit digital number stored in the Burr-Brown module's local register. Instead of immediately transferring this data to the 'C40 registers, the Burr-Brown module holds it until the next conversion pulse. Without the second trigger pulse, the 'C40 would receive PES information which was delayed one sampling period. To remove this delay, the second pulse is generated to transfer the sampled PES to the 'C40 resister for use in calculations. Rather than a one sample delay, the delay is now approximately *delay 2* + *delay 3*. The minimum duration of this delay is 5 μsec. This same delay also applies to the DACs. For these experiments, the DACs were triggered from a 200 kHz internal clock which results in a 10 μsec delay.

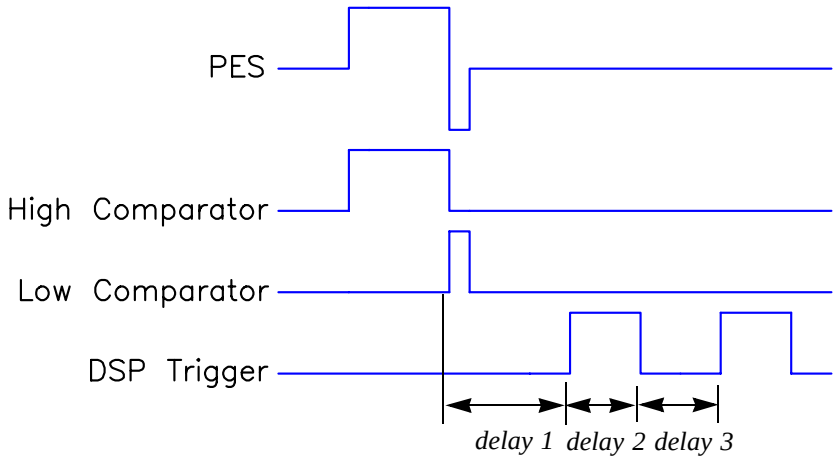

Figure 3-8. *DSP trigger timing diagram with the delays due to the sampling with the 'C40.*

To verify that the above circuit was operating correctly, the AC-coupled PES was sampled and then immediately sent out. These signals along with the trigger were viewed using an oscilloscope and the traces were saved. The comparison of the sampled PES

(from the DSP) and the AC-coupled PES is displayed in Fig. 3-9. The magnitude of the trigger signal was scaled such that it would display in the figure. The sampled PES does not change until 10 μsec after the second triggering pulse because of the two step delay of the DACs. The total delay from the time the new value of PES is available from the HDD to when it is available in the DSP is 20 μsec. There is a bias between the sampled PES and the AC-coupled PES. This bias results from the electrical noise in the circuit. The mean of the difference between these two signals is 0 with a 3σ deviation of 0.14 V. USing the conversion of 3.43 V from volts to tracks, this mean difference is 4% of a track width. Hence, the electrical noise can only cause the sampled PES to be 4% of a track width from the actual PES.

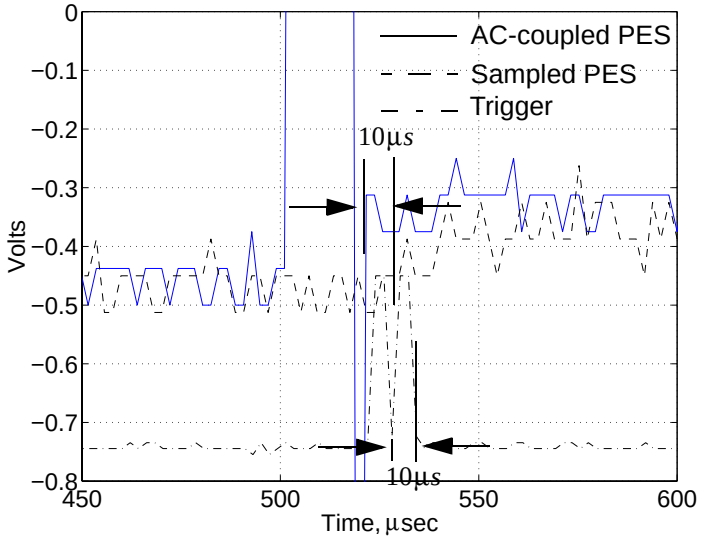

Figure 3-9. *Comparison of sampled PES and AC-coupled PES.*

A ispLSI-1024-60LJ Lattice chip was used to implement the finite state machine that is described by the state transition diagram in Fig. 3-10. There are six states that are needed to generate the trigger signal described in Section 3.2.2. State 0 waits for the high comparator to transition to logical 1 (5 V) which is denoted by the statement 'highc = 1?'. The trigger signal is set to logical 0 (0 V). A counter variable designated as count is set to 0. State 1 waits for the transition of the low comparator to logical 1 with the trigger set to logical 0. Once the transition of the PES signal from 0.1 V to 4.9 V is captured, the system remains in State 2 until the user specified time of *delay 1*. The values of all the

delays are selectable by the 4 pin DIP switches. The delays are 8 bit values inside the Lattice chip with the four least significant bits permanently set to 1. Hence the minimum and maximum delays are 15 and 255 counts respectively with discrete values available in between. Since the Lattice chip is running with a 10 MHz clock, each count represents 100 ns. Hence, delays of 1.5 µs to 25.5 µs are selectable. After *delay 1*, State 2 transitions to State 3 with *count* set to 0. In State 3, *trigger* is set to logical 1, and the transition to State 4 occurs after *delay 2*. State 4 resets *trigger* to logical 0 and waits for time *delay 3* before transitioning in State 5 which generates another pulse. State 5 then transitions to State 0 to wait for the next SAM. Specific details regarding the programming of the Lattice chip is listed in Appendix B2.

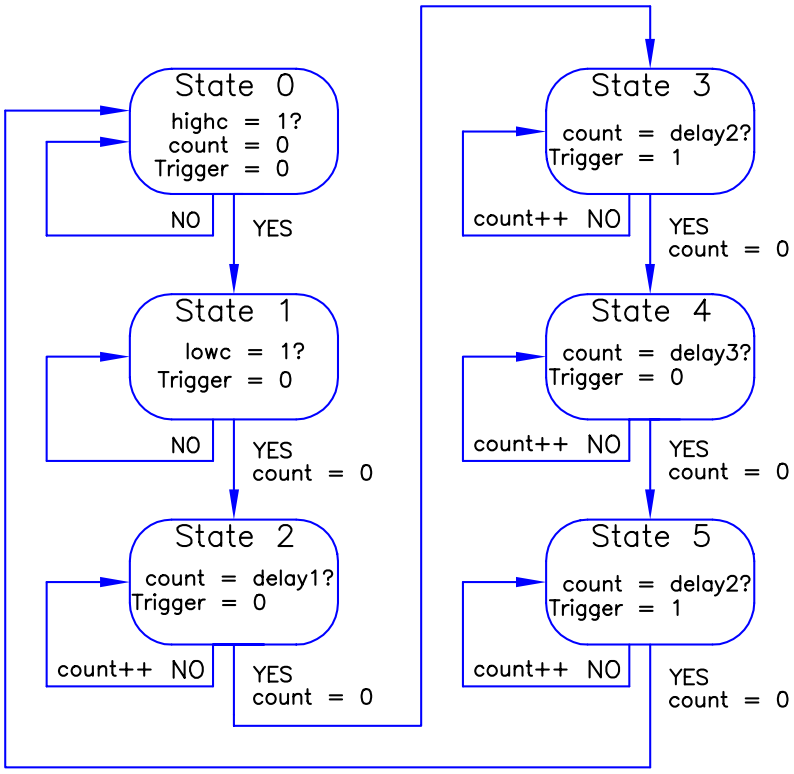

Figure 3-10. *State transition diagram of the program for the programmable logic chip.*

3.2.3 INPUT TO VCM DRIVER

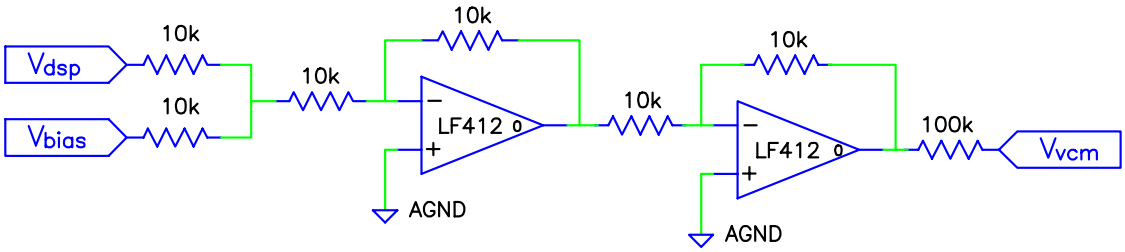

Figure 3-11. *Schematic of output circuitry with summing amplifiers.*

The schematic for the output circuitry is shown in Fig. 3-11. The output circuitry receives the control voltage from the DAC of the DSP, adds the appropriate bias, and scales it to the appropriate level. The input to the VCM driver must be 2.5±0.200 V. The control voltage from the DAC of the DSP is first summed with the bias voltage which is 2.5 V. The combined signal is then passed through an inverting amplifier to correct for the sign inversion from the summer. The result is then sent to the VCM driver of the HDD through a 100 kΩ resistor. Since V_{vcm} is also passed through a summing stage in the PCB of the HDD with a feedback resistance of 16.1 kΩ, the 100 kΩ resistor allows the maximum value of V_{dsp} to be ±1.2 V. The larger output swing from the DAC of the DSP allows for a higher SNR between the calculated value of control and the value sent to the VCM driver.

3.3 SOFTWARE

3.3.1 AT-ATTACHMENT INTERFACE

Standard commands can be sent to the HDD through the ATA interface. The commands are available using interrupt vector 0x13 which is the primary disk interface for the ROM BIOS[43]. A few of the available commands are listed in Table 3-3.

Command	Resistor Value
Reset HDD	0x00
Get Status	0x01
Get HDD Parameter	0x08

Table 3-3. *Brief listing of ATA interface commands for HDD.*

Command	Resistor Value
Initialize HDD Controller	0x09
Seek to Specific Cylinder	0x0c
Recalibrate HDD	0x11
HDD Controller Diagnostic	0x12
HDD Internal Diagnostic	0x14

Table 3-3. *Brief listing of ATA interface commands for HDD.*

These commands must be run with the computer in DOS. These commands will not function properly under Windows™† environment. Listed below is sample code which uses the seek to specified cylinders command.

```
#include<stdio.h>
#include<dos.h>

main(void)
{
   struct REGPACK reg;

// Load CPU registers with the proper data.                    //
// r_ax contains the code which idicated the seek command.     //
// r_cx the upper 8-bits contain the cylinder number.          //
// r_dx selects master or slave drive.                         //

   reg.r_ax = 0x0C00;
   reg.r_cx = 0x0000;
   reg.r_dx = 0x0081;

// Perform command by invoking interrupt13.                    //
   intr(0x13,&reg);
// Print status, 0x00 means successful completion of command.  //
   printf("%d \n",reg.r_ax>>8);
}
```

Modern HDD's have power management features built into their embedded control software. They allow the drive to minimize its power requirements during periods of inactivity. Commonly, the power management features are disabled by default on 3.5" HDD's. The HDD will continue to spin and respond to interface commands immediately no matter how infrequently it is accessed. However, for the Seagate 2.5" HDD used in

†Windows is a trademark of the Microsoft Corporation.

these experiments, the power management features are enabled by default since 2.5” HDD are often used in portable computers where power is limited. After 5 seconds, the HDD enters into an idle mode where the nominal compensator is off and no PES information is available. This feature is detrimental during experiments, so it was disabled. Listed below is the code to disable the power management features. A more detailed description of the commands below can be found in the AT-Attachment interface guide[20].

```
#include<stdio.h>
#include<dos.h>
#include<conio.h>

// Define pointer to store old ISR.                                    //
void interrupt (*oldhandle)(_CPPARGS);

// Define new ISR function which executes old ISR.                     //
void interrupt handle(_CPPARGS)        //
{
   oldhandle();
}

main(void)
{
   unsigned char status;

   disable();                 // Disable all interrupts.
   oldhandle = getvect(0x14); // Get current interrupt vector.
   setvect(0x14,handle);      // Set interrupt vector to handle.
   enable();                  // Enable all interrupts.

   outportb(0x1f0,0x00);      // Disable power management features.
   outportb(0x1f1,0x01);      // Disable power management features.
   outportb(0x1f2,0x55);      // Sector count.
   outportb(0x1f3,0x46);      // Sector number.
   outportb(0x1f4,0x4E);      // Low byte of cylinder number.
   outportb(0x1f5,0x55);      // High byte of cylinder number.
   outportb(0x1f6,0xB0);      // Head number.
   outportb(0x1f7,0xf7);      // Implement command.
   status = inportb(0x1f7);   // Read status of command, 0x50 is
                                 successful completion.
   disable();                 // Disable all interrupts.
   setvect(0x14,oldhandle);   // Set interrupt vector to oldhandle.
   enable();                  // Enable all interrupts.
}
```

3.3.2 DSP SOFTWARE

As stated above, the ADCs were triggered from an external signal synchronized with the PES, and the DACs were triggered from an internal clock running at 200 kHz. The external signal that was used to initiate conversions by the ADCs was also used to cause the DSP to enter an Interrupt Service Routine. It was inside the ISR that the adaptive control output was calculated and the identification algorithms were updated. Listed below is sample code that configures the DSP as stated above. A more complete listing of the DSP program can be found in Appendix B.

```
#include<intpt40.h>        // Realtime interrupt support functions.
#include<carrier.h>        // Pointers to the DSPLINK registers.
#include<stdio.h>

void c_int04(void);        // Function prototype for ISR.

main(void)
{
   volatile unsigned int temp;

// Need to perform an IACK instruction to allow external interrupts //
// through to the ‘C40.                                              //

   asm(“Push AR0”);
   asm(“Push DP”);
   asm(“LDI 030H,AR0”);
   asm(“LSH 16,AR0”);
   asm(“IACK *AR0”);
   asm(“POP DP”);
   asm(“POP AR0”);

   INT_DISABLE();             // Disable all interrupts.

// Set the ISR to be c_int04.  The function c_int04 will contain  //
// the C code to implement the adaptive algorithm.                //
   install_int_vector((void *)c_int04, 0x04);
   load_iif(0x00B0)l          // Set ISR to be level triggered.

   temp = *DM1_RESET;         // Reset Burr Brown board.

// Set ADCs to sample when external trigger occurs and DACs to    //
// trigger off internal clock.                                    //
   *DM1_ROUTE = 0x000E0000;
```

```
    *DM1_AMELIA_CTRL = 0x00A20000;

// Set the ISR to run when ADCs are finished.
    *DM1_INT_MASK = 0x00010000;

// Set the internal clock to 200kHz.
    *DM1_INT_MASK = 0xFFC40000;
    *DM1_CONFIGURATION = 0x8DFF0000;    // Load configuration.
    INT_ENABLE();              // Enable all interrupts.

}
```

4. ACCELEROMETER FEEDFORWARD SERVO

4.1 FORMULATION OF ADAPTIVE CONTROL SCHEME

In this chapter, a SISO discrete time stochastic system will be considered. All transfer functions and signals are expressed in the discrete time domain by using arguments k as the sampling time index and q^{-1} as the unit delay operator. Define $\Im_s$ as the set of all real proper and stable Infinite Impulse Response filters, and $\Im_n$ as the set of all real proper Finite Impulse Response filters of order n.

Referring back to Fig. 2-13 which displays the overall block diagram of the HDD in track following mode, the PES can be characterized by the following dynamic model

$$y(k) = \frac{P(q^{-1})}{1 + P(q^{-1})K(q^{-1})}u(k) + \frac{1}{1 + P(q^{-1})K(q^{-1})}r(k)\,, \tag{4-1}$$

where $u(k)$ is the auxiliary control input and $r(k)$ is the runout generated by external disturbances.

As stated earlier, external disturbances can cause a significant amount of runout in current HDD's. The scheme presented here uses an accelerometer signal to obtain an estimate of the disturbance. Since the accelerometer provides a measurement of the disturbance before the disturbance is delayed by the time constant of the HDD and before the disturbance effects the position of the R/W head, the accelerometer measurement can be used as a preview of the track runout to be caused by the external disturbance. The accelerometer is typically mounted on the base casting of the HDD. The control signal, $u(k)$, is described by the following relation

$$u(k) = Q(q^{-1})a(k)\,, \tag{4-2}$$

where $Q(q^{-1})$ is the feedforward compensator dynamics which in this case will be realized by a Finite Impulse Response filter, and $a(k)$ is the accelerometer signal. Expanding the block diagram given in Fig. 2-13 to include the control scheme given above and the generation of $r(k)$ from external disturbances yields the block diagram

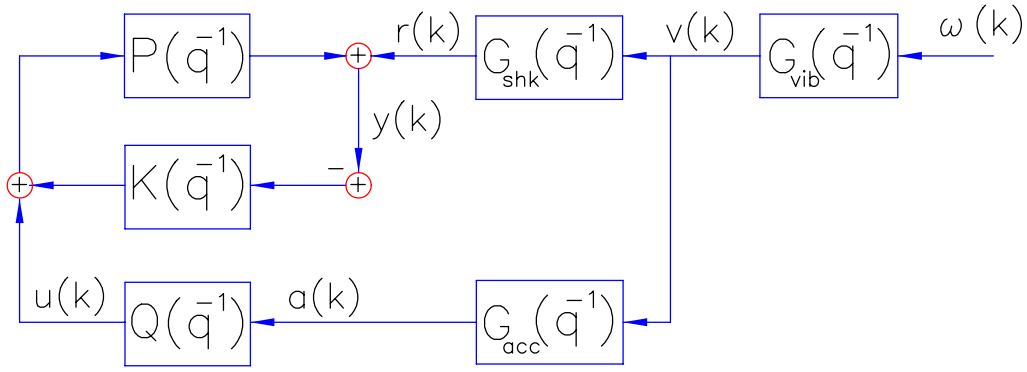

Figure 4-1. *Block diagram of HDD system including external disturbance model and auxiliary controller.*

given in Fig. 4-1. The mechanical dynamics which convert the external disturbance, $v(k)$, to runout, $r(k)$ are represented by $G_{shk}(q^{-1})$. The white noise random process, $\omega(k)$, is shaped by $G_{vib}(q^{-1})$ to match the spectral content of a desired external disturbance. The dynamics of the accelerometer which generates the accelerometer signal, $a(k)$, from $v(k)$ are depicted by $G_{acc}(q^{-1})$. Using this block diagram, Eq. (4-1) can be rewritten as

$$y(k) = \frac{P(q^{-1})}{1 + P(q^{-1})K(q^{-1})}u(k) + \frac{G_{shk}(q^{-1})G_{vib}(q^{-1})}{1 + P(q^{-1})K(q^{-1})}\omega(k), \tag{4-3}$$

which can in turn be rewritten in an ARMAX model as

$$y(k) = \frac{B_d(q^{-1})}{A_d(q^{-1})}u(k) + \frac{C(q^{-1})}{A_d(q^{-1})A_v(q^{-1})}\omega(k), \tag{4-4}$$

where

$$\begin{aligned} A_d(q^{-1}) &= 1 + a_{d1}q^{-1} + \ldots + a_{dn_{A_d}}q^{-n_{A_d}}, \\ B_d(q^{-1}) &= b_{d0} + b_{d1}q^{-1} + \ldots + b_{dn_{B_d}}q^{-n_{B_d}}, \\ C(q^{-1}) &= 1 + c_1q^{-1} + \ldots + c_{n_C}q^{-n_C}, \\ A_v(q^{-1}) &= 1 + a_{v1}q^{-1} + \ldots + a_{vn_{A_v}}q^{-n_{A_v}}. \end{aligned} \tag{4-5}$$

The poles of the disturbance and spectral coloring transfer functions are contained in

$A_v(q^{-1})$, while the poles of the HDD system are contained in $A_d(q^{-1})$. The following equation can be obtained by manipulating Eq. (4-4)

$$y(k) = \frac{B(q^{-1})}{A(q^{-1})}u(k) + \frac{C(q^{-1})}{A(q^{-1})}\omega(k), \tag{4-6}$$

where

$$\begin{aligned} A(q^{-1}) &= 1 + a_1 q^{-1} + \ldots + a_{n_A} q^{-n_A}, \\ B(q^{-1}) &= b_0 + b_1 q^{-1} + \ldots + b_{n_{B_d}} q^{-n_B}, \\ C(q^{-1}) &= 1 + c_1 q^{-1} + \ldots + c_{n_C} q^{-n_C}. \end{aligned} \tag{4-7}$$

The accelerometer signal is given by

$$a(k) = G_{acc}(q^{-1})G_{vib}(q^{-1})\omega(k), \tag{4-8}$$

which can be written in an ARX model as

$$a(k) = \frac{B_{acc}(q^{-1})}{A_{acc}(q^{-1})}\omega(k), \tag{4-9}$$

where

$$\begin{aligned} A_{acc}(q^{-1}) &= 1 + acc_1 q^{-1} + \ldots + acc_{n_{Acc}} q^{-n_{Acc}}, \\ B_{acc}(q^{-1}) &= 1 + bcc_1 q^{-1} + \ldots + bcc_{n_{Bcc}} q^{-n_{Bcc}}. \end{aligned} \tag{4-10}$$

Substituting Eq. (4-9) into Eq. (4-6), the following relation is obtained

$$y(k) = \frac{B(q^{-1})B_{acc}(q^{-1})Q(q^{-1}) + C(q^{-1})A_{acc}(q^{-1})}{A(q^{-1})A_{acc}(q^{-1})}\omega(k). \tag{4-11}$$

Since $y(k)$ is the PES and it is desired to keep the 3σ value less than an eighth of a track width[23], the control objective is to find the optimal filter $Q^{\circ}(q^{-1})$ which

minimizes the following cost function

$$Q^{o}(q^{-1}) = \arg\left\{ \min_{Q \in \Im_s} E\{|y(k)|^2\} \right\}, \tag{4-12}$$

$$= \arg\left\{ \min_{Q \in \Im_s} \left\| \frac{B(q^{-1})B_{acc}(q^{-1})Q(q^{-1}) + C(q^{-1})A_{acc}(q^{-1})}{A(q^{-1})A_{acc}(q^{-1})} \omega(k) \right\|_2 \right\}, \tag{4-13}$$

where the variance of the PES is

$$E\{|y(k)|^2\} = \lim_{N \to \infty} \frac{1}{N} \sum_{k=0}^{N} |y(k)|^2 \ , \tag{4-14}$$

and E is the expectation operator.

The solution to Eq. (4-13) can be obtained from Wiener filtering theory. A large class of linear discrete time optimization problems can be collectively solved by Wiener filtering[33]. One particular class of problems involves designing a linear discrete time filter whose output provides an estimate of a desired signal. The goal in designing such filters is minimizing the mean squared deviation of the output of the filter and desired signal. The solution to this class of problems will be discussed here.

The basic block diagram for Wiener filtering is shown in Fig. 4-2. The input to the filter $Q(q^{-1})$ is $x(k)$. The output of the filter, $p(k)$, is an estimate of $d(k)$, the desired signal; and $y(k)$ is the estimation error defined by as $d(k) - p(k)$. The objective of Wiener filtering is to design $Q(q^{-1})$ such that the mean square value of the estimation error is minimized. This objective is equivalent to the cost function given in Eq. (4-12).

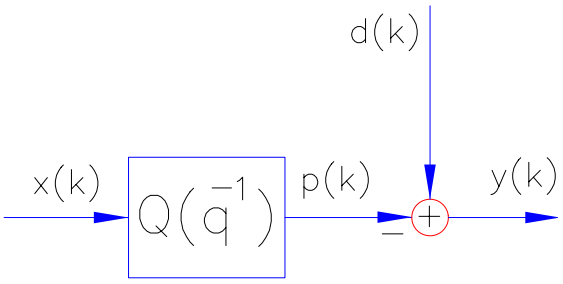

Figure 4-2. *Basic block diagram for Wiener filtering.*

To derive the solution to Eq. (4-12), it is assumed that the filter input and the desired signal are both zero mean, jointly wide sense stationary stochastic processes. Further, a FIR representation of the optimal filter will be used instead of an IIR filter. An FIR filter is inherently stable which is an advantage over an IIR filter in adaptive schemes. In adaptive IIR filter schemes, the stability of the filter must always be checked. An adaptive FIR filter need only to have the value of its coefficients to be constrained for the filter to have guaranteed stability. The disadvantage is that a large-order FIR filter is often needed to match the performance give by lower-order IIR filters. Hence adaptive schemes using FIR filters tend to be more computationally demanding than schemes using IIR filters. However, since the stability of the servos of HDD's is of paramount importance, a FIR scheme was pursued despite the additional computational burden.

Under these assumptions, the derivation for the optimal FIR filter proceeds as follows. Define the cost function as the variance of the PES

$$J = E\{|y(k)|^2\}, \tag{4-15}$$

where from Fig. 4-2, $y(k)$ may be written as

$$y(k) = d(k) - \sum_{i=0}^{n_Q} Q_i(q^{-1})x(k-i), \tag{4-16}$$

and $Q_i(q^{-1}) = h_i q^{-i}$ where the polynomial $Q(q^{-1})$ is given by

$$Q(q^{-1}) = h_0 + h_1 q^{-1} + \ldots + h_{n_Q} q^{-n_Q}, \tag{4-17}$$

and n_Q is the order of the FIR filter.

The minimum value of Eq. (4-15) can be found by taking the partial derivative of J with respect to the individual taps of $Q(q^{-1})$ and equating the result to zero. Hence

$$\frac{\partial J}{\partial Q_i(q^{-1})} = -2E\left\{\left(d(k) - \sum_{j=0}^{n_Q} Q_j(q^{-1})x(k-j)\right)x(k-i)\right\}. \tag{4-18}$$

Defining $ac(i-j) = E\{x(k-j)x(k-i)\}$ and $cc(i) = E\{d(k)x(k-i)\}$ as the

autocorrelation of $x(k)$ and the cross correlation between $x(k)$ and $d(k)$, respectively, and equating Eq. (4-18) to zero, an expression for the optimal FIR filter can be obtained

$$\sum_{i=0}^{n_Q} Q_j^o(q^{-1})ac(i-j) = cc(i), \qquad 0 \le i \le n_Q . \tag{4-19}$$

The set of equations given by Eq. (4-19) are known as the Wiener-Hopf equations. It provides the solution to the optimization problem posed in Eq. (4-12) and Eq. (4-15). Rewriting Eq. (4-19) in vector notation

$$RH^o = CC \tag{4-20}$$

where $H^o = [h_1^o \; h_2^o \ldots h_{n_Q}^o]^T$, $CC = [cc(0) \; cc(1) \ldots cc(n_Q)]^T$, and

$$R = \begin{bmatrix} ac(0) & ac(1) & \cdots & ac(n_Q) \\ ac(1) & ac(0) & \cdots & ac(n_Q-1) \\ \vdots & \vdots & \ddots & \vdots \\ ac(n_Q) & ac(n_Q-1) & \cdots & ac(0) \end{bmatrix}.$$

Assuming that R is non-singular, the solution to the optimal FIR filter is

$$H^o = R^{-1}C . \tag{4-21}$$

4.2 APPLICATION OF WIENER FILTERING

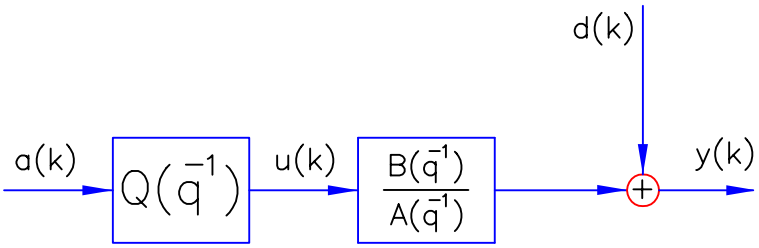

Figure 4-3. *Block diagram accelerometer feedforward before swapping.*

Rewriting Eq. (4-2) and Eq. (4-6) in a form similiar to the Wiener filtering form given

in Eq. (4-16) yields

$$y(k) = \frac{B(q^{-1})}{A(q^{-1})}Q(q^{-1})a(k) + d(k) \tag{4-22}$$

where $d(k)$ is defined as $(C(q^{-1})/A(q^{-1}))\omega(k)$. The block diagram of the system represented by Eq. (4-22) is shown in Fig. 4-3. Assuming that the conditions given in Section 4.1 hold, $Q(q^{-1})$ and $B(q^{-1})/A(q^{-1})$ can be exchanged. The resulting block diagram of that system is shown in Fig. 4-4.

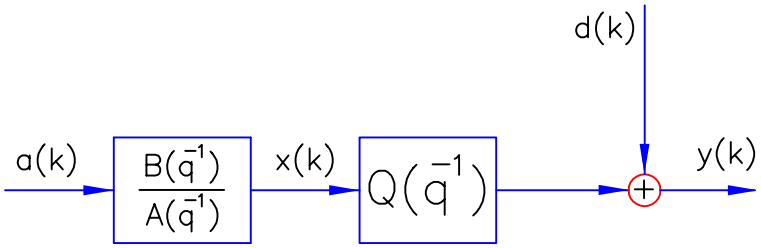

Figure 4-4. *Block diagram accelerometer feedforward after swapping.*

The system is in the form of the Wiener filtering problem given in Section 4.1. However, in the previous problem, $x(k)$ and $d(k)$ were assumed to be known. In general, the only three signals available for processing in HDD's are $a(k)$, $u(k)$, and $y(k)$. Assume for the moment that the polynomials $A(q^{-1})$ and $B(q^{-1})$ are known. Then $x(k)$ can be generated by filtering $a(k)$ by the following relation

$$x(k) = \frac{B(q^{-1})}{A(q^{-1})}a(k). \tag{4-23}$$

Further, since $y(k)$ is measured and $u(k)$ is generated, $d(k)$ can be calculated by the following relationship

$$d(k) = y(k) - \frac{B(q^{-1})}{A(q^{-1})}u(k). \tag{4-24}$$

In what follows, the adaptation scheme is discussed when the stochastic disturbance, $d(k)$, is not measurable and the plant polynomials, $A(q^{-1})$ and $B(q^{-1})$, are unknown. This scheme consists of two Parameter Adaptation Algorithms running simultaneously. The first PAA identifies the plant and noise model polynomials and produces an estimate

of the stochastic disturbance. The second PAA is an adaptive Wiener filtering algorithm that identifies the optimal FIR filter $Q^o(q^{-1})$ which is the solution of Eq. (4-12).

4.3 PARAMETER ADAPTATION ALGORITHM

Before the two parameter adaptation algorithm are discussed, the system assumptions will be given in a more rigorous sense. Rewritten here for convenience is Eq. (4-22)

$$y(k) = \frac{B(q^{-1})}{A(q^{-1})}u(k) + d(k),$$

where $y(k)$, is the output of the system, $u(k)$ is the auxiliary control input, and $d(k)$ is a stochastic disturbance given by

$$d(k) = \frac{C(q^{-1})}{A(q^{-1})}\omega(k), \tag{4-25}$$

where $\omega(k)$ is a white noise random disturbance with finite moments.

The following assumptions are made about the system:

a.) An upper bound for n_A, n_B, and n_C is known.

b.) $A^*(q) = q^{n_A}A(q^{-1})$ and $C^*(q) = q^{n_C}C(q^{-1})$ are Hurwitz.

c.) $C(z^{-1})$ is strictly input passive.

d.) The zero delay term in $B(q^{-1})$, b_o, is known.

Notice that no minimum phase assumptions are placed upon $B(q^{-1})$.

4.3.1 PLANT IDENTIFICATION PAA

The plant identification PAA identifies the unknown plant and noise model polynomials and obtains an estimate of the stochastic disturbance $d(k)$, which will be denoted by $\hat{d}(k)$. A Stochastic Gradient Algorithm[27] is used for parameter identification.

4.3. Parameter Adaptation Algorithm

Using standard system identification notation, the system output can be rewritten as

$$y(k) = \psi(k)^T\theta + \omega(k), \tag{4-26}$$

where

$$\theta = [a_1 \ldots a_{n_A}\ b_1 \ldots b_{n_B}\ c_{1\ldots}c_{n_c}]^T, \tag{4-27}$$

and

$$\psi(k) = [-y(k-1)\ldots -y(k-n_A)\ u(k-1)\ldots u(k-n_B)\ \omega(k-1)\ldots\omega(k-n_C)]^T. \tag{4-28}$$

The parameter estimate and regressor vectors are subsequently defined as

$$\hat{\theta}(k) = [\hat{a}_1(k)\ldots\hat{a}_{\hat{n}_A}(k)\ \hat{b}_1(k)\ldots\hat{b}_{\hat{n}_B}(k)\ \hat{c}_1(k)\ldots\hat{c}_{\hat{n}_C}(k)]^T, \tag{4-29}$$

and

$$\phi(k-1) = [-y(k-1)\ldots -y(k-\hat{n}_A)\ u(k-1)\ldots u(k-\hat{n}_B)\ \hat{e}_\theta(k-1)\ldots\hat{e}_\theta(k-\hat{n}_C)]^T, \tag{4-30}$$

where $\hat{e}_\theta(k)$ is the a-priori estimation error which is defined below. The SGA can then be written as

$$\begin{aligned} \hat{\theta}(k) &= \hat{\theta}(k-1) + \frac{\beta_\theta}{F_\theta(k-1)}\phi(k-1)\hat{e}_\theta(k), \\ F_\theta(k-1) &= F_\theta(k-2) + \lambda_\theta\phi^T(k-1)\phi(k-1), \\ \hat{e}_\theta(k) &= y(k) - \phi^T(k-1)\hat{\theta}(k-1), \end{aligned} \tag{4-31}$$

where $0 < \lambda_\theta \le 1$ and $\beta_\theta > 0$.

The estimated stochastic disturbance $\hat{d}(k)$ can now be obtained by

$$\hat{d}(k) = y(k) - \hat{y}_d(k), \tag{4-32}$$

where

$$\hat{y}_d(k) = -\ddot{A}(k, q^{-1})y(k) + \ddot{B}(k, q^{-1})u(k)\,, \tag{4-33}$$

and

$$\begin{aligned}\hat{A}(k, q^{-1}) &= 1 + \hat{a}_1(k)q^{-1} + \ldots + \hat{a}_{\hat{n}_A}(k)q^{-\hat{n}_A},\\ \hat{B}(k, q^{-1}) &= 1 + \hat{b}_1(k)q^{-1} + \ldots + \hat{b}_{\hat{n}_B}(k)q^{-\hat{n}_B}.\end{aligned} \tag{4-34}$$

4.3.2 FIR FILTER PAA

In order to obtain estimates of the optimal FIR filter, the following signal needs to be calculated using the plant polynomials obtained from the plant identification PAA

$$\ddot{A}(k, q^{-1})\hat{x}(k) = -\ddot{B}(k, q^{-1})a(k)\,. \tag{4-35}$$

The parameter and regressor vectors for the FIR filter PAA are

$$\begin{aligned}\hat{H} &= [\hat{h}_1\ \hat{h}_2 \ldots \hat{h}_{\hat{n}_Q}]^T,\\ \hat{X}(k) &= [\hat{x}(k)\ \hat{x}(k-1)\ldots\hat{x}(k-\hat{n}_Q)]^T,\end{aligned} \tag{4-36}$$

where $\ddot{H}$ is of order $\hat{n}_Q$. The adaptation for $\ddot{H}(k)$ uses the SGA

$$\begin{aligned}\hat{H}(k) &= \hat{H}(k-1) + \frac{\beta_Q}{F_Q(k)}\hat{X}(k-1)\hat{e}_Q(k),\\ F_Q(k) &= F_Q(k-1) + \lambda_Q\hat{X}^T(k-1)\hat{X}(k-1),\\ \hat{e}_Q(k) &= \hat{d}(k) - X^T(k-1)\hat{H}(k-1),\end{aligned} \tag{4-37}$$

where $0 < \lambda_Q \le 1$ and $\beta_Q > 0$. Finally, the adaptive control law is

$$u(k) = \ddot{Q}(k-1, q^{-1})a(k)\,. \tag{4-38}$$

The overall block diagram of the adaptive scheme including the two PAAs is shown in Fig. 4-5. The combination of the accelerometer dynamics and the spectral coloring filter is represented by $G_{acv}(q^{-1})$. The QPAA describes the algorithm given by Eqs. (4-35) through (4-37) which estimates the optimal FIR filter. The PPAA describes the algorithm

given by Eqs. (4-29) through (4-31) which estimates the plant parameters.

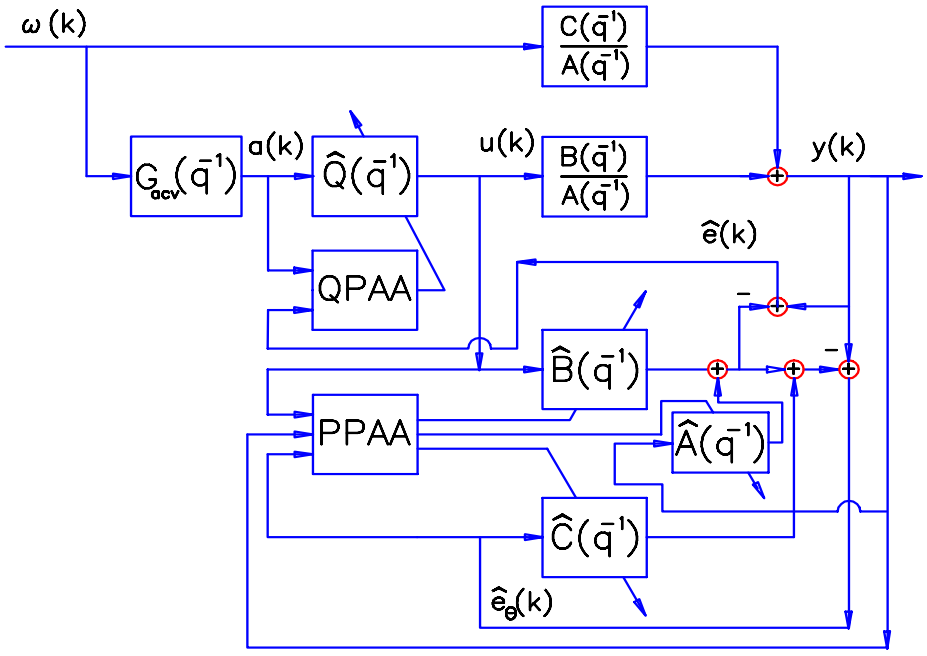

Figure 4-5. *Block diagram of adaptive accelerometer scheme.*

4.4 THEORETICAL RESULTS

The stability of the overall adaptive system was analyzed using stochastic Lyapunov functions and the Martingale convergence theorem as in [27]. The convergence and self-optimizing properties of the algorithm were analyzed using the ODE approach. The theoretical development and validation can be found in [34]. The major results are summarized below.

Theorem 1. Consider the ARMAX representation of the regulated variable closed loop dynamics given by Eq. (4-6), with the auxiliary control action given by Eq. (4-2). Under the assumptions: a) $\omega(k)$ *is a zero mean innovation signal with bounded covariance; b) the transfer function* $C(z)$ *is strictly input passive; c)* $\hat{n}_A \geq n_A$, $\hat{n}_B \geq n_B$, and $\hat{n}_C \geq n_C$ *; d) the FIR filter parameter vector* $\hat{H}(k)$ *satisfies* $\left|\hat{H}(k)\right| \leq h_{max} < \infty$ *; then the Pseudo Linear Regression (PLR) algorithm given by Eqs. (4-29) through (4-31) has the following*

properties:

$$\lim_{N\to\infty} \frac{1}{N}\sum_{k=1}^{N} [\hat{e}_\theta(k) - \omega(k)]^2 = 0, \tag{4-39}$$

$$\lim_{N\to\infty} \sum_{k=1}^{N} [\hat{\theta}(k) - \hat{\theta}(k-m)]^2 < \infty, \quad \forall m < \infty, \tag{4-40}$$

$$\lim_{N\to\infty} \frac{1}{N}\sum_{k=1}^{N} E_k[y(k) - \hat{y}(k)]^2 = 0, \tag{4-41}$$

$$\lim_{N\to\infty} \frac{1}{N} F_\theta(N-1) \le \infty, \text{ a.s.} \tag{4-42}$$

where E_k denotes the expectation operator with the terms up to and including $k-1$ are assumed to be known.

Loosely speaking, the above theorem indicates that the PLR algorithm asymptotically converges to a whitening filter (i.e. $\hat{e}_\theta(k)$ to $\omega(k)$). Moreover, the signals $y(k)$, $u(k)$ and $\hat{e}_\theta(k)$ are mean square bounded and the parameter estimate difference converges. The proof of Theorem 1 is given in Appendix A1.

Theorem 2. Consider the adaptive system described in Theorem 1 when the PAA algorithm given by Eqs. (4-36) through (4-37) is utilized and the signals $\hat{d}(k)$ and $\ddot{x}(k)$ are generated by Eq. (4-32) and Eq. (4-35), respectively. Under the additional conditions that a projection algorithm is utilized so that the polynomial $q^{\hat{n}_A}\hat{A}(k, q^{-1})$ is always Hurwitz then

1. *The parameter vector $[\hat{\theta}(k)\ \ddot{H}(k)]$ of the adaptive control algorithm converges with probability 1 to an equilibrium point $[\bar{\theta}\ H]$.*
2. *If $\hat{\theta} \to \{\theta: \bar{B}/\bar{A} = B/A\}$ then $\ddot{H} \to H = H^\circ$, where H° is the optimal Wiener filter parameter vector.*
3. *If $\hat{\theta} \to \theta$, then $\hat{H} \to H^o$, where H° is the optimal Wiener filter parameter vector.*

4. *If* $[\theta\ H] \rightarrow [\theta\ H]$ *such that* $A_{acc}C(q^{-1}) + B_{acc}B(q^{-1})Q(q^{-1})$ *and* $A(q^{-1})$ *are coprime and* $A_{acc} + B_{acc}Q(q^{-1})$ *and* A_{acc} *are co-prime with* $n_Q \geq \hat{n}_A$, *then* $[\bar{\theta}\ H] \rightarrow [\theta\ H^\circ]$.

5. *If* $B/A = B/A$, *then* $[\theta\ H^\circ]$ *is locally stable equilibrium points of the adaptive system. Moreover,* $1/C(z)$ *is SPR.*

6. *If* $\hat{\theta} \rightarrow \{\bar{\theta}: \bar{B}^- = B^-\}$, *then* $\lim_{n_Q \rightarrow \infty} Q = Q^\circ$ *where* $\bar{B}^-$ *and* B^- *contain all the roots of* B *and* B, *respectively, which are outside the unit circle.*

7. $B = 0$ *and* $Q = 0$ *is always an unstable equilibrium point of the closed loop adaptive system.*

Although the above theorem shows that the optimal minimum variance regulator is always an equilibrium point of the closed loop adaptive system, it has not been shown to be the only equilibrium point. Fortunately, the fourth result in the theorem provides a method to verify that the adaptive system has indeed converged to the true minimum variance regulator, and the plant parameter estimates have converged to the true parameters. The proof of Theorem 2 is given in Appendix A2.

The self-tuning properties of the adaptive control scheme are assured with the introduction of an additional exogenous input. Instead of using Eq. (4-38), the control input will now be given by

$$u(k) = \dot{Q}(k-1, q^{-1})a(k) + \eta(k), \tag{4-43}$$

where $\eta(k)$ is an exogenous input which satisfies the properties outlined in the following theorem.

Theorem 3. Consider the adaptive system described in Theorem 2, with the control input given by Eq. (4-43) instead of Eq. (4-38). If the exogenous input $\eta(k)$ *satisfies the following properties: a)* $\eta(k)$ *is an ergodic stochastic process with finite moments and is independent of* $\omega(k)$ *and b)* $\eta(k)$ *is persistently exciting of order greater than* $n_B + 1$, *then the closed loop adaptive system is always self-tuning. Moreover, the stationary*

polynomials $A(q^{-1})$, $B(q^{-1})$ *and* $Q(q^{-1})$ *calculated from the stable equilibrium vector* $[\bar{\theta}\ H]$ *satisfy:*

1. $B/A = B/A$

2. $\bar{Q} = Q^o$

3. Furthermore, if $\hat{n}_A = n_A$, $\hat{n}_B = n_B$ *and* $\hat{n}_C = n_C$, *then* $\bar{\theta} = \theta$.

The proof of Theorem 2 is given in [56].

Remarks:

The diminishing excitation technique presented in [10] is a good selection for the exogenous input $\eta(k)$. For the SGA algorithm presented in Section 4.3, $\eta(k)$ can be chosen as

$$\eta(k) = \frac{\varepsilon(k)}{k^{\delta/2}}, \tag{4-44}$$

where $\varepsilon(k)$ is a random sequence independent of $\omega(k)$ with zero mean and unit variance and

$$\delta \in \left(0, \frac{1}{2(t+1)}\right], \tag{4-45}$$

where

$$t = max(n_A, n_B, n_C) + n_A - 1\,. \tag{4-46}$$

Then $\eta(k)$ satisfies the conditions in Theorem 3 and therefore, it can be used as an excitation signal to guarantee consistency of the parameter estimation. Notice however that this signal asymptotically converges to zero and, as a consequence, it has no effect on the asymptotic performance of the closed loop system. It has been proven in Theorem 2 that the exact plant parameter and optimal Wiener filter parameter is a locally stable equilibrium point of the two PAAs, without any exogenous excitation signal. Therefore, once the adaptive system converges to its true parameters, due to the use of the exogenous excitation signal $\eta(k)$, it will never escape from this equilibrium point, even after the

excitation signal disappears.

4.5 SIMULATIONS

4.5.1 FULL ORDER SIMULATIONS

In the interest of clarity, the simulation results presented here are for a simple system described by Eq. (4-6) where

$$\begin{aligned} A(q^{-1}) &= 1 + 0.25q^{-1} - 0.125q^{-2}, \\ B(q^{-1}) &= 1.0q^{-1} + 0.75q^{-2}, \\ C(q^{-1}) &= 1 - 0.9q^{-1}. \end{aligned} \tag{4-47}$$

The orders of the plant polynomials $A(q^{-1})$, $B(q^{-1})$, and $C(q^{-1})$ were assumed to be known; and hence a full order estimation was done. Further, the accelerometer was assumed to measure $\omega(k)$ through a low-pass filter which characterizes the accelerometer dynamics. These dynamics are described by the following equation

$$\begin{aligned} A_{acc}(q^{-1}) &= 1 - 0.1202q^{-1}, \\ B_{acc}(q^{-1}) &= 0.4399(1 + q^{-1}). \end{aligned} \tag{4-48}$$

A fourth order FIR filter was used for the compensator. The optimal compensator as well as the optimal PES variance were computed by solving a Lyapunov equation. Both PAA algorithms were run simultaneously without the use of an additional excitation signal.

The convergence of the plant parameters is displayed in Fig. 4-6. After approximately 1000 samples, the parameter values are within 10% of their expected values. Hence, by Theorem 2, result 3, since $\hat{\theta}$ converges to θ, then $\ddot{H}$ must converge to the optimal solution, H°. The convergence rate can be increased by decreasing the initial value of $F_{\theta}(k)$.

The convergence of the compensator parameters is shown in Fig. 4-7. The parameters converge to their respective values as expected. After approximately 1000 samples, these

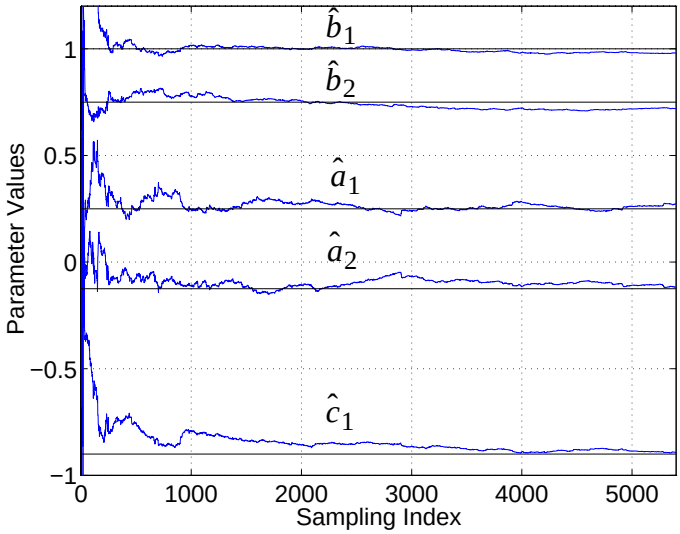

Figure 4-6. *Convergence of plant parameters.*

parameter values are also within 10% of their expected values. The convergence rate can be increased by decreasing the initial value of $F_Q(k)$. The expected value of improvement in the variance agreed with the simulated value which was 19.3%. The improvement is calculated as the difference in the variance of the PES between the nominal and adaptive cases, divided by the variance of the nominal controller.

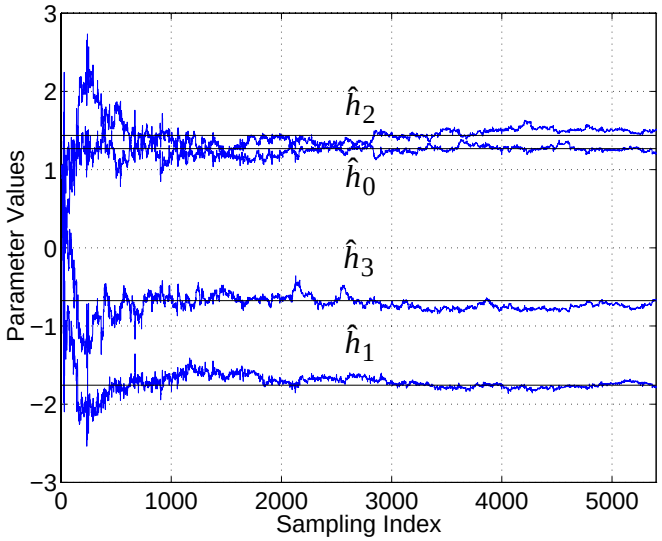

Figure 4-7. *Convergence of controller parameters.*

Result 4 from Theorem 2 also gives a way to verify that the adaptive system has converged to the true minimum variance regulator and plant parameter estimates if the the true parameter values were not available *a-priori*. The roots of the polynomials are

displayed in Eq. (4-49). Both pairs of polynomials are co-prime which indicates that the adaptive system has indeed converged to the true minimum variance regulator and plant parameter estimates.

$$\begin{aligned} A_{acc}\bar{C}(q^{-1}) + B_{acc}\bar{B}(q^{-1})\bar{Q}(q^{-1}) &= (1 - 0.5488q^{-1})(1 + 0.8195q^{-1}) \\ &\quad (1 + (0.4691 \pm 0.67i)q^{-1})(1 - (0.3732 \pm 0.7757i)q \\ \bar{A} &= (1 - 0.5q^{-1})(1 + 0.25q^{-1}) \\ B_{acc}\bar{Q} &= 0.4399(1 + q^{-1})(1 + 8.009q^{-1})(1 + (0.2921 \pm 0.7615i)q^{-1}) \\ A_{acc} &= (1 - 0.1202q^{-1}) \end{aligned} \tag{4-49}$$

The computational complexity of the algorithm is directly proportional to the order of the plant and the controller estimation. The plant identification algorithm requires $3(\hat{n} + 1)$ multiplications and $3\hat{n} + 2$ additions where $\hat{n} = \hat{n}_A + \hat{n}_B + \hat{n}_C$ is the combined order of estimated plant. Generation of the estimate of the stochastic disturbance and the regressor for the optimal FIR filter algorithm both require $\hat{n}_A + \hat{n}_B$ multiplications and additions. The optimal FIR filter algorithm requires $3(\hat{n}_Q + 2)$ multiplications and $3\hat{n}_Q + 5$ additions. Finally, generation of the control signal requires $\hat{n}_Q + 1$ multiplications and $\hat{n}_Q$ additions. Therefore, one full cycle of computation requires $3(\hat{n} + 1) + 2(\hat{n}_A + \hat{n}_B) + 4\hat{n}_Q + 7$ multiplications and $3(\hat{n} + 1) + 2(\hat{n}_A + \hat{n}_B) + 4\hat{n}_Q + 4$ additions which is approximately $5\hat{n} + 4\hat{n}_Q$ multiplications and additions. As will be described in Section 5.2.1, $\hat{n} = 7$ and $\hat{n}_Q = 5$ were found to be sufficient to model the typical HDD and optimal FIR filter. Hence, one full cycle of computation will require 55 multiplications and additions.

4.5.2 SIMULATIONS USING HDD MODELS

As mentioned in Section 2.2.2.4, external disturbances which rotate the base casting of the HDD about the center of rotation of the arm cause large tracking errors. Since the bearing friction is rather small, the actuator is effectively decoupled from the base casting of the HDD, and therefore the arm actuator will not follow the rotation of the base casting. Hence, a rotation disturbance which causes the base casting of the HDD to rotate about the

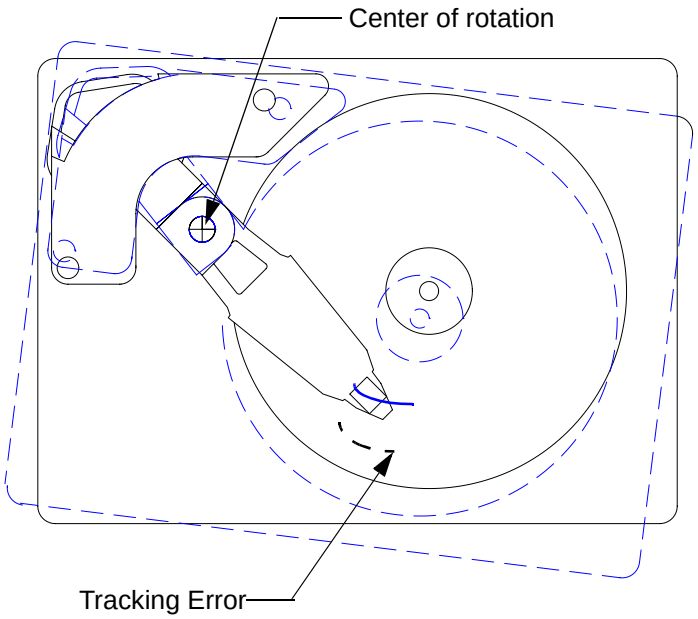

Figure 4-8. *Rigid-body effect of rotational disturbances on HDD's.*

center of rotation of the actuator will cause a large tracking error as depicted in Fig. 4-8. Moreover, as described in Section 2.2, mechanical resonance modes from the spindle motor, suspension, and actuator bearings will also contribute to the tracking error.

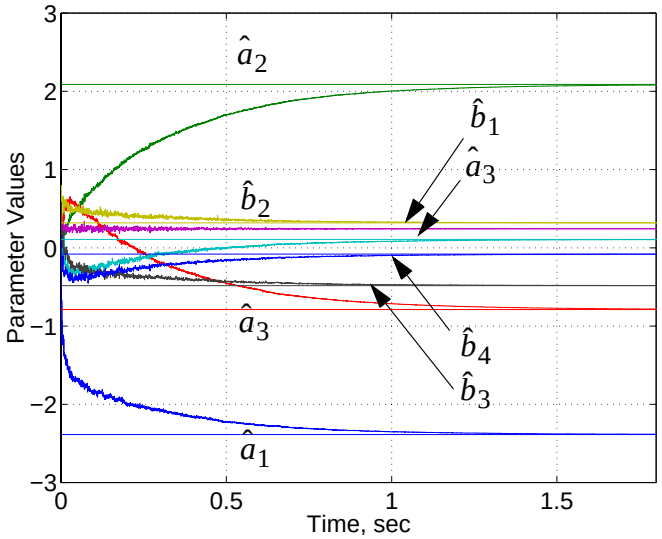

Figure 4-9. *Comparison of convergence of plant parameters.*

This set of simulations used the Seagate models from Section 2.4 to describe the behavior of the HDD. Experimental data was collected from a HDD mounted such that it was subjected to a rotational disturbance as shown in Fig. 4-8. This experimental data was

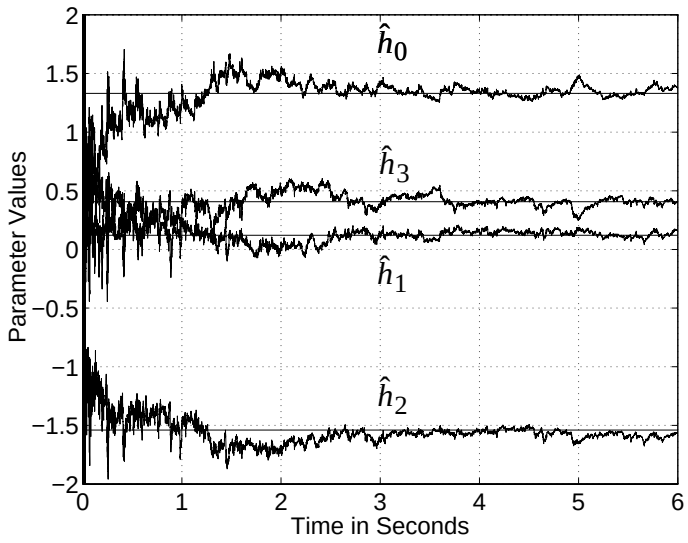

Figure 4-10. *Convergence of controller parameters.*

used to model the transfer function from disturbance to PES, $C(q^{-1})/A(q^{-1})$. Further, the accelerometer which was used in the experiments (described in Section 3.1.2) was modeled by Eq. (4-48).

A fourth order FIR filter was used for the compensator. As in the previous section, the optimal compensator as well as the optimal PES variance were computed by solving a Lyapunov equation. A full order estimation was done on the plant polynomials. Both PAA algorithms were run simultaneously using an additional excitation signal similar to the one described by Eq. (4-44). By the results of Theorem 3, both the plant and the optimal FIR filter estimates will converge to their true values.

The convergence of the plant parameters is shown in Fig. 4-9. For clarity, only $\hat{A}(q^{-1})$ and $\hat{B}(q^{-1})$ are shown. After approximately 1 second, the parameter values are within 10% of their expected values. The results are consistent with the results of Theorem 3. The convergence of the compensator parameters is displayed in Fig. 4-10. After 1 second, these parameter values are within 10% of their expected values. The expected value of improvement in the variance agreed with the simulated value which was 28.4%. The frequency response of the optimal compensator is shown in Fig. 4-11. Both the computed and estimated responses match since the FIR taps converge to the optimal values. The power spectral density of the position error signal for the various cases is

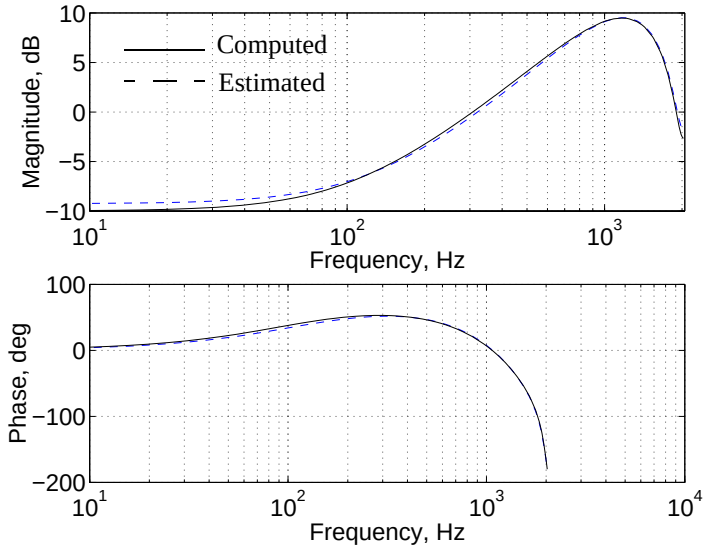

Figure 4-11. *Comparison of frequency response between recursive and optimal FIR filter.*

shown in Fig. 4-12. The solid line depicts the performance of the nominal controller only, while the dashed line represents the performance of the nominal controller with the adaptive accelerometer feedforward. The accelerometer feedforward scheme attenuates the disturbance by 3 db from 10 Hz to 100 Hz, 5 dB from 100 Hz to 500 Hz, and 10 dB from 700 Hz to the Nyquist frequency.

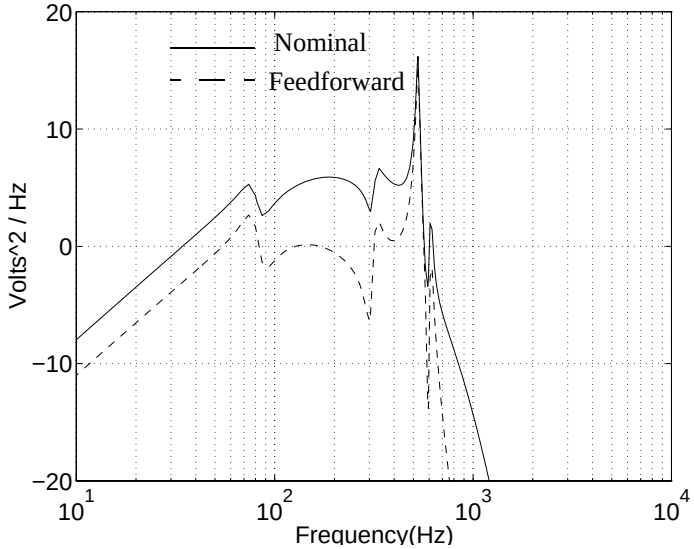

Figure 4-12. *Comparison of power spectral density of PES.*

The histogram of the PES is displayed in Fig. 4-13. For this simulation, the accelerometer feedforward decreased the 3σ value of the distribution from 18% to 12%.

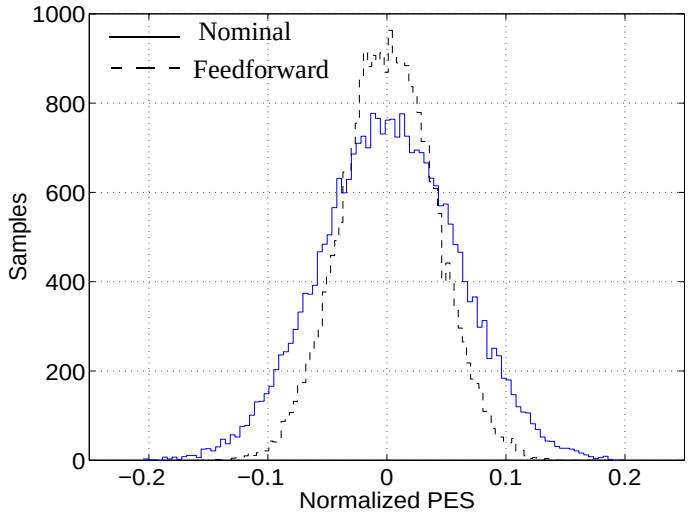

Figure 4-13. *Comparison of histogram of PES.*

5. EXPERIMENTAL RESULTS

5.1 CHARACTERIZATION OF VIBRATIONAL DISTURBANCES

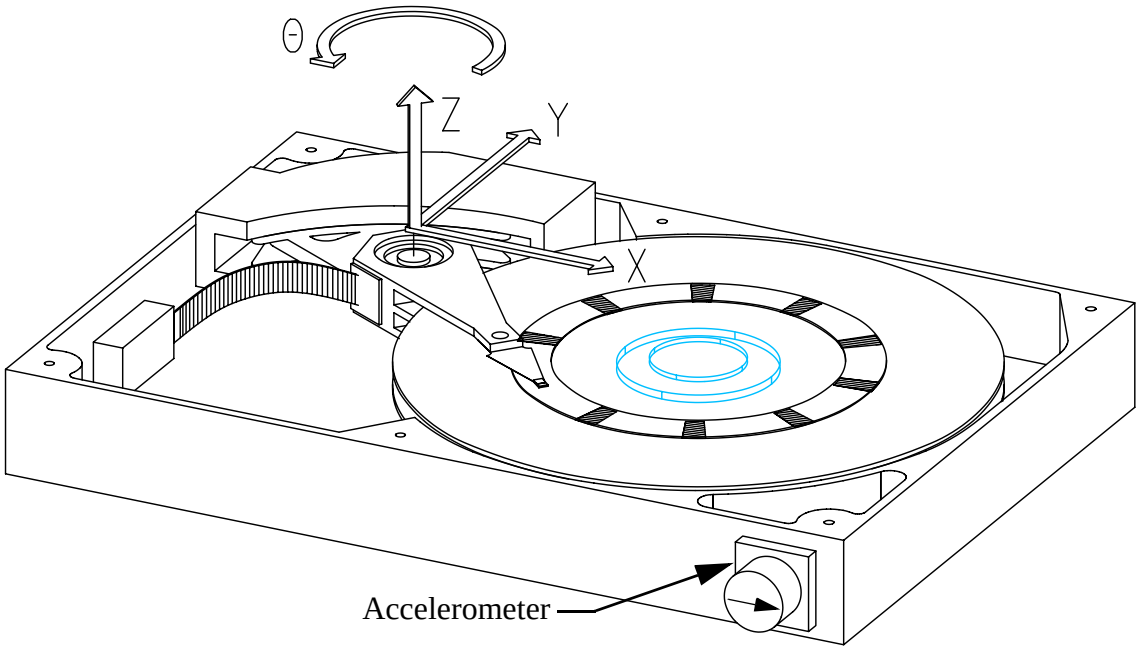

Figure 5-1. *Definition of the coordinate system for the vibrational disturbances. The x-axis is along the length of the drive, the y-axis is along the width, and the z-axis is perpendicular to the plane of the HDD. The rotational disturbance is about the center of the actuator bearing and in the plane of HDD. The axis of sensitivity is denoted by the small arrow inside the accelerometer.*

The HDD was subject to both single and random frequency disturbances about four axes. The definition for these different axes is shown in Fig. 5-1. The origin is at the center of rotation of the actuator bearing. The x-axis, y-axis, and rotation disturbances are in the plane of disk platters, while the z-axis is out of the plane. The effect of external disturbances was discussed in Section 2.2.2.4. Experimental data from the Seagate HDD will be shown to verify their detrimental effect. The transfer function from the accelerometer signal to the PES is shown in Fig. 5-2. The transfer function from disturbance to PES is not shown since the signal, $r(k)$ in Fig. 4-1, was not measurable. Notice that the transfer function of the rotational, x-axis, and y-axis are nearly identical. This similarity results from the fact that the actuator for this particular HDD is

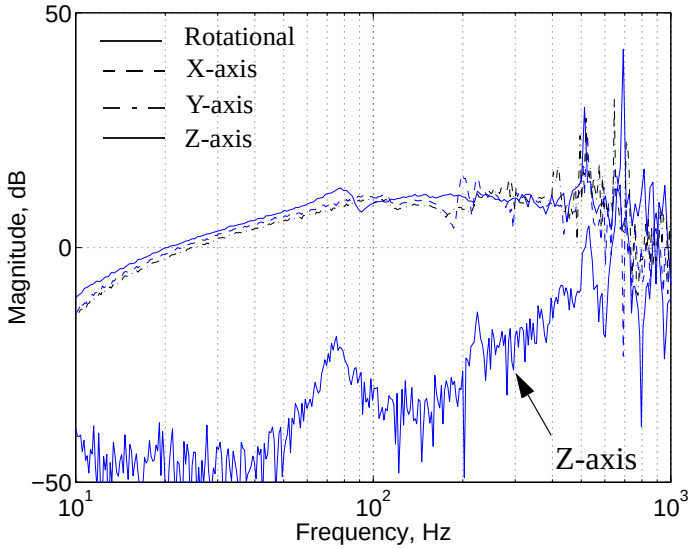

Figure 5-2. *Transfer function from the accelerometer signal to the PES for the rotational, x-axis, y-axis, and z-axis disturbances.*

unbalanced. Specifically, the center of mass of the actuator does not lie over the center of rotation of the actuator bearing. Hence, an external disturbance in any direction about the bearing will cause a torque on the actuator. However, in the out-of-plane direction, below 400 Hz the z-axis transfer function is 30 dB lower than the transfer functions for the other directions. Z-axis disturbances do not have a significant effect on the PES below 400 Hz. The relative insensitivity of the 2.5" HDD to z-axis disturbances is due to the high natural frequencies of the disk platters. The testing of a 3.5" drive would have shown the effect of the disk platter resonances as shown in Section 2.2.2.2 because of their lower natural frequencies.

To obtain an estimate of the transfer function, $G_{shk}(z^{-1})$ in Fig. 4-1 for the rotational disturbances, the models of the HDD from Section 2.4 and the model of the accelerometer from Section 4.5.1 were used in the following relationship

$$G_{shk}(z^{-1}) = G_{acc}(z^{-1})\left(\frac{1}{1 + P(z^{-1})K(z^{-1})}\right)^{-1}\left(\frac{Y(z^{-1})}{A(z^{-1})}\right). \qquad (5\text{-}1)$$

The frequency response of Eq. (5-1) is displayed in Fig. 5-3. The large DC component is clearly evident, and it is due to the rigid-body motion and the unbalanced actuator. The spindle rocking modes are also evident at the higher frequencies.

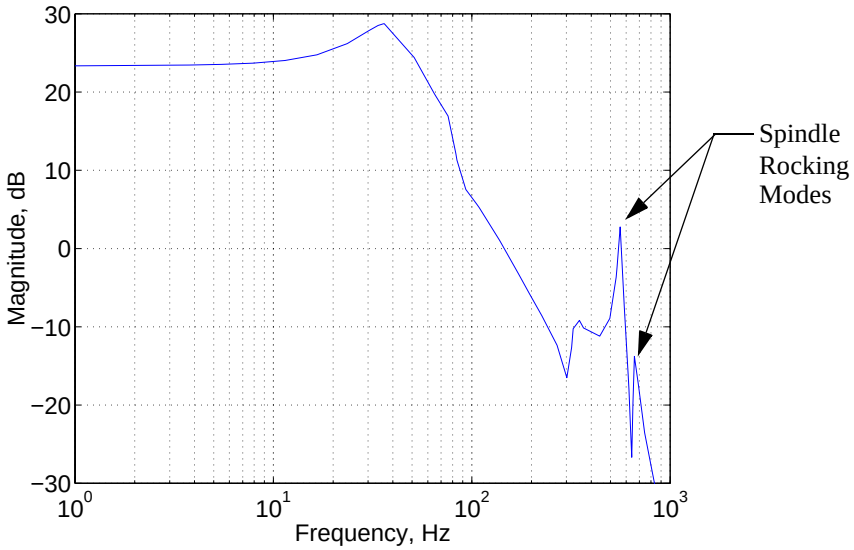

Figure 5-3. *Estimate of the mechanical dynamics, $G_{shk}(z^{-1})$, which convert the external disturbance to the track runout for rotational disturbances.*

5.2 Performance of Adaptive Scheme

5.2.1 Algorithm Modifications for Implementation

In order to implement the adaptive controller on an existing HDD, a number of modifications must be made. Of primary importance is the speed of the algorithm because there are a limited number of computational cycles for the control algorithm. Even with the 'C40 processor used in these experiments, the plant and FIR PAAs could not be run synchronously without using a multirate scheme. A multirate scheme was not pursued here since a successful implementation of a multirate adaptive scheme similar to the scheme presented in Chapter 4 was demonstrated by Horowitz and Li[56]. Since the position dependence of the plant of the HDD is calibrated out in current products, only plant parameter variations with temperature are of concern. For significant temperature changes, the plant PAA gain can be periodically reset to capture these parameter variations. Note that since the adaptive gain decays as $1/k$, the gain for both the plant and FIR PAAs will have to be reset to capture long term variations. In the experiments presented in the following section, the add-on adaptive servo was disabled and a persistently exciting input signal of sufficiently high magnitude was introduced in order to

pre-estimate the nominal closed-loop transfer function. After this open-loop identification stage, the random exciting signal was turned off, and the optimal FIR filter PAA was active during the second feedforward control stage.

Further, since the VCM in HDD's has a high sensitivity to the control input, it was possible to introduce an input signal which results in an output with a large signal to noise ratio and sufficient persistence of excitation. As a consequence, it was possible to identify the parameters of the nominal closed-loop complementary sensitivity transfer function, $B_d(q^{-1})/A_d(q^{-1})$, without identifying the noise polynomial, $C(q^{-1})$. Furthermore, since $B_d(q^{-1})/A_d(q^{-1}) = B(q^{-1})/A(q^{-1})$, all the theoretical results presented in Section 4.4 hold.

5.2.2 ROTATIONAL DISTURBANCE

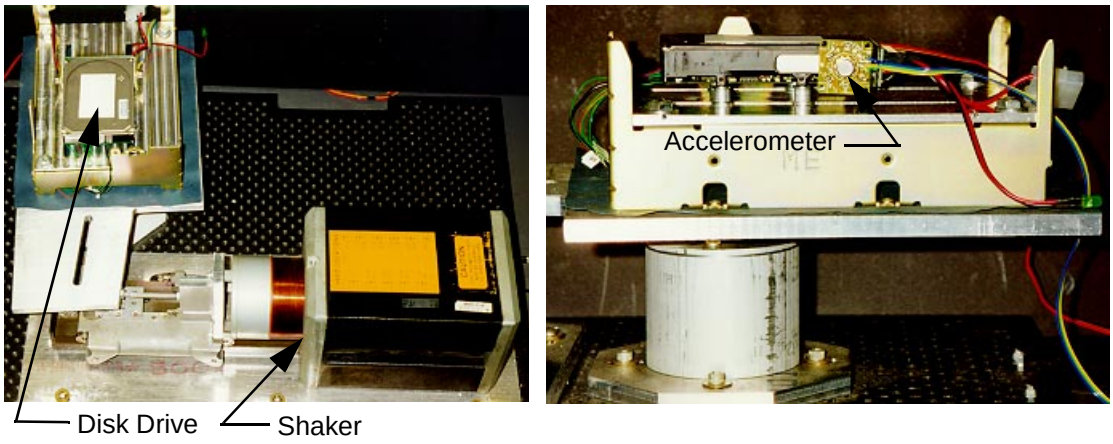

Figure 5-4. *Experimental setup showing the 2.5" Seagate HDD configured to receive a rotational disturbance. On the left is an overview of the apparatus. On the right, a close up of the HDD showing one on the ADXL05 accelerometers.*

The first experimental test conducted on the HDD was to subject it to a random rotational disturbance. The experimental setup for this configuration is shown in Fig. 5-4. The HDD was subjected to a random disturbance whose peak value of acceleration was 170 rad/sec^2. Both 5 and 10-tap FIR filters were used for $\hat{Q}(q^{-1})$.

To verify the performance of the plant PAA, a comparison of the frequency response of the transfer function from auxiliary control input, $u(k)$, to PES is shown in Fig. 5-5. As stated in Section 5.2.1, only the $A_d(q^{-1})$ and $B_d(q^{-1})$ polynomials were identified.

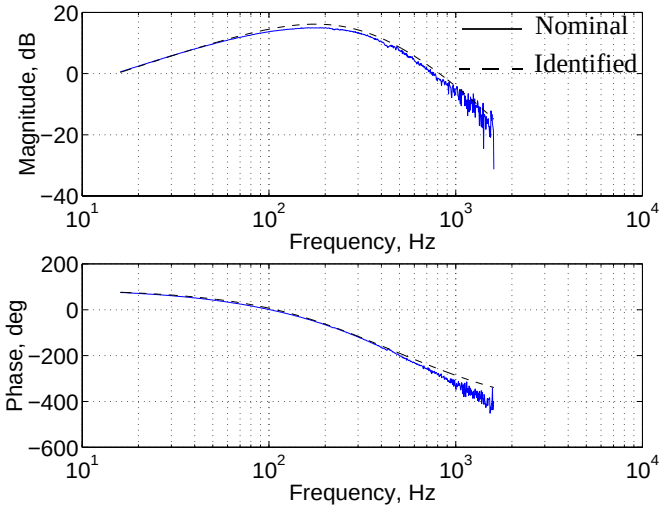

Figure 5-5. *Comparison of the frequency response for the experimentally measured and identified transfer functions from the auxiliary control input to the PES.*

The SNR was large enough so that the bias caused by the nominal noise is insignificant. The plant PAA was implemented with $F_\theta(0) = 1$, $\lambda_\theta = 0.1$, and $\beta_\theta = 1$.

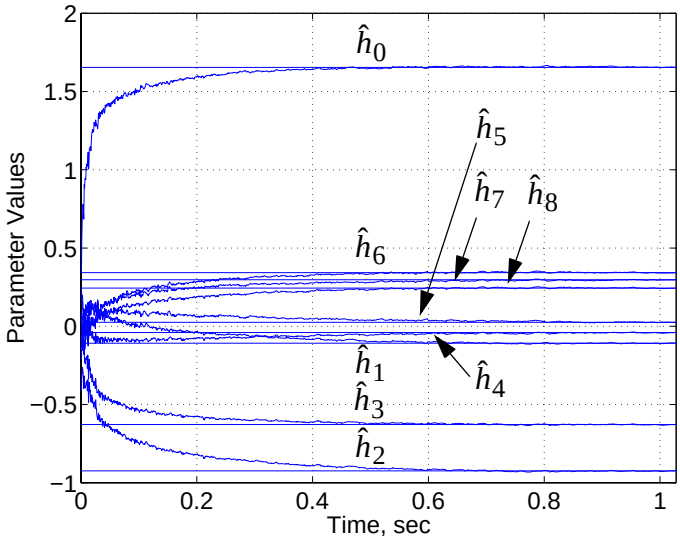

Figure 5-6. *Convergence of the FIR filter parameters for the external rotational disturbance experiment.*

Using Result 2 from Theorem 2, since $\hat{\theta}$ converges such that $B/A = B/A$ then $\hat{H}$ converges to H^o which is the optimal Wiener filter parameter vector. The convergence of the FIR parameters is displayed in Fig. 5-6. The FIR PAA was implemented with $F_Q(0) = 1$, $\lambda_Q = 0.1$, and $\beta_Q = 1$. Only the first nine FIR filter parameters are

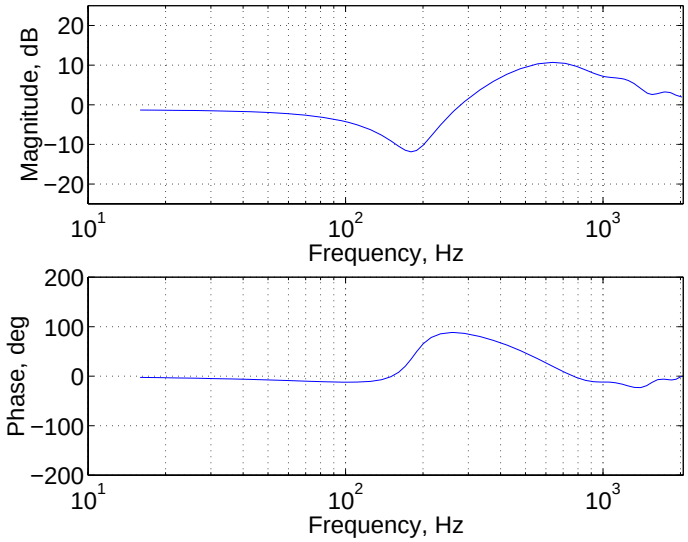

Figure 5-7. *Frequency response of the optimal FIR filter for the external rotational disturbance experiment.*

shown since there was not enough onboard memory on the ‘C40 to save the tenth. In this case, the horizontal lines to which the parameters are converging are not representative of a computed optimal Wiener FIR filter. These horizontal lines are merely aids in visualizing the convergence of the parameters; but as stated above, from Theorem 2, they are the optimal Wiener parameters. The FIR filter parameters are within 10% of their steady state value in approximately 200 msec which is 15 revolutions of the disk. However, it should be noted that an improvement in the PES is seen within a few milliseconds.

The frequency response of the FIR filter is shown in Fig. 5-7. From Result 2 of Theorem 2, this FIR filter is the optimal filter that minimizes the variance of the PES caused by the external disturbance.

The power spectral density of the PES is displayed in Fig. 5-8. The solid line depicts the performance of the nominal controller under only the influence of the external disturbance, while the dash-dot and dashed lines represent the performance of the nominal controller with a 5 and 10-tap adaptive feedforward filter respectively. The lower solid line displays the nominal power spectral density with the nominal servo without the disturbance. The 5-tap adaptive feedforward scheme attenuated the disturbance

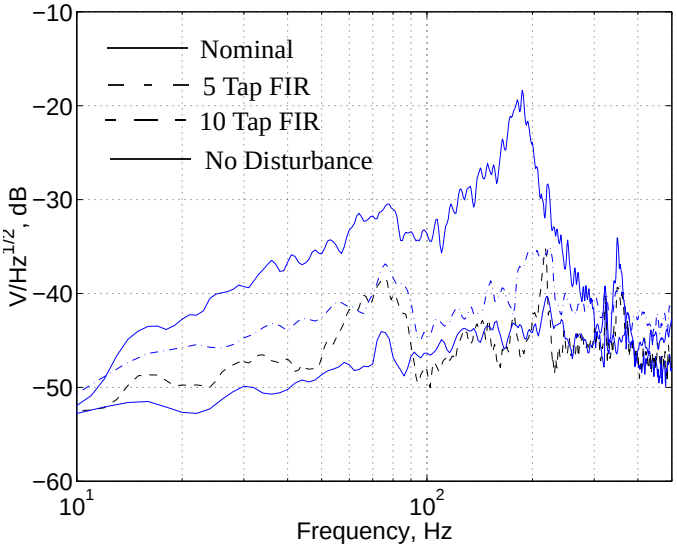

Figure 5-8. *Power spectral density of the PES for the random external rotational disturbance experiment.*

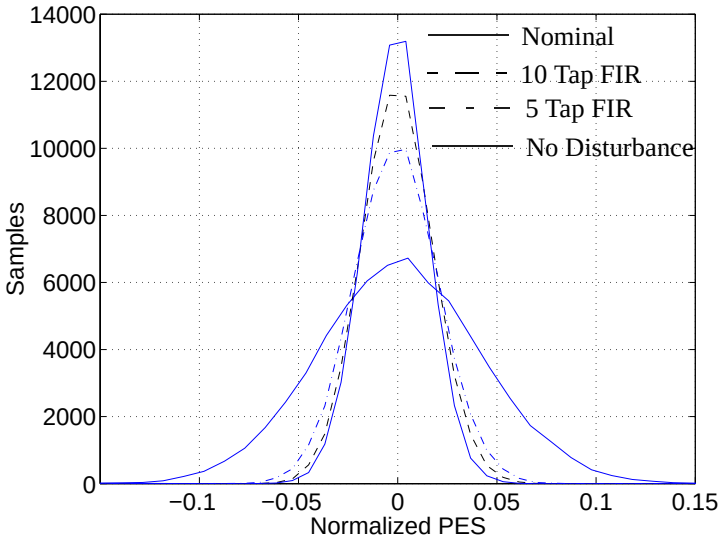

Figure 5-9. *Histogram of the PES for the random external rotational disturbance experiment.*

approximately 5 dB from 20 Hz to 100 Hz and 10 dB from 100 Hz to 200 Hz. The 10-tap adaptive feedforward scheme attenuated the disturbance approximately 10 dB from 20 Hz to 100 Hz and 15 dB from 100 Hz to 200 Hz. Hence by increasing the filter size by a factor of two, 5 dB more of attenuation was achieved across the frequency range. However, as stated in [92], increasing the number of FIR filter parameters does not always improve the performance. This result was observed in experiments where no significant

improvements could be detected beyond a 15-tap FIR filter which requires a significant amount of additional computational time.

The histogram of the PES is shown in Fig. 5-9. The PES has been normalized to the track width of the 2.5" Seagate HDD. The 5-tap FIR filter decreased the 3σ value of the distribution from 12% to 7%, while the 10-tap FIR filter decreased the 3σ value from 12% to 5% which was close to the nominal 3σ value of 4.5%. The overall reduction of the variance was 68% and 89% for the 5 and 10-tap filter, respectively. This amount of reduction was a significant improvement. Without the adaptive servo, the HDD can not read nor write; but with the adaptive servo, the HDD functions normally. A summary of the results for the rotational tests are listed in Table 5-1.

Frequency	$\hat{n}_Q$	$F_Q(0)$	λ_Q	β_Q	Maximum Attenuation	3σ	Reduction of Variance
Random	4	1	0.1	1	10 dB	7%	68%
Random	9	1	0.1	1	15 dB	5%	89%

Table 5-1. *Comparison of the results for different size compensators for the random external rotational disturbance experiments.*

5.2.3 X-AXIS DISTURBANCE

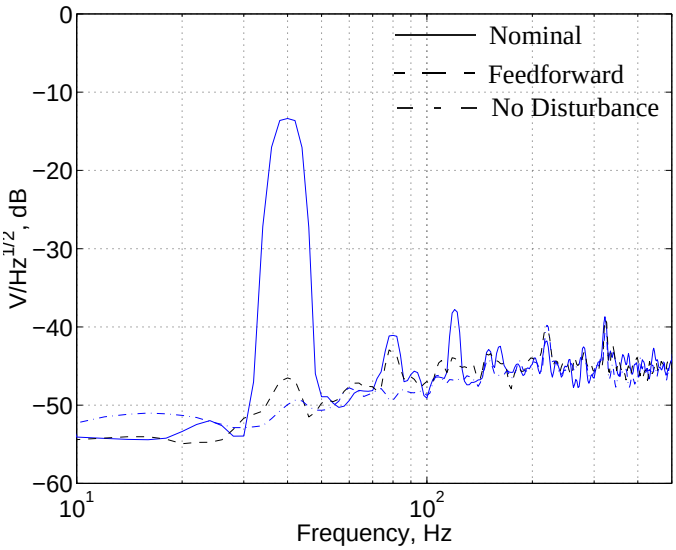

Figure 5-10. *Power spectral density of the PES for the 40 Hz external x-axis disturbance experiment.*

The next experimental test conducted on the HDD was to subject it to a single frequency disturbance at 40 Hz along the x-axis as defined in Fig. 5-1. A HDD can be subjected to a variety of single frequency disturbances. The most common is the 60 Hz disturbance from the power supply fan. Another source of single frequency disturbances is other HDD's mounted in the same computer or in a RAID system. A RAID system can contain many different HDD's whose spindle rotation frequency can excite the vibrational modes of other HDD's. For the test results shown here, the peak value of the disturbance was 3 G. A 5-tap FIR filter was used for $\hat{Q}(q^{-1})$ with $F_Q(0) = 1$, $\lambda_Q = 0.05$, and $\beta_Q = 1$.

The power spectral density of the PES is displayed in Fig. 5-10. The solid line depicts the performance of the nominal controller only in the presence of the external disturbance, while the dashed line represent the performance of the nominal controller with a 5-tap adaptive feedforward filter. The lower dash-dot line displays the nominal power spectral density with the nominal servo without the disturbance. The 5-tap adaptive feedforward scheme attenuated the fundamental frequency of the disturbance by approximately 30 dB. The second harmonic was attenuated by approximately 6 dB, while the first harmonic (80 Hz) was relatively unchanged. The harmonics appear since the shaker used for these

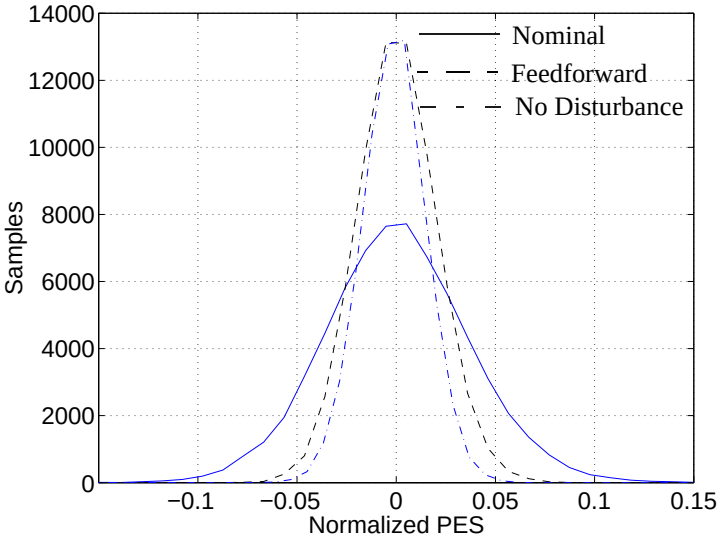

Figure 5-11. *Histogram of the PES for the 40 Hz external x-axis disturbance experiment.*

experiments has a significant nonlinear component.

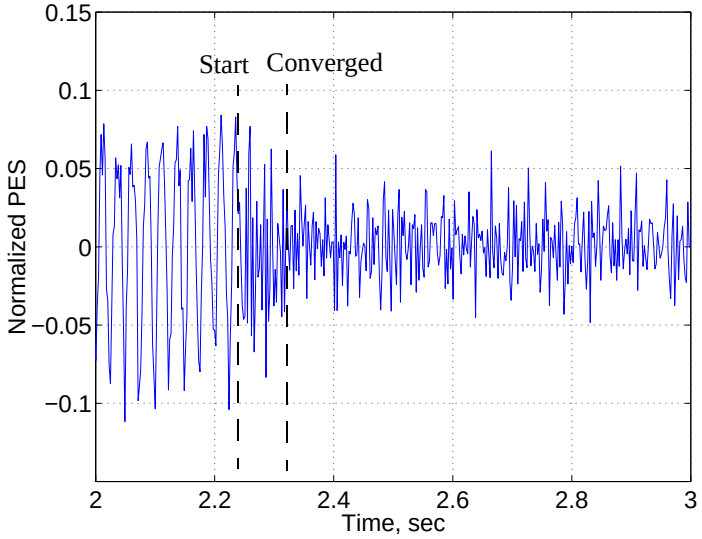

Figure 5-12. *Time response of the PES for the 40 Hz external x-axis disturbance experiment.*

The histogram of the PES is shown in Fig. 5-11. The 5-tap FIR filter decreased the 3σ value of the distribution from 12% to 6% which close to the nominal 3σ value of 4.5%. The overall reduction of the variance was 70%. Again, the amount of reduction was a significant improvement since without the adaptive servo, the HDD cannot read nor write; but with the adaptive servo, the HDD functions normally.

The dramatic reduction in the PES is shown in Fig. 5-12. The 5-tap FIR filter converged in approximately 75 msec which was 5.5 revolutions of the disk. The increase in convergence rate was due to a lower value of λ_Q used; λ_Q = 0.05 for this experimental run.

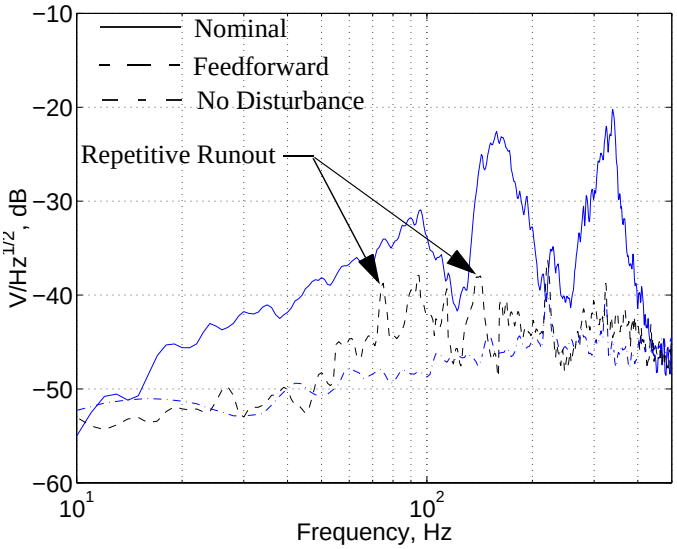

Figure 5-13. *Power spectral density of the PES for the random external x-axis disturbance experiment.*

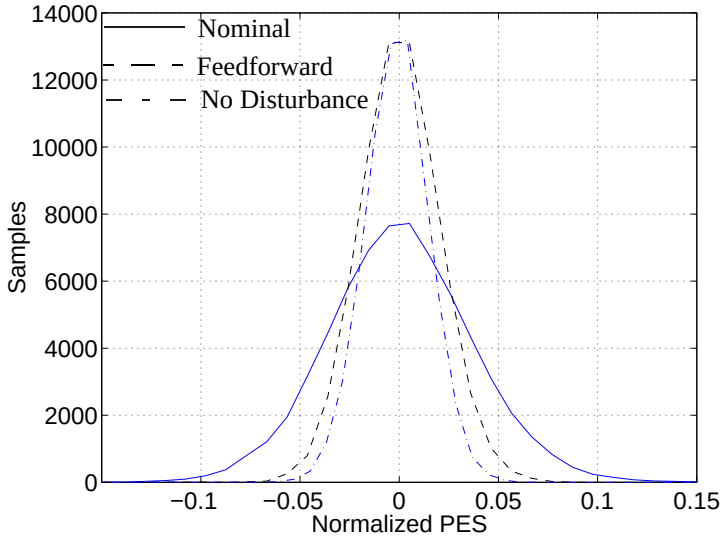

Figure 5-14. *Histogram of the PES for the random external x-axis disturbance experiment.*

In another experiment, the HDD was subjected to a random external disturbance

whose peak value of acceleration was 3 G. A 10-tap FIR filter was used for $\hat{Q}(q^{-1})$ such that the performance could be compared to the rotational case with $F_Q(0) = 1$, $\lambda_Q = 0.05$, and $\beta_Q = 1$.

The power spectral density of the PES is displayed in Fig. 5-13. The 10-tap adaptive feedforward scheme attenuated the disturbance approximately 10 dB from 20 Hz to 100 Hz, 15 dB from 130 Hz to 200 Hz, and 10 dB from 250 Hz to 290 Hz. The performance was similar to the performance during the random rotational disturbance experiment. Notice that the fundamental and first harmonic of repetitive runout were excited by this disturbance. The accelerometers were intentionally mounted to prevent the detection of repetitive runout, and hence it was not attenuated.

The histogram of the PES is shown in Fig. 5-14. The 10-tap FIR filter decreased the 3σ value of the distribution from 12% to 6%. The overall reduction of the variance was 78%. Again, the amount of reduction was a significant improvement since with the adaptive servo, the HDD functions normally. A summary of the results for the x-axis tests are listed in Table 5-2.

Frequency	$\hat{n}_Q$	$F_Q(0)$	λ_Q	β_Q	Maximum Attenuation	3σ	Reduction of Variance
40 Hz	4	1	0.05	1	30 dB	6%	70%
Random	9	1	0.05	1	15 dB	6%	78%

Table 5-2. *Comparison of the results for different frequency x-axis disturbance experiments.*

5.2.4 Y-Axis Disturbance

The next experimental test conducted on the HDD was to subject it to a single frequency disturbance along the y-axis as defined in Fig. 5-1. The HDD was subjected to a 250 Hz external disturbance whose peak value of acceleration was 3 G. A 5-tap FIR filter was used for $\hat{Q}(q^{-1})$ with $F_Q(0) = 1$, $\lambda_Q = 0.01$, and $\beta_Q = 1$.

The power spectral density of the PES is displayed in Fig. 5-15. The 5-tap adaptive feedforward scheme attenuated the fundamental frequency of the disturbance

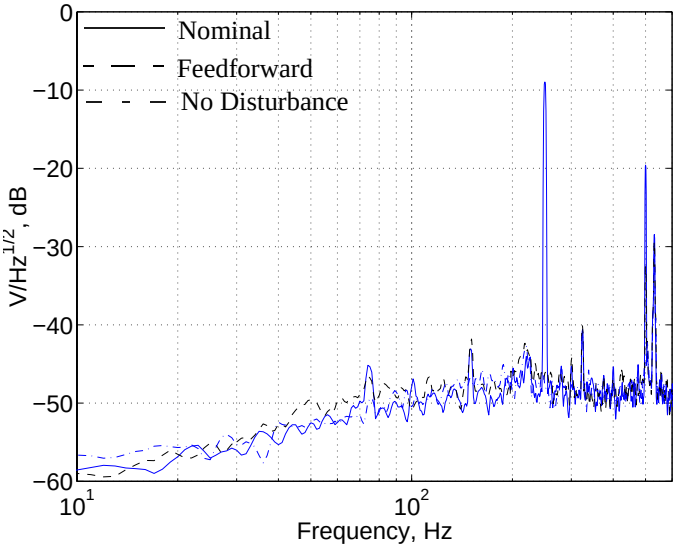

Figure 5-15. *Power spectral density of the PES for the 250 Hz y-axis disturbance experiment.*

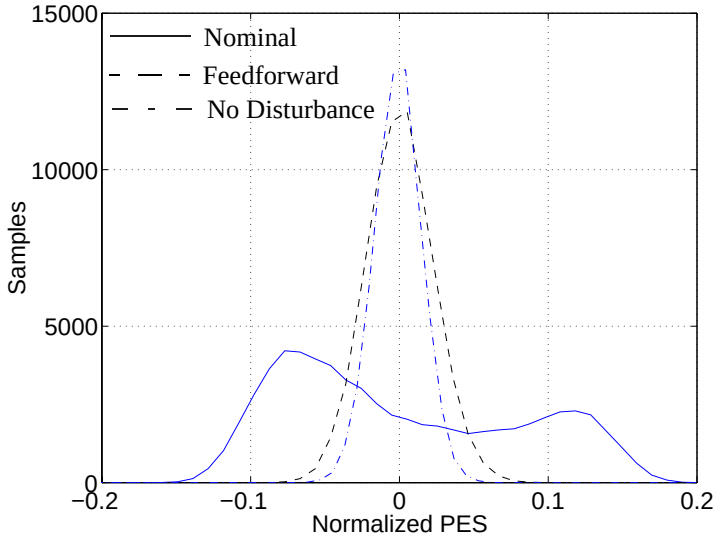

Figure 5-16. *Histogram of the PES for the 250 Hz external y-axis disturbance experiment.*

approximately 37 dB. The first harmonic was attenuated by approximately 15 dB.

The histogram of the PES is shown in Fig. 5-16. The 5-tap FIR filter decreased the 3σ value of the distribution from 14% to 8%. Again, the amount of reduction was a significant improvement since with the adaptive servo, the HDD can function normally. The overall reduction of the variance was 75%. The dramatic reduction in the PES is shown in Fig. 5-17. The 5-tap FIR filter converged in approximately 50 msec which was

3.5 revolutions of the disk.

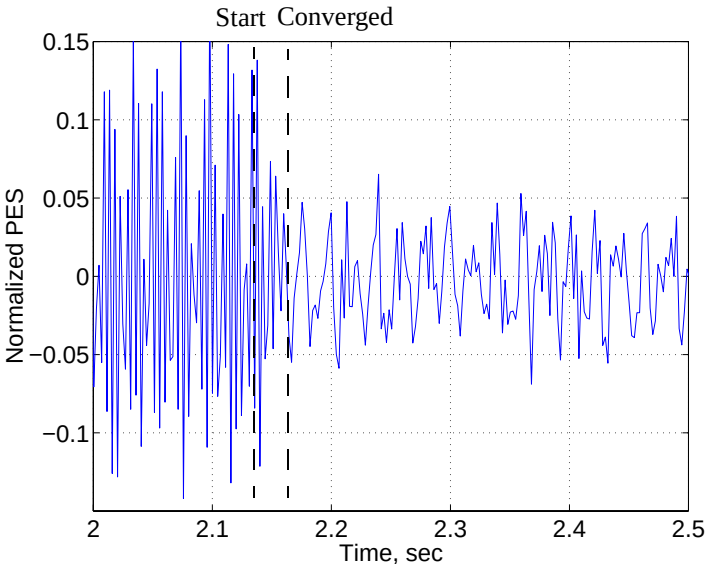

Figure 5-17. *Time response of the PES for the 250 Hz external y-axis disturbance experiment.*

Next the HDD was tested by subjecting it to a random frequency disturbance along the y-axis. The HDD was subjected to a random external disturbance whose peak value of acceleration was 3 G. A 10-tap FIR filter was used for $\hat{Q}(q^{-1})$ so that the performance could be compared to the rotational case.

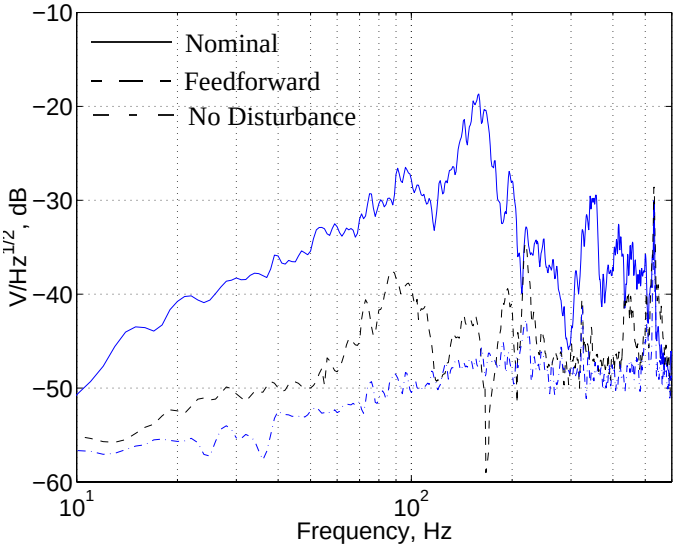

Figure 5-18. *Power spectral density of the PES for the random external y-axis disturbance experiment.*

The power spectral density of the PES is displayed in Fig. 5-18. The 10-tap adaptive feedforward scheme attenuated the disturbance approximately 10d B from 20 Hz to 100 Hz, 15 dB from 130 Hz to 200 Hz, and 10 dB from 220 Hz to 400 Hz. The performance was similar to the performance of the random rotational disturbance experiment.

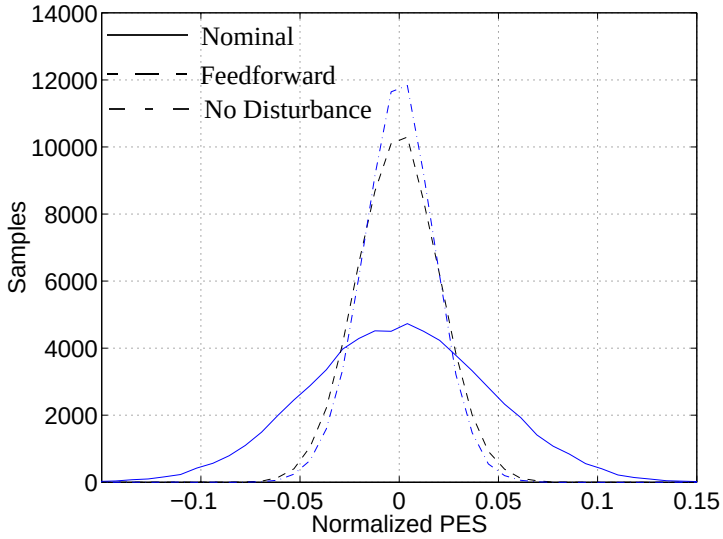

Figure 5-19. *Histogram of the PES for the random external y-axis disturbance.*

The histogram of the PES is shown in Fig. 5-19. The 10-tap FIR filter decreased the 3σ value of the distribution from 12% to 6% which was close to the nominal 3σ level of 4.5%. Again, the amount of reduction was a significant improvement since with the adaptive servo, the HDD can function normally. The overall reduction of the variance was 86%. A summary of the results for the y-axis tests are listed in Table 5-3.

Frequency	$\hat{n}_Q$	$F_Q(0)$	λ_Q	β_Q	Maximum Attenuation	3σ	Reduction of Variance
250 Hz	4	1	0.01	1	37 dB	8%	75%
Random	9	1	0.01	1	15 dB	6%	86%

Table 5-3. *Comparison of the results for the different frequency y-axis disturbance experiments.*

5.2.5 Z-Axis Disturbance

The next experimental test conducted on the HDD was to subject it to a single

frequency disturbance along the z-axis as defined in Fig. 5-1. Disturbances along this axis greatly effect the PES at higher frequencies. As discussed in Section 5.1, since the HDD is a 2.5" form factor, the natural frequencies of the disk platters are well above the Nyquist frequency. However, a significant amount of PES can be generated for disturbances below the Nyquist frequency. First, the HDD was subjected to a 500 Hz external disturbance whose peak value of acceleration was 3 G. A 5-tap FIR filter was used for $\hat{Q}(q^{-1})$ with $F_Q(0) = 1$, $\lambda_Q = 0.01$, and $\beta_Q = 1$ which were the same as used in the y-axis case.

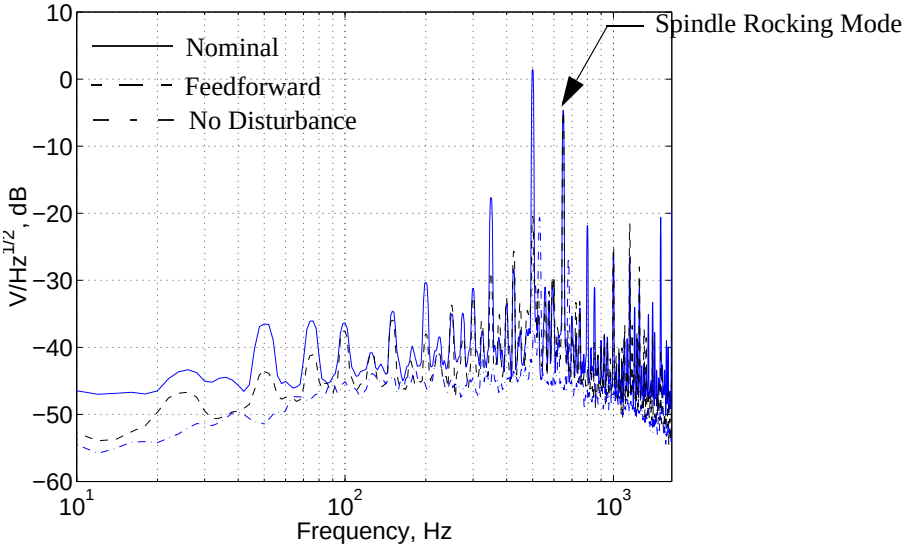

Figure 5-20. *Power spectral density of the PES for the 500 Hz external z-axis disturbance experiment.*

The power spectral density of the PES is displayed in Fig. 5-20. Notice that there are many more peaks than just the 500 Hz and its harmonics. The natural frequencies of the test stand were also excited by this test. Hence, the disturbance used in this test was extremely detrimental to the servo performance of the HDD. The 5-tap adaptive feedforward servo attenuated the 500 Hz disturbance by approximately 20 dB. It also attenuated the disturbances from 10 Hz to 100 Hz by 5 dB. Further, the disturbances at 200 Hz, 350 Hz, 800 Hz, and 850 Hz were attenuated by approximately 10 dB. Again, the spindle rocking mode is evident, but it was not attenuated because it was not sensed by the accelerometer.

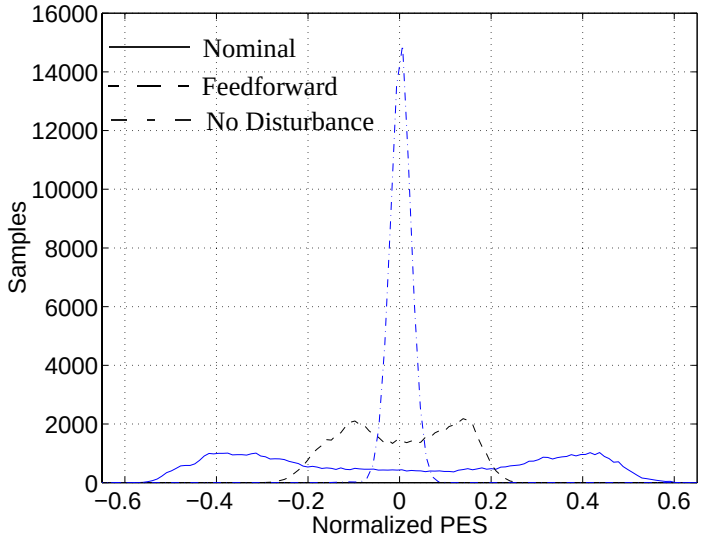

Figure 5-21. *Histogram of the PES for the 500 Hz external z-axis disturbance.*

The histogram of the PES is shown in Fig. 5-21. The 5-tap FIR filter decreased the 3σ value of the distribution from 57% to 23%. In this case, however, even with the adaptive feedforward servo the HDD cannot read nor write. The level of disturbance was too severe to be attenuated by a 5-tap FIR filter. The overall reduction of the variance was 53%.

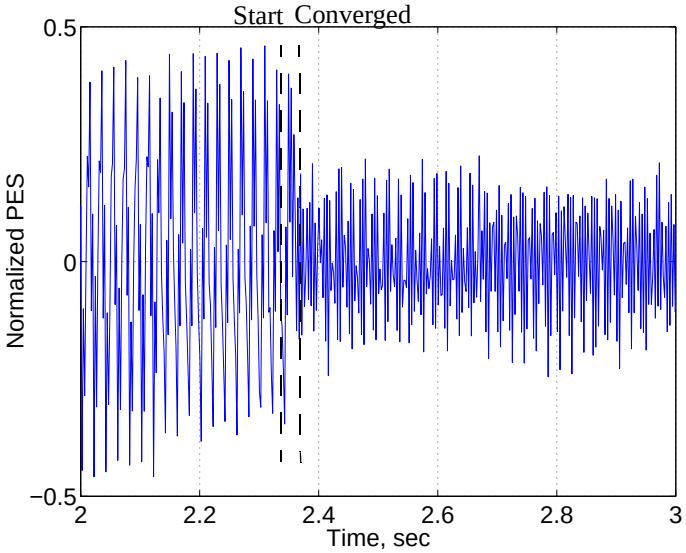

Figure 5-22. *Time response of the PES for the 500 Hz external z-axis disturbance experiment.*

The dramatic reduction in the PES which is in Fig. 5-22. The 5-tap FIR filter converged in approximately 25 msec which was 2 revolutions of the disk.

Next the HDD was subjected to a random external disturbance whose peak value of acceleration was 3 G. A 10-tap FIR filter was used for $\hat{Q}(q^{-1})$

The power spectral density of the PES is displayed in Fig. 5-23. The 10-tap adaptive feedforward scheme attenuated the disturbance approximately 15 dB from 200 Hz to 240 Hz and 10 dB from 130 Hz to 200 Hz.

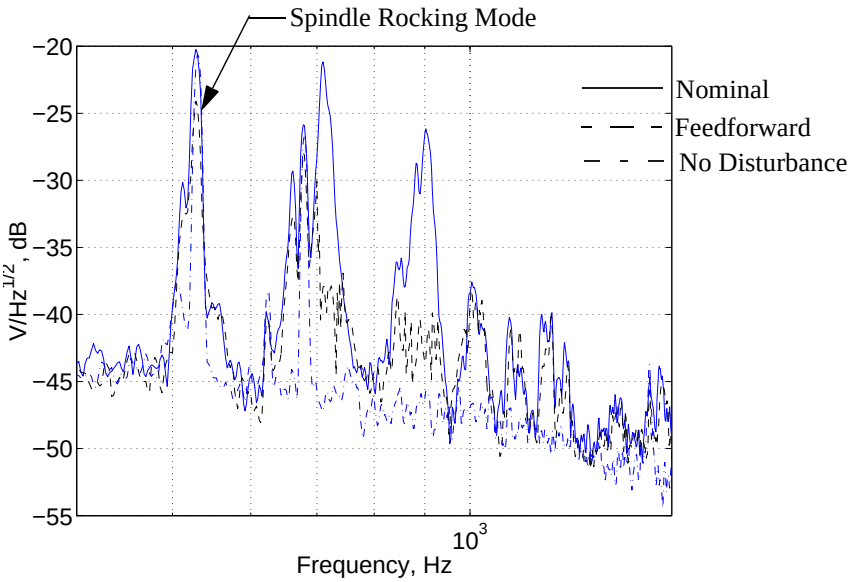

Figure 5-23. *Power spectral density of the PES for the random external z-axis disturbance experiment.*

The histogram of the PES is shown in Fig. 5-24. The 5-tap FIR filter decreased the 3σ value of the distribution from 28% to 11%. With the adaptive servo, the HDD is barely below the TMR budget to allow reading and writing. The overall reduction of the variance was 53%. A summary of the results for the z-axis tests are listed in Table 5-4.

Frequency	$\hat{n}_Q$	$F_Q(0)$	λ_Q	β_Q	Maximum Attenuation	3σ	Reduction of Variance
500 Hz	4	1	0.01	1	20 dB	23%	53%
Random	9	1	0.01	1	15 dB	11%	58%

Table 5-4. *Comparison of the results for the different frequency z-axis disturbance experiments.*

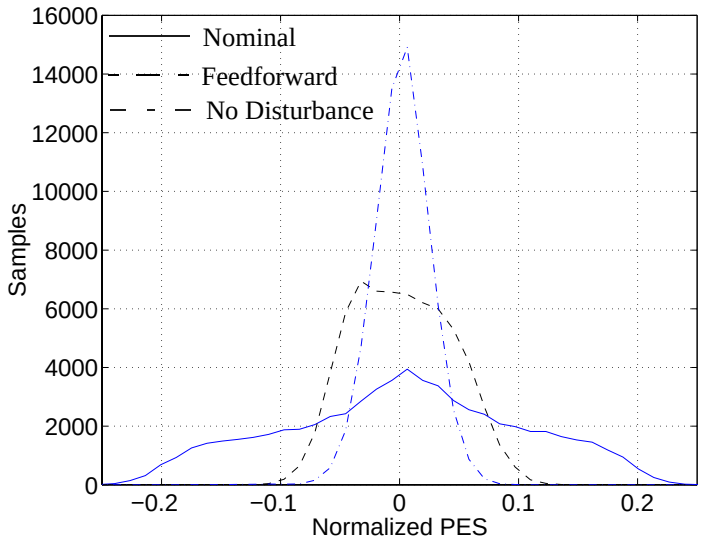

Figure 5-24. *Histogram of the PES for the random external z-axis disturbance experiment.*

5.2.6 STATIONARY FIR FILTER

The results in this section are based on using a stationary FIR filter for $\hat{Q}(q^{-1})$. The converged parameter values of $\hat{Q}(q^{-1})$ from the 5-tap random external rotational disturbance trial were used. Comparisons of the performance between this stationary and the adaptive feedforward servos are made.

The stationary feedforward servo was first tested with a single frequency 60 Hz rotational disturbance. The parameters for the 5-tap adaptive FIR filter were $F_Q(0) = 1$, $\lambda_Q = 0.01$, and $\beta_Q = 1$. The power spectral density of the PES is displayed in Fig. 5-25. The solid line depicts the performance of the nominal controller only in the presence of the external disturbance, while the dashed and the dash-dot lines represent the performance of the nominal controller with a stationary and adaptive 5-tap feedforward servo respectively. The 5-tap stationary feedforward servo attenuated the fundamental frequency of the disturbance approximately 9 dB. The second and third harmonics were also attenuated by approximately 9 dB. The 5-tap adaptive feedforward servo attenuated the fundamental frequency of the disturbance approximately 39 dB. The second and third harmonics were attenuated by approximately 9 dB. Hence the improvement with the adaptive servo is significantly greater than with the stationary servo.

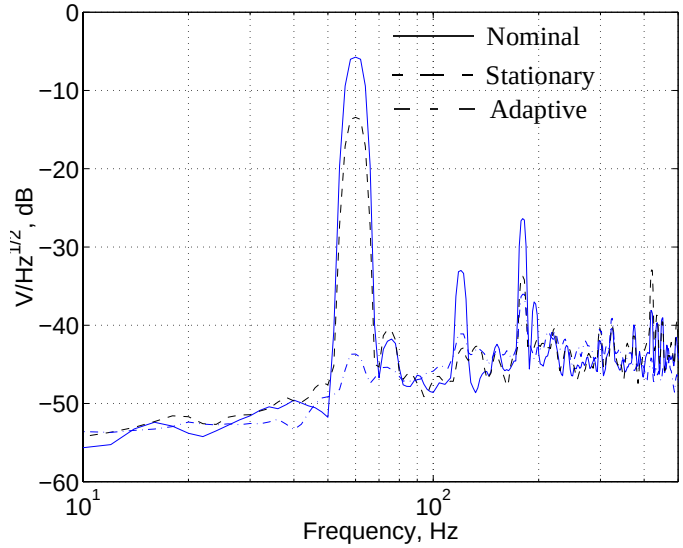

Figure 5-25. *Power spectral density of the PES for the 60 Hz external rotational disturbance using a 5-tap stationary FIR filter obtained from the random external rotational disturbance trial.*

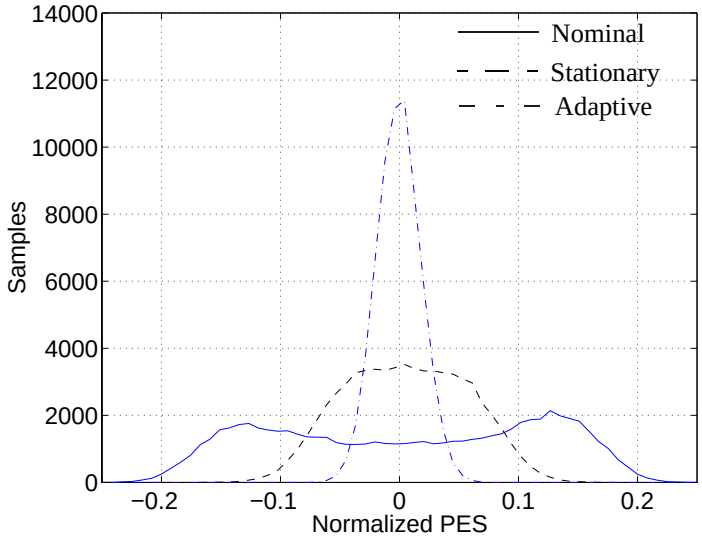

Figure 5-26. *Histogram of the PES for the 60 Hz external rotational disturbance using a 5-tap stationary FIR filter obtained from the random external rotational disturbance trial.*

The histogram of the PES is shown in Fig. 5-26. The stationary 5-tap FIR filter decreased the 3σ value of the distribution from 22% to 12%, while the adaptive 5-tap FIR filter decreased the 3σ value of the distribution from 22% to 6%. Both compensators

succeeded in attenuating the effect of the disturbance to such a degree that the HDD functions normally. The overall reduction of the variance was 38% and 85% for the stationary and adaptive filters respectively.

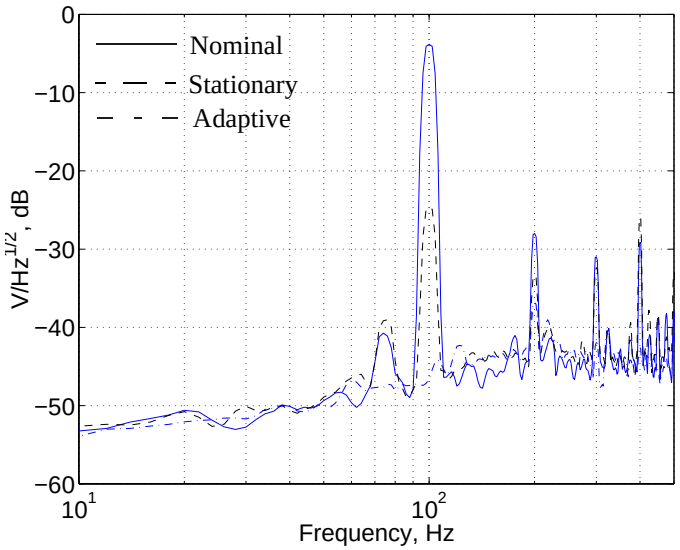

Figure 5-27. *Power spectral density of the PES for the 100 Hz external rotational disturbance using a 5-tap stationary FIR filter obtained from the random external rotational disturbance trial.*

Next, the stationary feedforward servo was tested with a single frequency 100 Hz rotational disturbance. The parameters for the 5-tap adaptive FIR filter were $F_Q(0) = 1$, $\lambda_Q = 0.01$, and $\beta_Q = 1$. The power spectral density of the PES is displayed in Fig. 5-27. The 5-tap stationary feedforward servo attenuated the fundamental frequency of the disturbance approximately 20 dB. The second harmonic was attenuated by approximately 5 dB. The 5-tap adaptive feedforward servo attenuated the fundamental frequency of the disturbance approximately 40 dB. The second harmonic was attenuated by approximately 10 dB. Even though the stationary FIR filter attenuated the effect of the disturbance significantly, the improvement with the adaptive servo is significantly greater.

The histogram of the PES is shown in Fig. 5-28. The stationary 5-tap FIR filter decreased the 3σ value of the distribution from 22% to 11%, while the adaptive 5-tap FIR filter decreased the 3σ value of the distribution from 22% to 5%. Both compensators succeeded in attenuating the effect of the disturbance to such a degree that the HDD

functions normally. The overall reduction of the variance was 58% and 94% for the stationary and adaptive filters respectively. A summary of the results for the comparison between compensators are listed in Table 5-5.

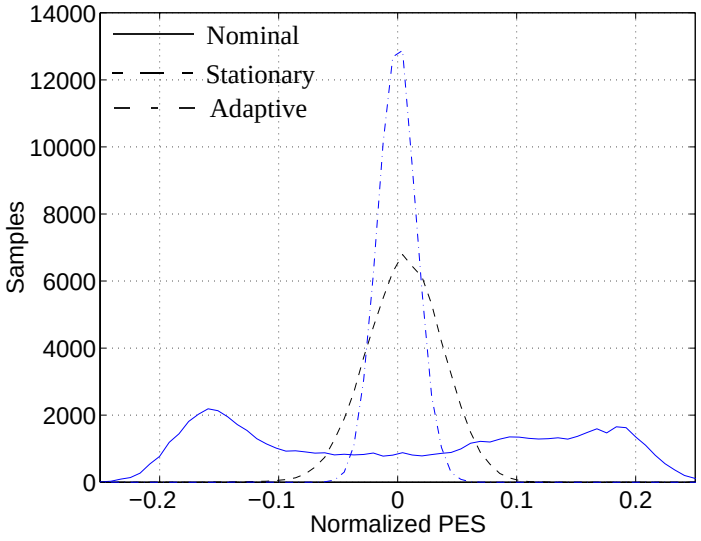

Figure 5-28. *Histogram of the PES for the 100 Hz external rotational disturbance using a 5-tap stationary FIR filter obtained from the random external rotational disturbance trial.*

Method	Frequency	$\hat{n}_Q$	Maximum Attenuation	3σ	Reduction of Variance
Stationary	60 Hz	4	9 dB	12%	38%
Adaptive	60 Hz	4	39 dB	6%	85%
Stationary	100 Hz	4	20 dB	11%	58%
Adaptive	100 Hz	4	40 dB	5%	94%

Table 5-5. *Comparison of the results between the stationary and adaptive feedforward servo experiments.*

5.3 COMPARISON OF ALGORITHMS

The performance of the algorithm was compared to two previously developed disturbance rejection schemes: the Horowitz-Li compensator[56] and the filtered-x scheme[88] developed by M. White and M. Tomizuka.

5.3.1 HOROWITZ-LI COMPENSATOR

The control law given by Eq. (4-38) is different from the control law given by R. Horowitz and B. Li[56] since the accelerometer signal is used directly instead of feeding back the estimate of the disturbance, $\hat{e}(k)$. The control law given by R. Horowitz and B. Li in [56] is

$$u(k) = \hat{Q}(k-1, q^{-1})\hat{e}(k), \tag{5-2}$$

where $\hat{e}(k) = y(k) - (\hat{B}(q^{-1})/\hat{A}(q^{-1}))u(k)$. Further in [56], $\hat{x}(k)$ in Eq. (4-35) and Eq. (4-36) is replaced by

$$\hat{A}(k, q^{-1})\hat{x}(k) = -\hat{B}(k, q^{-1})\hat{e}(k), \tag{5-3}$$

and a recursive least squares algorithm is used for the update laws.

The experimental results from the adaptive feedforward servo were compared with the results from the Horowitz-Li scheme. As in the previous experiments, the HDD was subjected to random external rotational disturbance. A 10-tap FIR filter was used for $\hat{Q}(q^{-1})$ in both schemes.

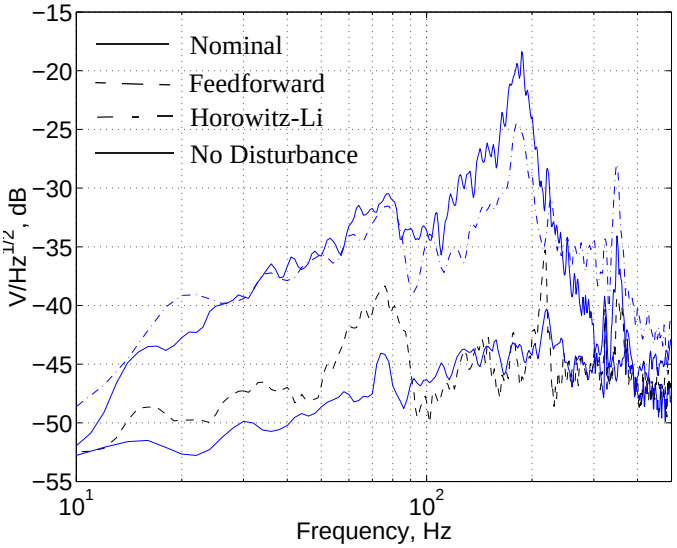

Figure 5-29. *Comparison of the power spectral density between the Horowitz-Li compensator and the adaptive feedforward servo for the random external rotational disturbance experiment.*

The power spectral density of the PES is displayed in Fig. 5-29. The upper solid line

depicts the performance of the nominal servo only, while the dashed line represents the performance of the nominal servo with the adaptive feedforward servo. The dash-dot line displays the performance of the Horowitz-Li scheme while the lower solid line represents the nominal level of the power spectral density without the disturbance. The adaptive feedforward results are the same as above. The Horowitz-Li scheme attenuated the disturbance approximately by 5 dB from 100 Hz to 200 Hz, while it amplified the disturbance above 250 Hz by 5 dB.

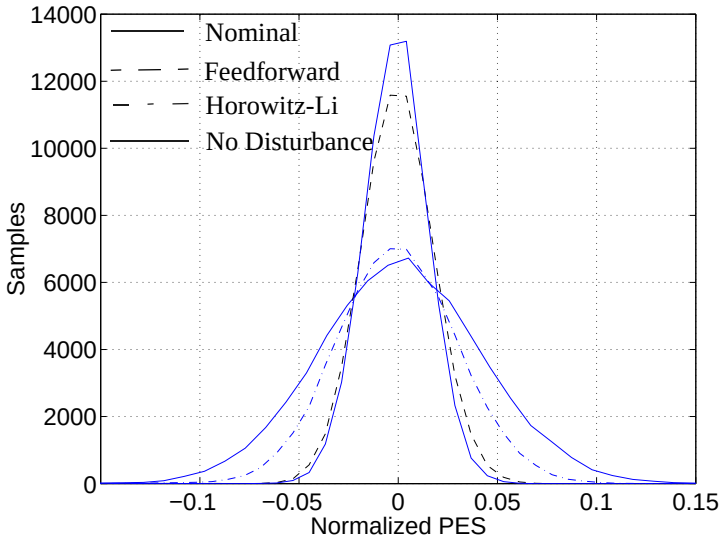

Figure 5-30. *Comparison of the histogram between the Horowitz-Li compensator and the adaptive feedforward servo for the random external rotational disturbance experiment.*

The histogram of the PES is shown in Fig. 5-30. The adaptive feedforward decreased the value from 12% to 5% which was close to the nominal level. However, the Horowitz-Li method only reduced it to 9%. The overall reduction of the variance was 89% by the adaptive feedforward and 38% by the Horowitz-Li method.

The advantage of the Horowitz-Li scheme is shown in Fig. 5-31 which shows the power spectral density of the PES for a single frequency 100 Hz rotational disturbance. The Horowitz-Li scheme not only reduced the external 100 Hz disturbances by 25 dB, but it also attenuated the nominal runout around the 100Hz disturbance by 15 dB. This extra attenuation results as a consequence of the fact that $\hat{Q}(q^{-1})$ is estimating the transfer function $A(q^{-1})/B(q^{-1})$, and the 100 Hz disturbance provides enough spectral energy to

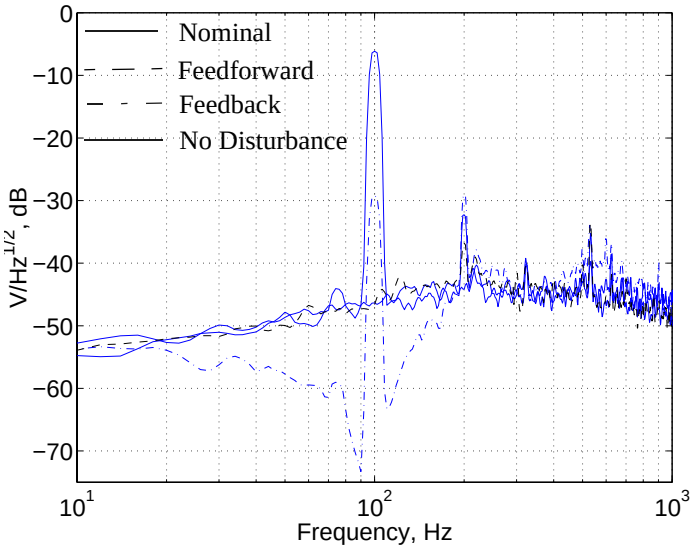

Figure 5-31. *Comparison of the power spectral density between the Horowitz-Li compensator and the adaptive feedforward servo for the 100 Hz external rotational disturbance.*

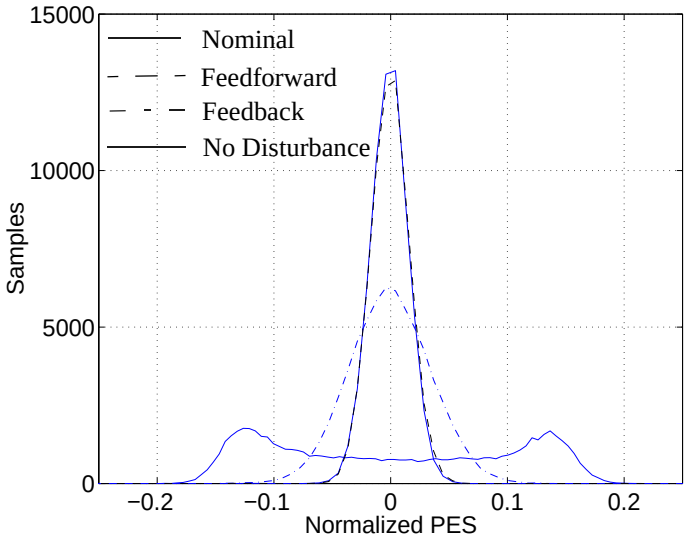

Figure 5-32. *Comparison of the histogram between the Horowitz-Li compensator and the adaptive feedforward servo for the 100 Hz external rotational disturbance experiment.*

identify $A(q^{-1})/B(q^{-1})$ in this region.

The histogram of the PES is shown in Fig. 5-32. The adaptive feedforward servo decreased the value from 17% to the nominal level of 5%. However, the Horowitz-Li

Method	Frequency	$\hat{n}_Q$	Maximum Attenuation	3σ	Reduction of Variance
Horowitz-Li	100 Hz	4	25 dB	9%	58%
Accelerometer	100 Hz	4	15 dB	5%	94%
Horowitz-Li	Random	9	5 dB	9%	38%
Accelerometer	Random	9	15 dB	5%	89%

Table 5-6. *Comparison of the results between the adaptive feedforward servo and the Horowitz-Li scheme.*

method only reduced it to 9%. The overall reduction of the variance was 94% by the adaptive feedforward and 58% by the Horowitz-Li method. A summary of the results for the comparison between algorithms are listed in Table 5-6.

5.3.2 ACCELEROMETER FEEDFORWARD USING A FILTERED-X LMS PAA

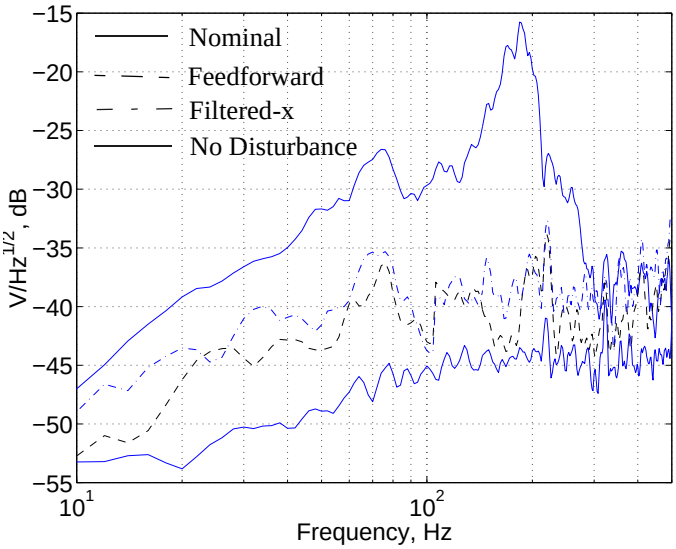

Figure 5-33. *Comparison of the power spectral density between the filtered-x scheme and the adaptive feedforward servo for the random external rotational disturbance.*

M. White and M. Tomizuka[88] also used an adaptive feedforward scheme. The control law used in their scheme was exactly the same as the one given in Eq. (4-38). However, the update law of the controller parameters for this scheme differs from the update law given by Eqs. (4-32) through (4-37). M. White and M. Tomizuka used a

multiple-tap, filtered-x LMS filter with the update law given by

$$\hat{\vec{H}}(k) = \hat{\vec{H}}(k-1) + 2\mu\hat{\vec{X}}_a(k-1)y(k-1) \; . \tag{5-4}$$

The adaptation gain μ was constant. No estimation of the disturbance, $\hat{\vec{e}}(k)$, was generated. The estimate of the disturbance was provided by the PES, $y(k)$. The estimation of the plant polynomials, $\hat{A}(q^{-1})$ and $\hat{B}(q^{-1})$, was done off-line. Hence, variation in the plant of the HDD due to thermal effects can not be compensated.

Moreover, as detailed in the stability analysis presented by Horowitz and Li in [34,56], the convergence analysis of the PAAs cannot easily be accomplished when $y(k)$ is used instead of $\hat{\vec{e}}(k)$, since by Eq. (4-6), $y(k)$ is itself affected by the control input $u(k)$ in addition to the disturbance, $\omega(k)$. Further, the convergence rate of the PAA given by Eq. (5-4) is limited since the adaptation gain is constrained to

$$0 < \mu < 1/\lambda_{max}, \tag{5-5}$$

where λ_{max} is the maximum eigenvalue of

$$\hat{R}(k) = E[\hat{X}_a(k)\hat{X}_a^{\,T}(k)] \; . \tag{5-6}$$

In fact, μ is often chosen to be a tenth of the $1/\lambda_{max}$ because of robustness issues[88]. The significant increase in the parameter convergence rate of the algorithm proposed in this dissertation over the filtered-x was verified both by simulation and experimental studies. However, the advantage of the filtered-x algorithm is that it is computationally simple. There is no plant estimation, and Eqs. (4-32) and (4-37) are not involved in the calculation of the optimal FIR filter.

The scheme presented by M. White and M. Tomizuka will be referred to as the filtered-x scheme throughout the rest of this section. A comparisons of the power spectral density of the PES for the random rotational external disturbance for both schemes is displayed in Fig. 5-33. The upper solid line depicts the performance of the nominal servo in the presence of the external disturbance, while the dashed line represents the performance of the nominal servo with the adaptive acceleration feedforward servo. The dash-dot line displays the performance of the filtered-x scheme while the lower solid line

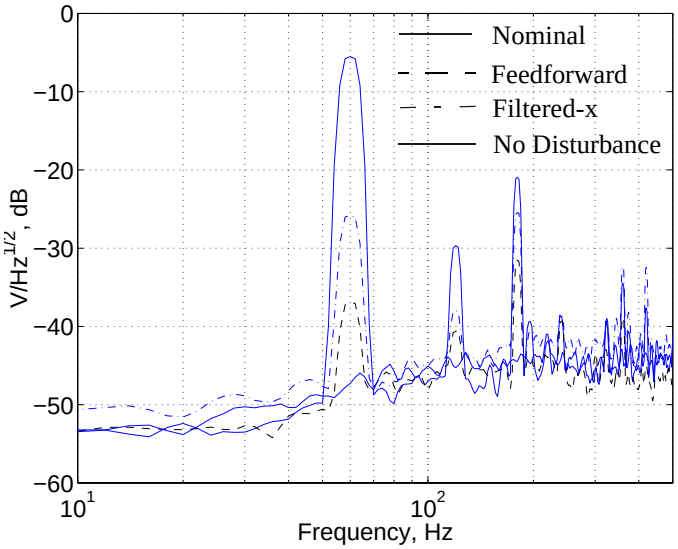

Figure 5-34. *Comparison of the power spectral density between the filtered-x scheme and the adaptive feedforward servo for the 60 Hz external rotational disturbance experiment.*

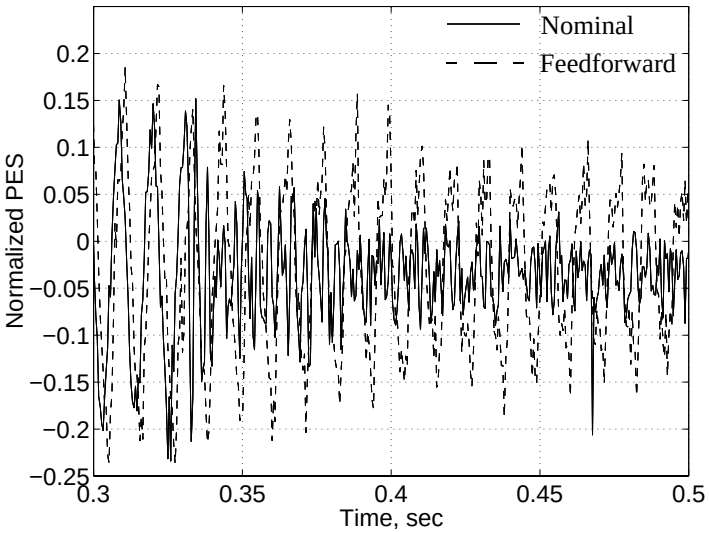

Figure 5-35. Comparison of the time response between the filtered-x scheme and the adaptive feedforward servo for the 60 Hz external rotational disturbance experiment.

represents the nominal level of the power spectral density without the disturbance. The performance of the schemes is very similar, with the adaptive feedforward servo providing an additional 3 dB of attenuation below 100 Hz.

Next, the HDD was subjected to a single frequency rotational disturbance at 60 Hz. A

5-tap FIR filter was used for $\hat{Q}(q^{-1})$ in both schemes. The power spectral density of the PES is displayed in Fig. 5-33. The dash-dot displays the performance of the filtered-x scheme while the other lines are the same as those in the previous figures. The filtered-x scheme attenuated the fundamental frequency of the disturbance by approximately 20 dB while the feedforward scheme attenuated the disturbance by 30 dB. The adaptive feedforward servo attenuated the second and third harmonics by approximately 10 dB, while the filtered-x attenuated the second and third harmonics by approximately 8 dB and 4 dB respectively.

The time response of the PES for the 60 Hz disturbance is shown in Fig. 5-35. The dash-dot line displays the performance of the filtered-x scheme while the solid line indicates the performance of the feedforward scheme. Since the gain of the filtered-x scheme was limited by Eq. (5-5), the convergence rate was generally slower than the SGA algorithm which is quite evident from Fig. 5-35. To converge to within 95% of the optimal FIR filter tap values, the feedforward and filtered-x schemes require approximately 45 msec (or 3 revolutions of the disk) and 1.17 sec (or 88 revolutions) respectively. A summary of the results for the comparison between algorithms are listed in Table 5-7.

Method	Frequency	$\hat{n}_Q$	Maximum Attenuation	Convergence Rate
Filtered-x	60 Hz	4	20 dB	1.17 sec
Accelerometer	60 Hz	4	30 dB	45 msec
Filtered-x	Random	9	15 dB	N/A
Accelerometer	Random	9	15 dB	N/A

Table 5-7. *Comparison of the results between the adaptive feedforward servo and the filtered-x scheme.*

5.4 SHOCK TESTING

The shock ratings for HDD's come in two categories: operating and nonoperating shock. Operating shock values give the maximum shock in the x-y plane that the HDD can survive without permanent damage while it is operating. Nonoperating shock gives

the maximum shock in the x-y plane that the HDD can survive without permanent damage when it is off and the disks are at rest. Commercial HDD companies typically use a half sine wave with a duration between 5 to 15 msec to approximate shocks whose peak value is stated as the shock rating. However, for operating shock, the read/write functions are typically inhibited until the effect of the shock diminishes. Delays over 50 msec can easily be induced. Shorter duration shocks can induce longer delays and cause damage at smaller magnitudes because of their broader frequency content.

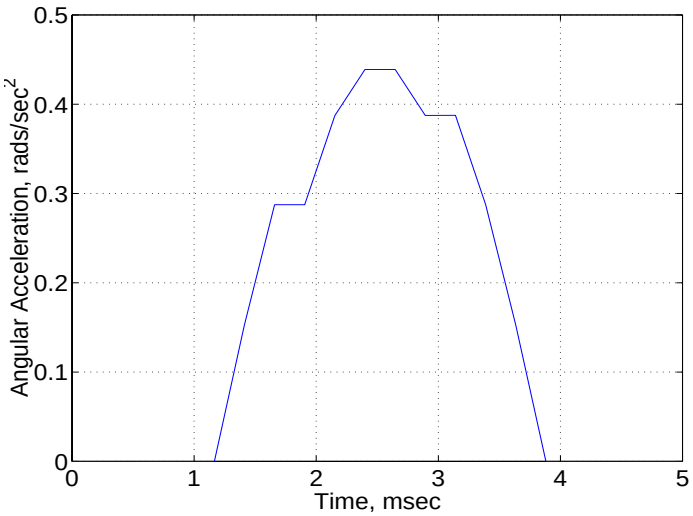

Figure 5-36. *Profile of the 2.7 msec, 4.45 rad/sec^2 rotational shock.*

Shock testing on the Seagate HDD was done using a shock profile similar to the one shown in Fig. 5-36. The shock ratings for this HDD are listed in Table 3-2. The HDD has an operating shock rating of 10 G. A 11 msec half sine wave was used for the determination of this shock rating. A shorter duration shock was used for the testing conducted in this dissertation since the shaker table is limited to a maximum linear acceleration of 4 G. Hence, to obtain a more damaging shock, a shorter duration was used. The shock does have to be of sufficient duration, however, such that the sampled accelerometer signal contains the profile of the shock. Since the sampling period of the HDD is 250 μsec, a shock of 2.7 msec in duration will provide approximately 11 samples from the accelerometer. A significant number of accelerometer samples are needed to attenuate the shock. For example, if the shock were less than 250 μsec, the sampled output of the accelerometer would not contain the shock. The profile shown in Fig. 5-36

has a peak value of 3 G which corresponds to 4.45 rad/sec^2 of rotational acceleration.

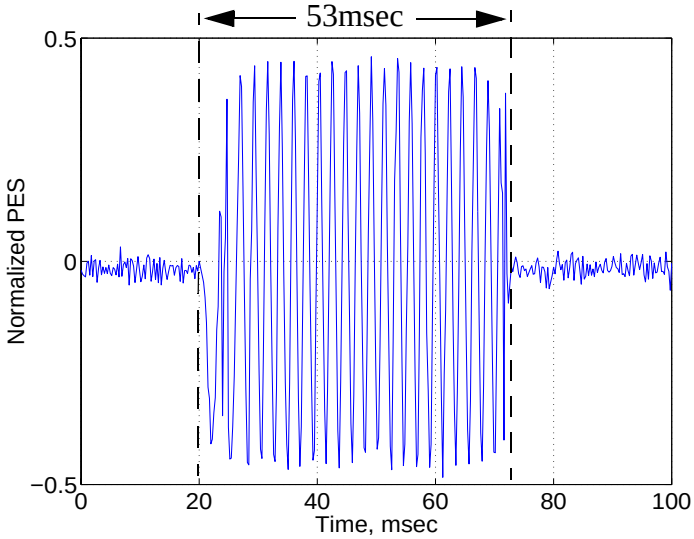

Figure 5-37. *Time response of the PES after the 4.45 rad/sec^2 rotational shock.*

The effect of the shock on the PES is displayed in Fig. 5-37. Even at this low shock level, the duration of the effect of the shock was 53 msec. During that time, the maximum tracking error was 45% of a track width which inhibits both reading and writing. In fact, after three successive shocks of this magnitude, the Seagate HDD automatically shut down to ensure data integrity.

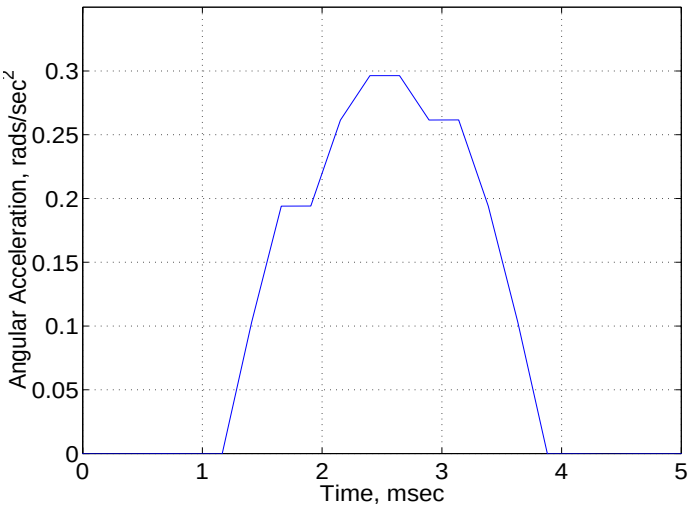

Figure 5-38. *Profile of the 2.75 msec, 3 rad/sec^2 rotational shock.*

To ensure that no damage was caused to the HDD, a shock of a lesser magnitude was

used in actual testing. The profile of this shock is shown in Fig. 5-38. It was of the same duration as the one shown is Fig. 5-36, but the magnitude is scaled to 0.675 of the original. The comparison between the time response of the PES with and without the 10-tap adaptive feedforward controller is shown in Fig. 5-39. The plots are offset for clarity. The nominal system response was offset by 75% of a track width, while the system response with the accelerometer feedfoward was offset by -75%. The adaptive feedforward servo does not do much to attenuate the first shock, since it must adapt. However, the subsequent shocks are significantly attenuated. By the ninth shock, the effect is significantly diminished.

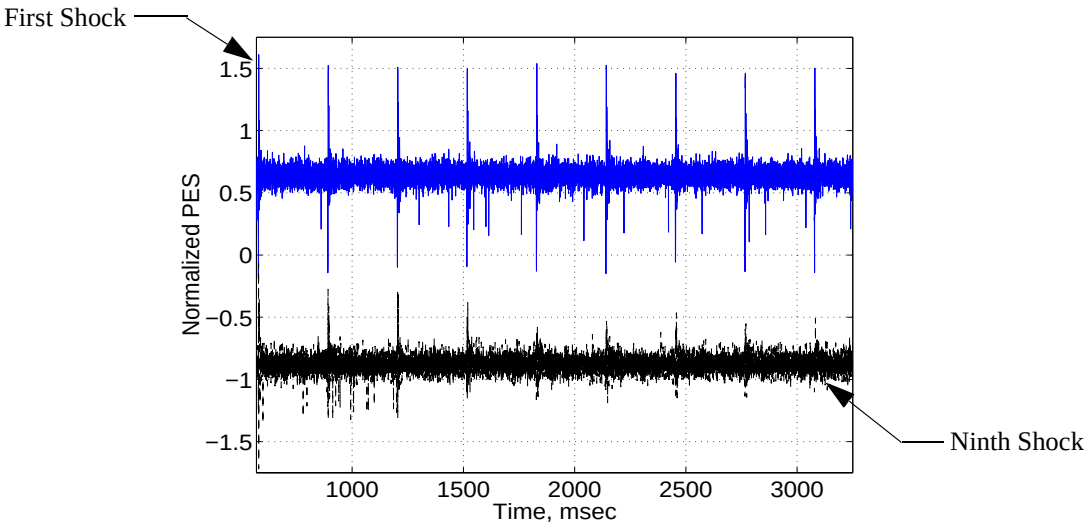

Figure 5-39. *Comparison of the time response of the PES after the 3 rad/sec^2 rotational shock. The upper and lower traces display the effect of the shock without and with the adaptive feedforward respectively.*

A close up of the second shock is shown in Fig. 5-40. The maximum magnitude of the runout was reduced from 90% to 55% of a track width, and the duration was reduced by 3msec. A close up of the ninth shock is displayed in Fig. 5-41. The tracking error has now been reduced to 25% of a track width, a 68% reduction. The duration has been reduced by 7 msec, a 54% reduction.

If the converged adaptive feedforward parameters from Section 5.2.6 are used, the performance of the stationary feedforward servo is as displayed in Fig. 5-41. The magnitude of the error is still 25% of a track width, but the duration is decreased by

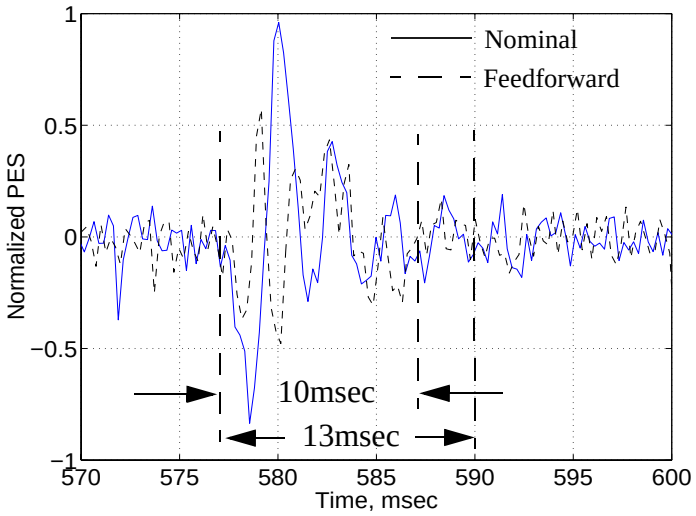

Figure 5-40. *Comparison of the time response of the PES for the second 3rad/sec^2 rotational shock.*

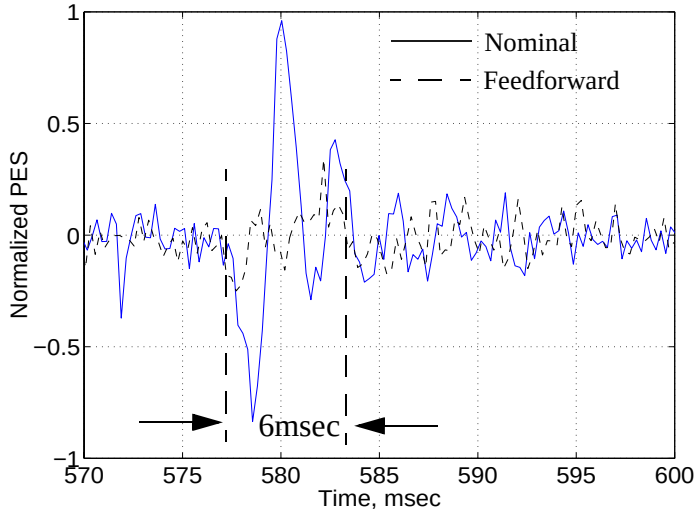

Figure 5-41. *Comparison of the time response of the PES after the 3 rad/sec^2 rotational shock during the ninth shock.*

10 msec.

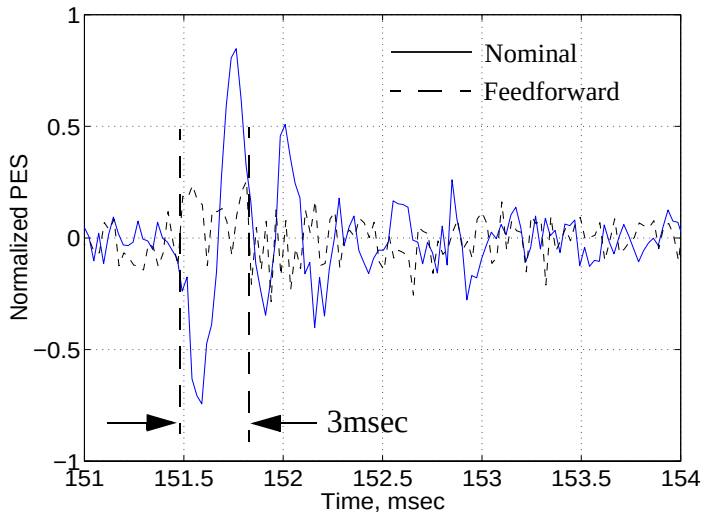

Figure 5-42. *Comparison of the time response of the PES after the 3 rad/sec^2 rotational shock using the stationary filter parameters obtained in Section 5.2.2 for the random external rotational disturbance.*

6. CONCLUSIONS

6.1 SUMMARY OF RESULTS

This dissertation presents a new direct adaptive control scheme for the track following servos of HDD's operating in the presence of external shocks and vibrations. An accelerometer signal was coupled with an adaptive scheme to minimize the variance of the position error signal. The adaptive add-on servo was implemented on a Seagate 2.5" disk drive using a TMS320C40 DSP board. An interface board was developed which allowed a number of signals to be sent between the HDD and the DSP. Among these signals were the PES and the control input to the VCM.

The HDD was subject to both single and random frequency external disturbances about several different axes. Even though the level of disturbance in all cases were quite modest (3 G), the TMR produced with only the nominal controller of the HDD was of significant magnitude to inhibit reading and writing. The accelerometer adaptive servo provided significant attenuation of the external disturbances. A summary of the results for random frequency test are given in Table 6-1. In all cases, the adaptive servo reduced the

Axis	Maximum Attenuation	3σ	Reduction of Variance
Rotational	15 dB	5%	89%
X-axis	15 dB	6%	78%
Y-axis	15 dB	6%	86%
Z-axis	15 dB	11%	58%

Table 6-1. *Summary of results for external random frequency disturbances.*

TMR to a value within 1/8 of the track width, allowing the HDD to function normally. The HDD was also subjected to single frequency disturbances to simulate the effects of RAIDs, power supply fan, and other vibrations. A summary of the results for single

frequency tests are given in Table 6-2. For all cases except the z-axis, the adaptive servo

Axis	Frequency	Maximum Attenuation	3σ	Reduction of Variance
Rotational	60 Hz	35 dB	6%	78%
X-axis	40 Hz	30 dB	6%	70%
Y-axis	250 Hz	37 dB	8%	75%
Z-axis	500 Hz	20 dB	23%	53%

Table 6-2. *Summary of results for external single frequency disturbances.*

reduced the TMR to a value within 1/8 of the track width, allowing the HDD to function normally. Overall, the accelerometer adaptive servo proved to be extremely effective in attenuating external disturbances.

The accelerometer adaptive servo was also compared to two previous disturbance rejection algorithms. The accelerometer adaptive servo outperformed the Horowitz-Li compensator. It not only provided greater attenuation of the external disturbance, it required less computational time and did not suffer from the instability problems associated with the Horowitz-Li scheme. The filtered-x scheme provided similar performance in the random frequency tests; however, in the single frequency tests, the convergence rate was shown to be an order of magnitude greater than that of the adaptive feedforward servo. Further, since the filtered-x scheme does not identify the dynamics of the HDD, it cannot compensate for thermal variations, while the adaptive feedforward servo can. A summary of the comparisons of the different servo algorithms is given Table 6-3.

Scheme	Axis	Maximum Attenuation	3σ	Reduction of Variance
Feedforward	Rotational	15 dB	5%	89%
Horowitz-Li	Rotational	5 dB	9%	28%
Filtered-x	Rotational	15 dB	6%	83%

Table 6-3. *Summary of comparisons of the difference servo algorithms.*

The HDD was also subjected to shock testing. Using the adaptive feedforward servo, the effect of a 3 rad/sec^2 rotational shock on the PES was reduced from 90% to 25% of a

track width, a 68% reduction. The duration of the effect of the shock was reduced by 7 msec, a 54% reduction. This level of attenuation was achieved after nine successive shocks.

6.2 FUTURE WORK

A number of interesting research topics still exist in this area. First, since the accelerometer signal is analog, there is little reason why it should be sensed at the sampling frequency of the PES. The only major reason would be the ease of integration into existing HDD electronics. Sensing the accelerometer signal at the PES sampling frequency would only require minor alterations in existing HDD servo code which is why that approach was pursued here. However, the changes to the servo code to sample the accelerometer at a different rate would not be too difficult. As discussed in Section 5.4, increased sampling of the accelerometer signal will allow the adaptive scheme to further attenuate external shock as well as allow the detection of shorter duration shock.

Furthermore, integrating the adaptive servo into the electronics and the DSP code of the HDD will reduce the propagation delay introduced by the interface electronics and the ‘C40 DSP described in Chapter 3. Instead of using an external DSP for the adaptive servo, the scheme can be incorporated into the existing servo scheme of HDD’s. As implemented in Chapter 5, the delay due to sampling with the ‘C40 DSP was approximately 50 μsec. Decreasing this delay to the nominal propagation delay of current HDD’s (a few μsec) would significantly increase the performance of the adaptive servo. Further, since the propagation delay can be a significant portion of the duration of the shocks, a significant improvement would be achievable in the shock attenuating performance.

Secondly, since the current scheme was limited to attenuating external disturbance about a single axis because of the use of a single axis accelerometer, a multi-axis accelerometer can be incorporated into the adaptive scheme. Thus, one accelerometer would be able to sense shock and vibration in all axes instead of mounting three separate single axis accelerometers on the base casting. A depiction of such a system is shown in

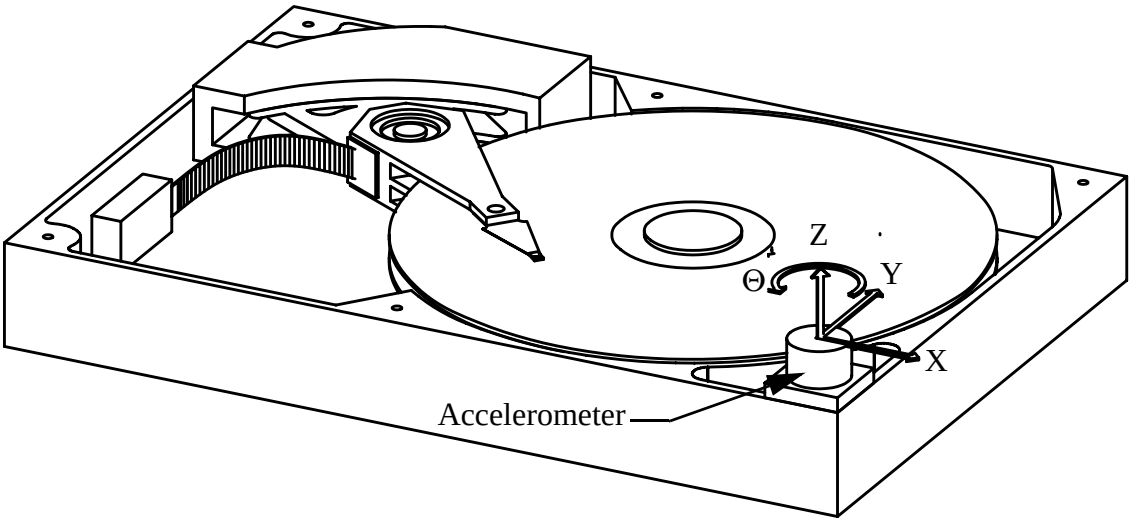

Figure 6-1. *Mounting of a multi-axis accelerometer to the HDD to allow the attenuation of external disturbances about an arbitrary axis. The accelerometer pictured is a four axis accelerometer with sense axes in the x, y, z, and θ directions.*

Fig. 6-1. Three-axis micromachined accelerometers have already been developed by BSAC[55] at the University of California at Berkeley. Since in this case there would be multiple accelerometer signals, the theorems presented in Section 4.4 would have to be extended to include MIMO systems.

Another advantage gained by developing the MIMO theory is the use of multiple accelerometers. Acceleration measurement of both the suspension and spindle axis can help attenuate internal disturbances as well as external disturbances.

Thirdly, the adaptive accelerometer scheme could be incorporated into the multiactuator control scheme currently progressing in both the academic[40] and HDD industries[18]. The attenuation of external disturbances provided by both the accelerometer adaptive feedforward scheme and the multiactuator scheme would greatly assist the HDD industry in its quest to exceed the 40 GBit/in^2 barrier.

Finally, the placement of an accelerometer on the suspension of a HDD can linearize the behavior from the VCM command to the head position. The magnitude of the transfer function from the VCM command to the head position is shown in Fig. 6-2. As stated in Section 2.2.2.1 and Section 2.2.2.5, suspension resonances and bearing effects alter the transfer function. Between 60 Hz and 1 kHz, the plant behaves as a double integrator with

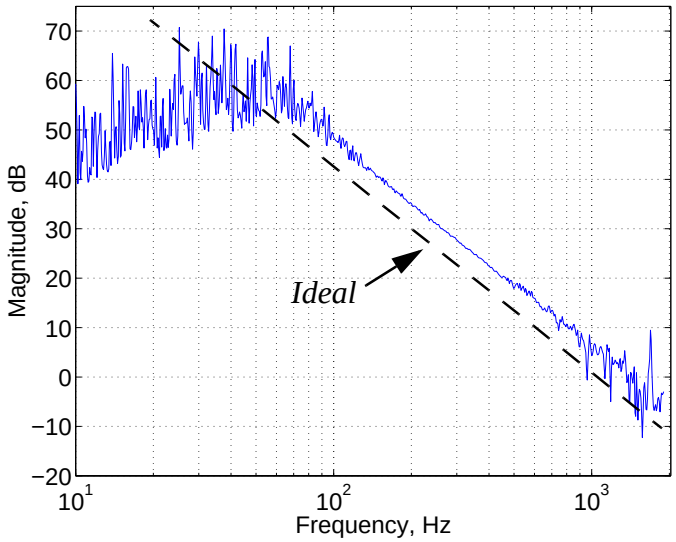

Figure 6-2. *Experimentally measure magnitude of the transfer function of the VCM command to head position of a HDD. The ideal behavior is denoted by the dashed line which is the magnitude of a double integrator transfer function.*

a one step delay due to the sampling of the PES. However, with the use of an accelerometer on the suspension, the behavior can be linearized to more closely match the idealized behavior depicted by the dashed line. The linearized system would provide much better tracking performance than the nominal system. Preliminary work on this area by Ishikawa[42] has shown promising results.

BIBLIOGRAPHY

[1] D.Y. Abramovitch. Rejection of disturbances on a disk drive by use of an accelerometer. United States Patent 5,553,847. Hewlett-Packard Company. Palo Alto, CA, 1997.

[2] D.Y. Abramovitch. Rejecting rotational disturbances on small disk drives using rotational accelerometers. In *Proceedings of the 13th World Congress of IFAC*, volume O, pages 483-488, San Francisco, July 1996.

[3] D.Y. Abramovitch, T. Hurst, and D. Henze. An overview of the PES Pareto Method for decomposing baseline noise sources in hard disk position error signals. *IEEE Transactions on Magnetics*. 34(1):17-23, January 1998.

[4] D.Y. Abramovitch, F. Wang, and G. Franklin. Disk drive pivot nonlinearity modeling part I: frequency domain. In *Proceedings of the American Control Conference*, volume 3, pages 2600-2603, Seattle, June 1994.

[5] A.M. Allen and D.B. Bogy. Effects of shock on the head-disk interface. *IEEE Transactions on Magnetics*. 32(5):3717-3719, September 1996.

[6] Analog Devices, Inc. *ADXL05 Single Chip Accelerometer with Signal Conditioning*. Techinical Specifications, 1996.

[7] K.J. Astrom and B. Wittenmark. *Adaptive Control*. Addison-Wesley, Menlo Park, Ca, 1995.

[8] K. Aruga, Y. Mizoshita, M. Iwatsubo, and T. Hatagami. Acceleration feedforward control for head positioning in magnetic disk drives. *JSME International Journal*, 33(1):35-41, 1990. series III.

[9] K. Aruga, S. Yoneoka, and T. Ohwe. Vibro-loading of magnetic head assemblies for hard disk drives. *IEEE Transactions on Magnetics*. 30(6):4161-4163, November 1994.

[10] H. F. Chen and L. Guo. *Identification and Stochastic Adaptive Control*. Birkhauser, Boston, Ma, 1991.

[11] K.K. Chew. Control system challenges to high track density magnetic disk storage. *IEEE Transactions on Magnetics*. 32(3):1799-1804, May 1996.

[12] K.K. Chew and M. Tomizuka. Digital control of repetitive errors in disk drive systems. In *Proceedings of the 29th IEEE Conference on Decision and Control*, pages 1902-1907, Honolulu, HI, December 1990.

[13] C. D'Angelo III and C.D. Mote, Jr. Aerodynamically excited vibration and flutter of a thin disk rotating at supercritical speed. *Journal of Sound and Vibration*, 168(1): 15-30, November 1993.

[14] C. D'Angelo III and C.D. Mote, Jr. Natural Frequencies of a Thin Disk Clamped by Thick Collars with Friction at the Contacting Surfaces Spinning at High Rotation Speed. *Journal of Sound and Vibration*, 168(1): 1-14, November 1993.

[15] D.B. Davies and M.D. Sidman. Active compensation of shock, vibration, and wind-up in disk drives. In *Advances in Information Storage Systems*, volume 5, pages 5-20. ASME Press, 1993. B. Bhushan, editor.

[16] K. Eddy and W. Messner. Dynamics affecting tracking bias in hard disk drive rotary actuators. In *Proceedings of the American Control Conference*, volume 6, pages 1055-1060, Seattle, June 1995.

[17] S.J. Elliott, I.M. Stothers, and P.A. Nelson. A multiple error LMS algorithm and its application to the active control of sound and vibration. *IEEE Transactions on Acoustics, Speech, and Signal Processing*, ASSP-35(10):1423-1434, October 1987.

[18] L.-S. Fan. Design and fabrication of microactuators for high density data storage. *IEEE Transaction on Magnetics*. 32(3):1855-1862, May 1996.

[19] L.-S. Fan, H.H. Ottesen, T.C. Reiley, and R.W. Wood. Magnetic recording head positioning at very high track densities using a microactuator-based, two-stage servo system. *IEEE Transactions on Industrial Electronics*. 42(3):222-233, June 1995.

[20] S. Finch. Information Technology - AT Attachment Interface with Extensions. American National Standard Institute, 1995.

[21] S. Finch and D. Maczarny. Headerless disk formatting: Making room for more data. *Data Storage Magazine*. pages 52-54, April 1997.

[22] G.F. Franklin, J.D. Powell, and M.L. Workman. *Digital Control of Dynamic Systems*. Addison-Wesley, Menlo Park, CA, 2nd edition, 1992.

[23] G. Frees. Disk drive spindle dynamics - analysis and measurement. In *Advances in Information Storage Systems*, volume 6. ASME Press, 1994. B. Bhushan, editor.

[24] T. Fu and D.B. Bogy. Drive level slider-suspension vibration analysis and its application to a ramp-load magnetic disk drive. *IEEE Transactions on Magnetics*. 31(6):3003-3005, November 1995.

[25] C.R. Fuller and A.H. von Flotow. Active control of sounds and vibration. *IEEE Control Systems*, pages 9-19, December 1995.

[26] H.T. Goh, S. Weerasooriya, T.S. Low, and Y.H. Huang. Modeling and Compensation of Pivot Friction in a Disk Drive Actuator. In *Proceedings of the American Control Conference*, volume 6, pages 4141-4145, Seattle, June 1995.

[27] G.C. Goodwin and K.S. Sin. *Adaptive Filtering Prediction and Control*. Prentice Hall, Englewood Cliffs, NJ, 1984.

[28] E. Grochowski and R.F. Hoyt. Future trends in hard disk drives. *IEEE Transaction on Magnetics*. 32(3):1850-1854, May 1996.

[29] J. Gui, D. Kuo, B. Marchon, and G.C. Rauch. Stiction model for a head-disk interface: experimental. *IEEE Transaction on Magnetics*. 33(1):932-937, January 1997.

[30] S.D. Haddad and M. Lalouette. A new mounting adapter for computer peripherals with improved reliability, thermal distribution, low noise and vibration reduction. In *Advances in Information Storage and Processing Systems, Proceedings of the ASME IMECE*, pages 97-100, San Francisco, November 1995.

[31] D.M. Hanks. Apparatus and method for shock attenuation in a disk recording and/or reproduction system using variable gain acceleration sensor. United States Patent 5,299,075. Hewlett-Packard Company. Palo Alto, CA, 1994.

[32] J.C. Harrison and F.E. Talke. Non-repeatable runout of cantilever and doubly supported 51/4" disc drive spindles. *Precision Engineering*, 13(10:33-40, January 1991.

[33] S. Haykin. *Adaptive Filter Theory.* Prentice Hall, Englewood Cliffs, NJ, 1991.

[34] R. Horowitz, B. Li, and J. McCormick. Wiener filter based minimum variance self-tuning regulation. In *Automatica*, 43(2), February 1998.

[35] R. Horowitz and B. Li. Adaptive track-following servos for disk file actuators. *IEEE Transactions on Magnetics*, 32(3):1779-1786, May 1996.

[36] R. Horowitz and B. Li. Adaptive control for disk file actuators. In *Proceedings of the 34th IEEE Conference on Decision and Control*, volume 1, pages 655-660, New Orleans, LA, December 1995.

[37] R. Horowitz and B. Li. Design and implementation of adaptive non-repetitive track-following disk file servos. In *Proceedings of the American Control Conference*, volume 6, pages 4151-4155, Seattle WA, June 1995.

[38] R. Horowitz and J. McCormick. A self-tuning control scheme for disk file servos. *IEEE Transactions on Magnetics*, 27(6):4490-4495, November 1991.

[39] D.A. Horsley, A. Singh, A.P. Pisano, and R. Horowitz. Angular micropositioner for disk drives. In The 10th Annual International Workshop on Mirco Electro Mechanical Systems, pages 454-459, Nagoya, Japan, January 1997.

[40] D.A. Horsley. *A Mircofabricated Electrostatic Actuator for Magnetic Disk Drives.* PhD thesis, University of California, Berkeley, 1998.

[41] Hutchinson Technology Inc. *Microactuation test platform*. Technology Bulliten, September 1997.

[42] J. Ishikawa and M. Tomizuka. Pivot friction compensation using an accelerometer and a disturbance observer for hard disk drives. In *Advances in Information Storage and Processing System, Proceedings of the ASME IMECE,* volume 3, Dallas TX, November 1997.

[43] M. Johnson. *PC Programmer's Guide to Low-Leverl Functions and Interrupts.* SAM Publishing, Indianapolis, Indiana, 1994.

[44] F. Jorgensen. The complete handbook of magnetic recording. McGraw-Hill, New York, New York, 1996.

[45] R.S. Kajley, J.E.C. Brown, and P.J. Hurst. A mixed-signal decision-feedback equalizer that uses parallelism. In *Proceedings of the IEEE 1996 Custom Integrated Circuits Conference*, pages 17-20, San Diego, CA, May 1996.

[46] C.J. Kempf. *Design of Servo Systems for Disturbance Rejection and Applications to Disk File Storage Systems*. PhD thesis, University of California, Berkeley, 1994.

[47] M. Kobayahi, T. Yamaguchi, H. Hirai, K. Tsuneta, T. Arai, and K. Onoyama. Adaptive control of a hybrid servo system for magnetic disk drives. JSME International Journal, Series C. 39(4):772-80, December 1996.

[48] T. Kouhei, T. Yamada, Y. Kuroba, and K. Aruga. A study of head-disk interface shock resistance. *IEEE Transactions on Magnetics*. 31(6):3006-3008, November 1995.

[49] C.-P. Ku. Dynamic characteristics of hard disk drive spindle motors-comparison between ball bearings and hydrodynamic bearings. *Transactions of the ASME. Journal of Tribology*, 118(2):402-406, April 1996.

[50] S. Kumar, V.D. Khanna, and M. Sri-Jayantha. A study of head disk interface shock failure mechanism. *IEEE Transactions on Magnetics*. 30(6):4155-4157, November 1994.

[51] Lattice Semiconductor Corporation. *Lattice Semiconductor Data Book.* Hillsboro, Oregon, 1996.

[52] C. Lee, A.C. Munce, and T.C. O'Sullivan. Disk drive with acceleration rate sensing. United States Patent 5,521,772. IBM Corporation. Armonk, NY, 1996.

[53] H.S. Lee. Implementation of adaptive feedforward cancellation algorithms for pre-embossed rigid magnetic (PERM) disks. IEEE Transactions on Magnetics. 33(3):2419-2423, May 1997.

[54] H.S. Lee and H. Ferrier. Open-loop compensation of repeatable runouts in discrete-track magnetic disks. In Advances in Information Storage and Processing Systems, Proceedings of the American Control Conference, volume 1, pages 215-219, Seattle, June 1995.

[55] M. Lemkin. *Micro Accelerometer Design with Digital Feedback Control*. PhD thesis, University of California, Berkeley, 1997.

[56] B. Li. *Wiener Filter Based Adaptive Control with Applications to the Design of Disk File Servos*. PhD thesis, University of California, Berkeley, 1995.

[57] B. Liu, S.B. Hu, T.S. Low, S.H. Soh, and J. Yip. Skew angle and its effect on gb/in^2 density magnetic recording. *IEEE Transactions on Magnetics*, 32(3):1743-1748, May 1996.

[58] L. Ljung. *System Identification: Theory for the User.* Prentice-Hall, Englewood Cliffs, NJ, 1987.

[59] L. Ljung and T. Soderstrom. *Theory and Practice of Recursive Identification*. MIT Press, Cambridge, MA, 1983.

[60] J.S. McAllister. Characterization of Disk Vibrations on Aluminum and Alternate Substrates. *IEEE Transactions on Magnetics.* 33(1):968-973, January 1997

[61] J.S. McAllister. The effect of disk platter resonances on track misregistration in 3.5 inch disk drives. *IEEE Transactions on Magnetics*. 32(3):1762-1766, May 1996.

[62] W. Messner and K. Eddy. Disk drive actuator bias: prediction and compensation. In *Proceedings of the 13th World Congress of IFAC,* volume O, pages 477-482, San Francisco, July 1996.

[63] W. Messner and C. Kempf. A comparison of four discrete-time repetitive control algorithm. Technical report, University of California, Berkeley, Mechanical Engineering Department, Computer Mechanics Laboratory, December 1991.

[64] D.K. Miu, G.M. Frees, and R.S. Gompertz. Tracking dynamics of read/write head suspensions in high performance small form factor rigid disk drives. *ASME Journal of Vibration and Acoustics*, 112:33-39, January 1990.

[65] Y. Mizoshita, S. Hasegawa, and K. Takaishi. Vibration minimized access control for disk drives. *IEEE Transactions on Magnetics*. 32(3):1793-1798, May 1996.

[66] T. Ohmi. Non-repeatable runout of ball-bearing spindle-motor for 2.5” HDD. *IEEE Transactions on Magnetics*. 32(3):1715-1720, May 1996.

[67] R.G. Parker and C.D. Mote, Jr. Vibration and coupling phenomena in asymmetric disk-spindle systems. In *Advances in Information Storage and Processing Systems, Proceedings of the ASME IMECE*, pages 293-302, San Francisco, CA, November 1995.

[68] D.T. Phan. The design and modeling of multirate digital control systems for disk drives applications. In *Proceedings of the 1993 Asia-Pacific Workshop on Advances in Motion Control*, pages 189-205. Singapore, July 1993.

[69] H.R. Radwan, D.T. Phan and Kiet Cao. Effect of disk drive actuator unbalance on track following response to external vibration & shock. *IEEE Transactions on Magnetics*. 32(3):1749-1755, May 1996.

[70] H.R. Radwan and R. Whaley. Servo-structure interaction in disk drives using finite element analysis. In *Advances in Information Storage Systems*, volume 5, pages 101-118. ASME Press, 1993. B. Bhushan, editor.

[71] T.C. Reiley, T.R. Albrecht, M.A. Moser, O. Ruiz, and S. Pattanaik. MICROFILE--A one-inch disk drive technology demonstration. In *Proceedings of the 6th Biennial IEEE International Nonvolatile Memory Technology Conference*, pages 17-20. Albuquerque, Mn, June 1996.

[72] W. Ren and P.R. Kumar. Adaptive active noise control: Structures, algorithms and convergence analysis. In *Proceedings of the 1989 International Conference on Noise Control Engineering*, volume 1, pages 435-440, Newport Beach, CA, December 1989. G.C. Maling, Jr., editor.

[73] A. Renshaw, C. D'Angelo III, and C.D. Mote, Jr. Aerodynamically excited vibration of a rotating disk. *Journal of Sound and Vibration*, 177(5):577-590, November 1994.

[74] W.O. Richter and F.E. Talke. Nonrepeatable radial and axial runout of 51/4" disk drive spindles. *IEEE Transactions on Magnetics*, 24(6):2760-2762, November 1988.

[75] A.H. Sacks and W. Messner. MR head effects on PES generation: simulation and experiment. *IEEE Transactions on Magnetics*, 32(3):1773-1778, May 1996.

[76] A.H. Sacks, M. Bodson, and W. Messner. Advanced methods for repeatable runout compensation. *IEEE Transactions on Magnetics*, 31(2):1031-1036, March 1995.

[77] A.C. Swann, J.C. Harrison, and F.E. Talke. Non-repeatable runout measurement and simulation of fluid lubricated spindles. *IEEE Transactions on Magnetics*. 32(3):1727-1732, May 1996.

[78] N. Schirle and D.K. Lieu. History and trends in the development of motorized spindles for hard disk drives. *IEEE Transactions on Magnetics*, 32(3):1703-1708, May 1996.

[79] I.Y. Shen and C.P. Roger Ku. On the rocking motion of a rotating flexible-disk/rigid shaft system. In *Advances in Information Storage and Processing Systems, Proceedings of the ASME IMECE*, pages 271-282, San Francisco, November 1995.

[80] I.Y. Shen and C.P. Roger Ku. On the vibration analysis of multiple rotating flexible disks. In *Advances in Information Storage and Processing Systems, Proceedings of the ASME IMECE*, pages 259-270, San Francisco, November 1995.

[81] M.D. Sidman and D.B. Davies. Active disturbance compensation system for disk drives. United States Patent 5,426,545. Colorado Springs, CO, 1995.

[82] M.D. Sidman. Convergence properties of an adaptive runout correction systems for disk drives. In *Advances in Information Storage Systems*, volume 1, pages 61-78. ASME Press, New York, 1991. B. Bhushan, editor.

[83] M.D. Sidman. *Analysis of Active Compensation for Shock, Vibration, and Wind-up in Disk Drives*. Masters thesis, M.I.T., 1991.

[84] M. Tomizuka. Zero-phase error tracking controller for digital control. *ASME Journal of Dynamic Systems, Measurement and Control*, 109:65-68, 1987.

[85] F. Wang, T. Hurst, D.Y. Abramovitch, and G. Franklin. Disk drive pivot nonlinearity modeling part II: time domain. In *Proceedings of the American Control Conference*, volume 3, pages 2604-2607, Seattle, June 1994.

[86] P.A. Weaver and R.M. Ehrlich. The use of multirate notch filters in embedded-servo disk drives. In *Proceedings of the American Control Conference*, volume 6, pages 4156-4160, Seattle, June 1995.

[87] S. Weerasooriya, J.L. Zhang, and T.S. Low. Efficient implementation of adaptive feedforward runout cancellation in a disk drive. *IEEE Transaction on Magnetics*. 32(5):3920-3922, September 1996.

[88] M.T. White. *Control Techniques for Increased Disturbance Rejection and Tracking Accuracy in Magnetic Disk Drives*. PhD thesis, University of California, Berkeley, 1997

[89] M.T. White and M. Tomizuka. Increased disturbance rejection in magnetic disk drives by acceleration feedforward control. In *Proceedings of the 13th World Congress of IFAC*, volume O, pages 489-494, San Francisco, July 1996.

[90] R.A. White. Shock force compensating system. United States Patent 4,040,103. Sperry Rand Corporation. New York, New York, 1977.

[91] R.L. White, R.M.H. New, and R.F.W. Pease. Patterned media: A viable route to 50 gbits/in^2 and up for magnetic recording. *IEEE Transaction on Magnetics*. 33(1):990-995, January 1997.

[92] B. Widrow, J.M. McCool, M.G. Larimore, and C.R. Johnson, Jr. Stationary and nonstationary learning characteristics of the LMS adaptive filter. *Proceedings of the IEEE*. 64(8):1151-1162, August 1976.

[93] B. Widrow and S.D. Stearns. *Adaptive Signal Processing*. Prentice Hall, Englewood Cliffs, NJ, 1985.

[94] T. Yamaguchi, Y. Soyama, H. Hosokawa, K. Tsuneta, and H. Hirai. Improvement of settling response of disk drive head position servo using mode switching control with initial value compensation. *IEEE Transactions on Magnetics*, 32(3):1767-1772, May 1996.

[95] T. Yamaguchi, Y. Soyama, H. Hosokawa, K. Tsuneta, and H. Hirai. Mode switching control design and its application to head position control on magnetic disk drives. *IEEE Transactions on Industrial Electronics*, 43(1):65-73, February 1996.

APPENDIX A - CONVERGENCE ANALYSIS

The convergence proofs presented in this section follow the proofs presented in [34]. As discussed in Chapter 4, the adaptive scheme presented there used an accelerometer to generate the control signal. The scheme presented by R. Horowtiz and B. Li in [34] did not use an external sensor. The proofs have been altered to account for this difference. Further, the feedback scheme in [34] uses the RLS for the adaptation mechanisms where the SGA is used here. The two theorems presented in Section 4.4 will be proven below.

A1. Proof of Theorem 1

Both a lemma and a corollary which are instrumental in the proof of Theorem 1 are stated below. The lemma is known as the Stochastic Key Technical Lemma and is from Goodwin and Sin[27]. It has been numbered the same as in [27]. The notation has been modified to match the notation given in this dissertation.

Lemma 8.5.3. The Stochastic Key Technical Lemma.

If $\lim_{N \to \infty} \sum_{k=0}^{N} \frac{(\hat{e}_\theta(k) - \omega(k))^2}{F_\theta(k-1)} < \infty$ *holds and if there exists constants* K_1, K_2, *and* $\bar{N}$, $[0 \le K_1 < \infty, 0 < K_2 < \infty, 0 < \bar{N} < \infty]$ *such that:*

$$\frac{1}{N} F_\theta(N-1) \le K_1 + \frac{K_2}{N} \sum_{k=1}^{N} [\hat{e}_\theta(k) - \omega(k)]^2, N \ge \bar{N} \qquad \text{(L8.5.3-1)}$$

then

$$\lim_{N \to \infty} \frac{1}{N} \sum_{k=1}^{N} [\hat{e}_\theta(k) - \omega(k)]^2 = 0, \text{ a.s.} \qquad \text{(L8.5.3-2)}$$

$$\lim_{N \to \infty} sup \frac{1}{N} F_\theta(N-1) \le \infty, \text{ a.s.} \qquad \text{(L8.5.3-3)}$$

$$\lim_{N\to\infty}\frac{1}{N}\sum_{k=1}^{N} E_{k-1}[y(k)-\hat{y}(k)]^2 = \sigma^2, \text{ a.s.} \qquad \text{(L8.5.3-4)}$$

Proof of (Lemma 8.5.3.):

This lemma is proven in [27].

The corollary which states convergence results using positive super martingale functions is stated below. It has been numbered the same as found in [27]. The notation has been modified to match the notation used in this dissertation.

Corollary D.5.1. *If* $\{V(t,\omega)\}$ *is a sequence of nonnegative random variables adapted to an increasing sequence of sub-sigma algebras* $\underset{t}{}$ *and if* $E_k[V(k)] \le V(k-1) - \alpha_j + \gamma_j$ *where* $\alpha_j \ge 0, \gamma_j \ge 0 \quad \forall j$, $\sum_{i=0}^{N} \gamma_j < \infty$, *and* $E[V(0)] \le \infty$ *then* $V(t)$ *converges almost surely to a finite random variable and* $\lim_{N\to\infty}\sum_{i=0} \alpha_j < \infty$ *a.s.*

Proof of (Corollary D.5.1.):

This corollary is proven by Goodwin and Sin in [27].

A few preliminary properties which will be needed to prove Theorem 1 will be summarized in Lemma 1 and Lemma 2 below.

Lemma 1. *Consider the Pseudo Linear Regression (PLR) algorithm given by Eq. (4-29) -Eq. (4-31). Under the assumptions that* $\omega(k)$ *is a zero mean innovation signal with bounded covariance, the PLR has the following properties:*

$$\lim_{N\to\infty}\sum_{k=1}^{N}\frac{\phi^T(k-1)\phi(k-1)}{F_\theta(k-1)F_\theta(k-2)} < \infty, \qquad \text{(L1-1)}$$

$$C(q^{-1})\hat{\eta}(k) = \hat{b}(k), \qquad \text{(L1-2)}$$

$$E_k[\hat{b}(k)\omega(k)] = 0, \qquad \text{(L1-3)}$$

where $\hat{\eta}(k) = \hat{e}_\theta(k) - \omega(k)$, $\hat{b}(k) = -\phi^T(k-1)\tilde{\theta}(k-1)$, *and* $\tilde{\theta}(k) = \hat{\theta}(k) - \theta_o$.

Proof of Eq. (L1-1):

Starting with Eq. (4-31),

$$\frac{F_\theta(k-1)-F_\theta(k-2)}{\lambda_\theta} = \phi^T(k-1)\phi(k-1)\,. \tag{A1-1}$$

Substituting Eq. (A1-1) into the left hand side of Eq. (L1-1) yields

$$\lim_{N\to\infty}\frac{1}{\lambda_\theta}\sum_{k=1}^{N}\frac{F_\theta(k-1)-F_\theta(k-2)}{F_\theta(k-1)F_\theta(k-2)}, \tag{A1-2}$$

which implies that

$$\lim_{N\to\infty}\frac{1}{\lambda_\theta}\sum_{k=1}^{N}\left[\frac{1}{F_\theta(k-2)}-\frac{1}{F_\theta(k-1)}\right]\le\frac{1}{\lambda_\theta F_\theta(-1)}<\infty\,, \tag{A1-3}$$

since $F_\theta(-1)$ is the initial adaptation gain which is finite and λ_θ is bounded by definition. Therefore

$$\lim_{N\to\infty}\sum_{k=1}^{N}\frac{\phi^T(k-1)\phi(k-1)}{F_\theta(k-1)F_\theta(k-2)}<\infty\,. \tag{A1-4}$$

Further, since

$$F_\theta(k-1)\ge F_\theta(k-2),\ \forall k\ , \tag{A1-5}$$

the following relation can be obtained

$$\frac{\phi^T(k-1)\phi(k-1)}{F_\theta(k-1)F_\theta(k-1)}\le\frac{\phi^T(k-1)\phi(k-1)}{F_\theta(k-1)F_\theta(k-2)},\ \forall k\ , \tag{A1-6}$$

which in turn implies that

$$\lim_{N\to\infty}\sum_{k=1}^{N}\frac{\phi^T(k-1)\phi(k-1)}{F_\theta(k-1)F_\theta(k-1)}<\infty\,. \tag{A1-7}$$

Proof of Eq. (L1-2):

Adding and subtracting $[0\ 0\ldots\hat{e}_\theta(k-1)]\theta_o$ from the right hand side of Eq. (4-31)

yields

$$\hat{e}_\theta(k) = \psi^T(k-1)\theta_o - \phi^T(k-1)\hat{\theta}(k-1) + [0\ 0 \ldots \hat{e}_\theta(k-1)](\theta_o - \theta_o) + \omega(k)\ , \quad \text{(A1-8)}$$

$$\hat{e}_\theta(k) = -\phi^T(k-1)\tilde{\theta}(k-1) + C^*(q^{-1})(\omega(k-1) - \hat{e}_\theta(k-1)) + \omega(k), \quad \text{(A1-9)}$$

where $C^*(q^{-1}) = c_1 q^{-1} + \ldots + c_{n_C} q^{-n_C}$.

Moving the last two terms on the right hand side of Eq. (A1-9) to the left hand side yields

$$\begin{aligned} C(q^{-1})(\hat{e}_\theta(k) - \omega(k)) &= -\phi^T(k-1)\tilde{\theta}(k-1), \\ C(q^{-1})\hat{\eta}(k) &= \hat{b}(k). \end{aligned} \quad \text{(A1-10)}$$

Proof of Eq. (L1-3):

Expanding the left side of Eq. (L1-3)

$$E_k[\hat{b}(k)\omega(k)] = E_k[C(q^{-1})(\hat{e}_\theta(k) - \omega(k))\omega(k)]\ . \quad \text{(A1-11)}$$

Since $\omega(k)$ is random white noise, and E_k is the expectation operator with all the $k-1$ terms assumed to be known

$$\begin{aligned} E_k[C(q^{-1})(\hat{e}_\theta(k) - \omega(k))\omega(k)] &= 0, \\ E_k[\hat{b}(k)\omega(k)] &= 0. \end{aligned} \quad \text{(A1-12)}$$

In order to used the Stochastic Key Technical Lemma, it is necessary to prove that there exists positive bounded constants, K_1, K_2, and N such that for any $N \geq N$, the inequality Eq. (L8.5.3-1) holds.

Lemma 2. Consider the ARMAX representation of the regulated variable closed loop dynamics given by Eq. (4-6), with the auxiliary control action given by Eq. (4-38). Under the conditions given in Theorem 1, the following inequalities hold:

$$\frac{1}{N}\sum_{k=1}^{N} \hat{e}_\theta(k) \leq C_1 + \frac{C_2}{N}\sum_{k=1}^{N} [\hat{e}_\theta(k) - \omega(k)]^2, 0 \leq C_1, C_2 < \infty\ , \quad \text{(L2-1)}$$

$$\frac{1}{N}\sum_{k=1}^{N} u^2(k) \le C_3 + \frac{C_4}{N}\sum_{k=1}^{N} [\hat{e}_\theta(k) - \omega(k)]^2, 0 \le C_3, C_4 < \infty , \quad \text{(L2-2)}$$

$$\frac{1}{N}\sum_{k=1}^{N} y^2(k) \le C_5 + \frac{C_6}{N}\sum_{k=1}^{N} [\hat{e}_\theta(k) - \omega(k)]^2, 0 \le C_5, C_6 < \infty , \quad \text{(L2-3)}$$

$$\frac{1}{N}F_\theta(N-1) \le K_1 + \frac{K_2}{N}\sum_{k=1}^{N} [\hat{e}_\theta(k) - \omega(k)]^2, N \ge \bar{N} . \quad \text{(L2-4)}$$

Proof of Eq. (L2-1):

Starting with the equality $\hat{e}_\theta(k) = \hat{e}_\theta(k)$ and adding and subtracting $\omega(k)$ from the right hand side yields

$$\hat{e}_\theta(k) = \hat{e}_\theta(k) - \omega(k) + \omega(k) . \quad \text{(A1-13)}$$

Squaring both sides

$$\hat{e}_\theta^2(k) = (\hat{e}_\theta(k) - \omega(k))^2 + 2(\hat{e}_\theta(k) - \omega(k))\omega(k) + \omega^2(k) , \quad \text{(A1-14)}$$

and using the fact that

$$2(\hat{e}_\theta(k) - \omega(k))\omega(k) \le (\hat{e}_\theta(k) - \omega(k))^2 + \omega^2(k) , \quad \text{(A1-15)}$$

implies that

$$\hat{e}_\theta^2(k) \le 2(\hat{e}_\theta(k) - \omega(k))^2 + 2\omega^2(k), \forall k . \quad \text{(A1-16)}$$

Hence summing from 1 to N and dividing by N implies that

$$\frac{1}{N}\sum_{k=1}^{N} \hat{e}_\theta^2(k) \le \frac{2}{N}\sum_{k=1}^{N} (\hat{e}_\theta(k) - \omega(k))^2 + \frac{2}{N}\sum_{k=1}^{N} \omega^2(k) . \quad \text{(A1-17)}$$

Since one of the system assumptions is that the variance of the noise is bounded

$$\frac{2}{N}\sum_{k=1}^{N} \omega^2(k) = C_1 < \infty , \quad \text{(A1-18)}$$

inequality (L2-1) is obtained.

Proof of Eq. (L2-2):

From Eq. (4-37)and Eq. (4-38),

$$u(k) \;=\; \hat{h}_o a(k) + \hat{h}_1 a(k-1) + \ldots + \hat{h}_{n_Q} a(k-n_Q)\,. \tag{A1-19}$$

Since the taps of $u(k)$ are assumed to be bounded by h_{max},

$$u^2(k) \le n_Q h^2{}_{max}(a^2(k) + a^2(k-1) + \ldots + a^2(k-n_Q))\,. \tag{A1-20}$$

Using the assumption that the white noise, $\omega(k)$, has finite power and the accelerometer signal as given by Eq. (4-9) is just a filtered version of $\omega(k)$ yields the following relation

$$\frac{1}{N}\sum_{k\,=\,1}^{N} a^2(k) \;=\; C_3 < \infty\,. \tag{A1-21}$$

Further, since

$$\frac{1}{N}\sum_{k\,=\,1}^{N} [\hat{e}_\theta(k) - \omega(k)]^2 \ge 0\,,$$

inequality (L2-2) is obtained.

Proof of Eq. (L2-3):

Starting with Eq. (4-4), for a stable system

$$\|y(k)\|_2^2 \;\le M_1\|u(k)\|_2^2 \;+ M_2\|\omega(k)\|_2^2 \quad , \tag{A1-22}$$

where M_1 and M_2 are the l_1 norms of $B(q^{-1})/A(q^{-1})$ and $C(q^{-1})/A(q^{-1})$ respectively. Inequality (L2-3) is obtained by inserting Eq. (L1-2) into Eq. (A1-22).

Proof of Eq. (L2-4):

To show that Eq. (L1-4) is satisfied, notice that

$$\begin{aligned} F_\theta(k-1) \;&=\; F_\theta(k-2) + \lambda_\theta \phi^T(k-1)\phi(k-1), \\ F_\theta(k-1) - F_\theta(k-2) \;&=\; \lambda_\theta \phi^T(k-1)\phi(k-1), \end{aligned} \tag{A1-23}$$

which implies that

$$\frac{F_\theta(N-1)}{N} = \frac{\lambda_\theta}{N}\sum_{k=1}^{N}\phi^T(k-1)\phi(k-1) + \frac{F_\theta(0)}{N}. \tag{A1-24}$$

From Eq. (4-30), the following relation can be obtained

$$\begin{aligned}&\phi^T(k-1)\phi(k-1) = \\ &[y^2(k-1)\ldots y^2(k-\hat{n}_A)\ u^2(k-1)\ldots u^2(k-\hat{n}_B)\ \hat{e}_\theta^2(k-1)\ldots\hat{e}_\theta^2(k-\hat{n}_C)].\end{aligned} \tag{A1-25}$$

Since Eq. (A1-25) is a linear combination of the squares of $y(k)$, $u(k)$, and $\hat{e}_\theta(k)$, inequality (L2-4) is obtained from Eqs. (L2-1) through (L2-3) and Eq. (Al-25).

The proof of Theorem 1 will now be given.

Theorem 1. Consider the ARMAX representation of the regulated variable closed loop dynamics given by Eq. (4-6), with the auxiliary control action given by Eq. (4-38). Under the assumptions: a) $\omega(k)$ is a zero mean innovation signal with bounded covariance and b) the transfer function $C(z^{-1})$ is strictly input passive; c) $\hat{n}_A \geq n_A$, $\hat{n}_B \geq n_B$, and $\hat{n}_C \geq n_C$; d) the FIR filter parameter vector $\hat{H}(k)$ satisfies $|\hat{H}(k)| \leq h_{max} < \infty$; the Pseudo Linear Regression (PLR) algorithm given by Eq. (4-39) through Eq. (4-39) has the following properties:

$$\lim_{N\to\infty}\sum_{k=1}^{N}[\hat{\theta}(k)-\hat{\theta}(k-m)]^2 < \infty, \forall m < \infty, \tag{T1-1}$$

$$\lim_{N\to\infty}\frac{1}{N}\sum_{k=1}^{N}[e_\theta(k)-\omega(k)]^2 = 0, \tag{T1-2}$$

$$\lim_{N\to\infty}\frac{1}{N}\sum_{k=1}^{N}E_k[y(k)-\hat{y}(k)]^2 = \sigma^2, \text{ a.s.} \tag{T1-3}$$

$$\lim_{N\to\infty}\frac{1}{N}F_\theta(N-1) \leq \infty, \text{ a.s} \tag{T1-4}$$

The proof of Theorem 1 is almost identical as Theorem 8.5.1 in [27] with the exception of the following:

a.) The a-priori estimate of $\hat{y}(k)$ is used instead of a-posteriori estimate.

b.) The constants λ_θ and β_θ are introduced to the update law.

Proof of Eq. (T1-1):

First it has to be shown that the parameter error $\tilde{\theta}(k)$ is bounded. Define the non-negative martingale function

$$V(k) = \tilde{\theta}^T(k)\tilde{\theta}(k) . \tag{A1-26}$$

Subtracting θ_o from Eq. (4-31) yields

$$\tilde{\theta}(k) = \tilde{\theta}(k-1) + \frac{\beta_\theta}{F_\theta(k-1)}\phi(k-1)\hat{e}_\theta(k) . \tag{A1-27}$$

Multiplying by $\tilde{\theta}^T(k)$ yields

$$\begin{aligned}\tilde{\theta}^T(k)\tilde{\theta}(k) = \tilde{\theta}^T(k-1)\tilde{\theta}(k-1) &+ \frac{2\beta_\theta}{F_\theta(k-1)}\phi(k-1)\tilde{\theta}(k-1)\hat{e}_\theta(k) \\ &+ \frac{\beta_\theta^2}{F_\theta^2(k-1)}\phi^T(k-1)\phi(k-1)\hat{e}_\theta^2(k).\end{aligned} \tag{A1-28}$$

Substituting Eq. (A1-28) into Eq. (A1-26) yields

$$V(k) = V(k-1) - \frac{2\beta_\theta}{F_\theta(k-1)}\hat{b}(k)\hat{e}_\theta(k) + \frac{\beta_\theta^2}{F_\theta^2(k-1)}\phi^T(k-1)\phi(k-1)\hat{e}_\theta^2(k) . \tag{A1-29}$$

Adding and subtracting $\frac{2\beta_\theta}{F_\theta(k)}\hat{b}(k)\omega(k)$ from the right side of above equation yields

$$\begin{aligned}V(k) = V(k-1) - \frac{2\beta_\theta}{F_\theta(k-1)}\hat{b}(k)\hat{\eta}(k) &+ \frac{\beta_\theta^2}{F_\theta^2(k-1)}\phi^T(k-1)\phi(k-1)\hat{e}_\theta^2(k) \\ &- \frac{2\beta_\theta}{F_\theta(k-1)}\hat{b}(k)\omega(k).\end{aligned} \tag{A1-30}$$

Taking the conditional expectation E_k of both sides of Eq. (A1-30) and using the facts that $E_k[\omega^2(k)] = \rho^2$, $E_k[\hat{b}(k)\omega(k)] = 0$, and $E_k[\hat{e}(k)\omega(k)] = \sigma^2$ yields

$$E_k[V(k)] = V(k-1) - \frac{2\beta_\theta}{F_\theta(k-1)} E_k[\hat{b}(k)\hat{\eta}(k)] + \frac{\beta_\theta^2}{F_\theta{}^2(k-1)} \phi^T(k-1)\phi(k-1)\rho^2. \tag{A1-31}$$

Substituting the relation $C(q^{-1})\hat{\eta}(k) = \hat{b}(k)$ into the above equation yields the following relation

$$E_k[V(k)] = V(k-1) - \frac{2\beta_\theta}{F_\theta(k-1)} E_k[C(q^{-1})\hat{\eta}(k)\hat{\eta}(k)] + \frac{\beta_\theta{}^2}{F_\theta{}^2(k-1)} \phi^T(k-1)\phi(k-1)\rho^2. \tag{A1-32}$$

Since $C(q^{-1})$ is SPR, $E_k[C(q^{-1})\hat{\eta}(k)\hat{\eta}(k)] \geq 0, \forall k$. Moreover from Eq. (L1-1), it is known that

$$\lim_{N \to \infty} \sum_{k=1}^{N} \frac{\beta_\theta^2 \phi^T(k-1)\phi(k-1)}{F_\theta(k-1)F_\theta(k-2)} \rho^2 < \infty. \tag{A1-33}$$

Hence the conditions in Corollary D.5.1 are satisfied which implies that

$$\lim_{N \to \infty} E_N[V(N)] < \infty, \tag{A1-34}$$

or

$$\lim_{N \to \infty} sup \left\| \hat{\theta}(N) - \theta_o \right\|^2 < \infty. \tag{A1-35}$$

Further, from Corollary D.5.1, the following inequalities can be obtained

$$\lim_{N \to \infty} \sum_{k=0}^{N} \frac{2\beta_\theta}{F_\theta(k-1)} C(q^{-1})\hat{\eta}(k)\hat{\eta}(k) < \infty,$$
$$\lim_{N \to \infty} \sum_{k=0}^{N} \frac{(\hat{e}_\theta(k) - \omega(k))^2}{F_\theta(k-1)} < \infty. \tag{A1-36}$$

To obtain Eq. (T1-1) use the result from Lemma 1 that

$$\lim_{N\to\infty}\sum_{k=1}^{N}\frac{\beta_\theta^2\phi^T(k-1)\phi(k-1)}{F_\theta(k-1)F_\theta(k-1)}\hat{e}_\theta^2(k)<\infty\,, \tag{A1-37}$$

and since

$$\hat{\theta}(k) \;=\; \hat{\theta}(k-1)+\frac{\beta_\theta}{F_\theta(k-1)}\phi(k-1)\hat{e}_\theta(k)\,, \tag{A1-38}$$

that implies

$$\lim_{N\to\infty}\sum_{k=1}^{N}\left\|\hat{\theta}(k)-\hat{\theta}(k-1)\right\|^2<\infty\,. \tag{A1-39}$$

Using the Schwarz inequality theorem

$$\left\|\hat{\theta}(k)-\hat{\theta}(k-m)\right\|^2\le\left\|\hat{\theta}(k)-\hat{\theta}(k-1)\right\|^2+\ldots+\left\|\hat{\theta}(k-m+1)-\hat{\theta}(k-m)\right\|^2, \tag{A1-40}$$

and taking sums from 1 to N on both sides of the above inequality, the following relation can be obtained

$$\sum_{k=1}^{N}\left\|\hat{\theta}(k)-\hat{\theta}(k-m)\right\|^2\le$$
$$\sum_{k=1}^{N}\left\|\hat{\theta}(k)-\hat{\theta}(k-1)\right\|^2+\ldots+\sum_{k=1}^{N}\left\|\hat{\theta}(k-m+1)-\hat{\theta}(k-m)\right\|^2.$$

The following relation

$$\sum_{k=1}^{N}\left\|\hat{\theta}(k)-\hat{\theta}(k-2)\right\|^2\le\hat{\theta}(0)+\sum_{k=1}^{N}\left\|\hat{\theta}(k)-\hat{\theta}(k-1)\right\|^2 \tag{A1-41}$$

implies that

$$\sum_{k=1}^{N}\left\|\hat{\theta}(k)-\hat{\theta}(k-m)\right\|^2\le m\hat{\theta}(0)+m\sum_{k=1}^{N}\left\|\hat{\theta}(k)-\hat{\theta}(k-1)\right\|^2, \tag{A1-42}$$

which in turn implies

$$\sum_{k=1}^{N} \left\| \hat{\theta}(k) - \hat{\theta}(k-m) \right\|^2 < \infty . \tag{A1-43}$$

Eqs. (T1-2) through (T1-4) can be obtained using Lemma 2 combined with Eq. (A1-36).

A2. Proof of Theorem 2

Theorem 2. Consider the adaptive system described in Theorem 1 when the PAA algorithm given by Eqs. (4-36) through (4-38) is utilized and the signals $\hat{d}(k)$ *and* $\ddot{x}(k)$ *are generated by Eq. (4-32) and Eq. (4-35) respectively. Under the additional conditions that a projection algorithm is utilized so that the polynomial* $q^{\hat{n}_A}\hat{A}(k, q^{-1})$ *is always Hurwitz then*

1. *The parameter vector* $[\hat{\theta}(k)\ \ddot{H}(k)]$ *of the adaptive control algorithm converges with probability 1 to an equilibrium point* $[\bar{\theta}\ H]$.

2. *If* $\hat{\theta} \to \{\theta: \bar{B}/\bar{A} = B/A\}$ *then* $\ddot{H} \to H = H^\circ$, *where* H° *is the optimal Wiener filter parameter vector.*

3. *If* $[\hat{\theta}\ \hat{H}] \to [\bar{\theta}\ \bar{H}]$ *such that* $A_{acc}C(q^{-1}) + B_{acc}B(q^{-1})Q(q^{-1})$ *and* $\bar{A}(q^{-1})$ *are coprime and* $A_{acc} + B_{acc}Q(q^{-1})$ *and* A_{acc} *are co-prime with* $n_Q \geq \ddot{n}_A$, *then* $[\bar{\theta}\ H] \to [\theta\ H^\circ]$.

4. *If* $B/A = B/A$, *then* $[\theta\ H^\circ]$ *is locally stable equilibrium points of the adaptive system. Moreover,* $1/C(z)$ *is SPR.*

5. *If* $\hat{\theta} \to \{\bar{\theta}: \bar{B}^- = B^-\}$, *then,* $\lim_{n_Q \to \infty} Q = Q^\circ$ *where* $\bar{B}^-$ *and* B^- *contain all the roots of* B *and* B, *respectively, which are outside the unit circle.*

6. $B = 0$ *and* $Q = 0$ *is always an unstable equilibrium point of the closed loop adaptive system.*

Proof:

The proof is very similar to the one in [34] and is based on the Ljung's Ordinary Differential Equations (ODE) approach which is detailed in [59]. Define the overall

parameter vector:

$$\hat{\Theta} = [\hat{\theta}\ \hat{H}]^T \in \Re^{\hat{n}_T}, \qquad \hat{n}_T = \hat{n}_A + \hat{n}_B + \hat{n}_C + \hat{n}_Q . \tag{A2-1}$$

Using the notation in [59], the PAAs in Eqs. (4-29) through (4-31) and Eqs. (4-36) through (4-37) can be rewritten as follow

$$\begin{aligned} \hat{\theta}(k) &= \hat{\theta}(k-1) + \gamma(k)\beta_\theta R_\theta^{-1}(k-1)\phi(k-1)\hat{e}_\theta(k), \\ R_\theta(k-1) &= R_\theta(k-2) + \gamma(k)[\lambda_\theta \phi^T(k-1)\phi(k-1) - R_\theta(k-2)], \end{aligned} \tag{A2-2}$$

and

$$\begin{aligned} H(k) &= H(k-1) + \gamma(k)\beta_Q R_Q^{-1}(k)X(k-1)\hat{e}_Q(k), \\ R_Q(k) &= R_Q(k-1) + \gamma(k)\left[\lambda_Q \hat{X}^T(k-1)\hat{X}(k-1) - R_Q(k-1)\right], \end{aligned} \tag{A2-3}$$

where $\gamma(k) = 1/k$.

In order to use the ODE approach, it is necessary that the system satisfy a set of regularity and boundness conditions (e.g. conditions B.1 through B.11) given in [59]. Under the assumptions in the theorem and utilizing the results of Theorem 1, it can be verified that the conditions B.1 through B.11 in [59] are satisfied when $D_F = \left\{\hat{\Theta} \middle| R_\theta > 0, R_Q > 0\right\}$. The ODEs associated with Eqs. (A2-2) through (A2-3) are

$$\begin{aligned} \frac{d}{d\tau}\hat{\theta}(\tau) &= \beta_\theta R_\theta^{-1}(\tau) f_\theta(\hat{\Theta}(\tau)), \\ \frac{d}{d\tau}R_\theta(\tau) &= \lambda_\theta g_\theta(\hat{\Theta}(\tau)) - R_\theta(\tau), \end{aligned} \tag{A2-4}$$

$$\begin{aligned} \frac{d}{d\tau}\hat{H}(\tau) &= \beta_Q R_Q^{-1}(\tau) f_Q(\hat{\Theta}(\tau)), \\ \frac{d}{d\tau}R_Q(\tau) &= \lambda_Q g_Q(\hat{\Theta}(\tau)) - R_Q(\tau), \end{aligned} \tag{A2-5}$$

where

$$f_\theta(\hat{\Theta}) = E^{\Theta}\left\{\phi(k-1,\hat{\Theta})\hat{e}_\theta(k,\hat{\Theta})\right\},$$
$$g_\theta(\hat{\Theta}) = E^{\hat{\Theta}}\{\phi^T(k-1,\hat{\Theta})\phi(k-1,\hat{\Theta})\}. \tag{A2-6}$$

and

$$f_Q(\Theta) = E^{\Theta}\left\{X(k,\Theta)\hat{e}_Q(k,\Theta)\right\},$$
$$g_Q(\hat{\Theta}) = E^{\hat{\Theta}}\left\{\hat{X}^T(k,\hat{\Theta})\hat{X}(k,\hat{\Theta})\right\}. \tag{A2-7}$$

For example, $E^{\hat{\Theta}}\left\{\phi(k-1,\hat{\Theta})\hat{e}_\theta(k,\hat{\Theta})\right\}$ denotes

$$E^{\hat{\Theta}}\left\{\phi(k-1,\hat{\Theta})\hat{e}_\theta(k,\hat{\Theta})\right\} = \lim_{N\to\infty}\frac{1}{N}\sum_{k=1}^{N}\phi(k-1,\hat{\Theta})\hat{e}_\theta(k,\hat{\Theta}), \tag{A2-8}$$

where the parameter, Θ, is kept constant in the calculation of the expectation.

Proof of Part 1:

The invariant set and domain of attraction of the ODE in Eq. (A2-4) will now be determined. Define the parameter error vectors and the positive definite function:

$$\tilde{\theta}(\tau) = \hat{\theta}(\tau) - \theta, \tag{A2-9}$$

$$V(\tau) = \tilde{\theta}^T(\tau)\tilde{\theta}(\tau). \tag{A2-10}$$

In what follows, $\dot{f}_\theta(\tau) \equiv \frac{d}{d\tau}f_\theta(\tau)$. Using the result on page 210 in [59], the following relation can be found:

$$\hat{e}_\theta(k) = -\frac{1}{C(q^{-1})}\phi^T(k-1)\tilde{\theta}(k-1) + \omega(k). \tag{A2-11}$$

Substituting this result into Eq. (A2-6) yields

$$\dot{\tilde{\theta}}(\tau) = -\beta_\theta R_\theta^{-1}(\tau)G_{\theta f}(\tau)\tilde{\theta}(\tau), \tag{A2-12}$$

where

$$G_{\theta f}(\hat{\Theta}(\tau)) = E^{\Theta}\{\phi(k-1,\hat{\Theta})((1/C(q^{-1}))\phi^T(k-1,\hat{\Theta}))\}. \tag{A2-13}$$

Hence

$$\dot{V}(\tau) = -\beta_\theta R_\theta^{-1}\tilde{\theta}^T(\tau)[G_{\theta f}^T(\tau) + G_{\theta f}(\tau)]\tilde{\theta}(\tau) . \tag{A2-14}$$

C(z) strictly input passive implies that $G^T{}_{\theta f}(\tau) + G_{\theta f}(\tau) \geq 0$. Further, since $\lambda_\theta g_\theta(\tau) \geq 0$ and $\beta_\theta > 0$ yields

$$\dot{V}(\tau) = -\tilde{\theta}^T(\tau)S(\tau)\tilde{\theta}(\tau) , \tag{A2-15}$$

where

$$S(\tau) = \beta_\theta R_\theta^{-1}[G_{\theta f}^T(\tau) + G_{\theta f}(\tau)] . \tag{A2-16}$$

Since $\dot{V}(\tilde{\theta})$ is negative semi-definite, $V(\tilde{\theta}) \in L_\infty$ which in turn implies that $\tilde{\theta} \in L_\infty$.

Integrating both sides of Eq. (A2-15) yields

$$\int_0^t \dot{V}(\tau)d\tau = -\int_0^t \tilde{\theta}^T(\tau)S(\tau)\tilde{\theta}(\tau)d\tau , \tag{A2-17}$$

$$\int_0^t \tilde{\theta}^T(\tau)S(\tau)\tilde{\theta}(\tau)d\tau = V(\tilde{\theta}(0)) - V(\tilde{\theta}(t)) < \infty . \tag{A2-18}$$

Hence, $\dot{V}(\tilde{\theta}) \in L_1$ which in turn implies that $\dot{V}(\tilde{\theta}) \in L_1 \cap L_\infty$. To use Barbarlot's lemma, $\ddot{V}(\tilde{\theta}) \in L_\infty$ has to be shown. Taking the derivative of Eq. (A2-15) yields

$$\ddot{V}(\tau) = -\dot{\tilde{\theta}}^T(\tau)S(\tau)\tilde{\theta}(\tau) - \tilde{\theta}^T(\tau)\dot{S}(\tau)\tilde{\theta}(\tau) - \tilde{\theta}^T(\tau)S(\tau)\dot{\tilde{\theta}}(\tau) \tag{A2-19}$$

Since $G_{\theta f}(\tau)$ is a linear combination of bounded elements, it must be bounded. $G_{\theta f}(\tau) \in L_\infty$ implies that $\dot{\tilde{\theta}}(\tau) \in L_\infty$. Hence the first and last terms on the right hand side of Eq. (A2-19) are bounded. It only remains to show that $\dot{S}(\tau) \in L_\infty$. Taking the derivative of Eq. (A2-16) yields

$$\begin{aligned}\dot{S}(\tau) = \beta_\theta \dot{R}_\theta^{-1}[G_{\theta f}^T(\tau) + G_{\theta f}(\tau)] + \beta_\theta R_\theta^{-1}[\dot{G}_{\theta f}^T(\tau) + G_{\theta f}(\tau)] \\ + \beta_\theta \dot{R}_\theta^{-1}[G_{\theta f}^T(\tau) + \dot{G}_{\theta f}(\tau)].\end{aligned} \tag{A2-20}$$

Since $g_\theta(\tau) \in L_\infty$ and $R_\theta(\tau) \in L_\infty$ yields $\dot{R}^{-1}(\tau) \in L_\infty$. Further, since $\dot{G}_{\theta f}(\tau)$ is a

linear combination of bounded elements since $\dot{\tilde{\theta}}(\tau) \in L_\infty$ implies that $\dot{G}_{\theta f}(\tau) \in L_\infty$ which in turn implies that $\dot{S}(\tau) \in L_\infty$. Hence, $\ddot{V}(\tilde{\theta}) \in L_\infty$. Since $\ddot{V}(\tilde{\theta}) \in L_\infty$ and $\dot{V}(\tilde{\theta}) \in L_1 \cap L_\infty$, Barbarlot's lemma yields $\dot{V}(\tilde{\theta}) \to 0$. Hence, the invariant set of the parameter estimate error $\tilde{\theta}$ is

$$\begin{aligned} D_{\tilde{\theta}} &= \{\theta \mid \dot{V}(\theta(\tau)) = 0\}, \\ &= \left\{ \tilde{\theta} \middle| G_{\theta f}(\tilde{\Theta}) = 0 \right\}, \end{aligned} \tag{A2-21}$$

where $G_{\theta f}(\tilde{\Theta})$ is defined in Eq. (A2-13). Eq. (A2-15) implies that

$$\begin{aligned} &\hat{\theta}(\tau) \to \{\bar{\theta} \middle| G_{\theta f}(\tau)(\theta - \bar{\theta}) = 0\}, \\ &\dot{\tilde{\theta}}(\tau) \to 0. \end{aligned} \tag{A2-22}$$

The above relation can be further simplified

$$\begin{aligned} &\hat{\theta}(\tau) \to \left\{ \bar{\theta} \middle| E^{\hat{\Theta}}\{\phi(k-1, \hat{\Theta})\phi^T(k-1, \hat{\Theta})\}(\theta - \bar{\theta}) = 0 \right\}, \\ &\dot{\tilde{\theta}}(\tau) \to 0. \end{aligned} \tag{A2-23}$$

Using the above facts about $\dot{V}(\tilde{\theta}(\tau))$ as well as Eq. (A2-12) and the boundness assumption (conditions B.1 through B.11 in [59]), $\tilde{\theta}(\tau) \in L_1 \cap L_\infty$ and $\dot{\tilde{\theta}}(\tau) \in L_1 \cap L_\infty$ can be concluded.

The invariant set and the domain of attraction of the ODE in Eq. (A2-5) will now be determined. Define the vector $H^*(\tau)$ which satisfies the following relation

$$p(\tau) - G_Q(\tau)H^*(\tau) = 0, \tag{A2-24}$$

where $G_Q(\tau)$ and $G_Q(\tau)$ are defined by the following relations

$$\begin{aligned} G_Q(\tau) &= E^{\Theta}\left\{ \hat{X}(k, \hat{\Theta})\hat{X}^T(k, \hat{\Theta}) \right\}, \\ p(\tau) &= E^{\hat{\Theta}}\{\hat{X}(k, \hat{\Theta})\hat{z}(k, \hat{\Theta})\} \end{aligned} \tag{A2-25}$$

Hence

$$H^*(\tau) = G_Q^{\#}(\tau)p(\tau), \tag{A2-26}$$

where $G_Q^{\#}(\tau)$ denotes the pseudo inverse of $G_Q(\tau)$. Taking the derivative of Eq. (A2-24) yields

$$\dot{p}(\tau) - \dot{G}_Q(\tau)H^*(\tau) - G_Q(\tau)\dot{H}^*(\tau) = 0. \tag{A2-27}$$

By the definition of $G_Q(\tau)$ and $p(\tau)$ in Eq. (A2-25) and utilizing the condition in the theorem that $\hat{A}(q^*)$ is Hurwitz, $H^*(\tau) \in L_\infty$ since $p(\tau)$ is always in the range space of $G_Q(\tau)$. From the definition of $\tilde{\theta}(\tau) \in L_1 \cap L_\infty$ and $\tilde{\theta}(\tau) \in L_1 \cap L_\infty$ in Eq. (4-32) and Eq. (4-35), the following relations can be obtained

$$\begin{aligned} p(\tau) \to \bar{p} &= E\{\bar{X}(k, \bar{\Theta})\bar{d}(k, \bar{\Theta})\}, \\ G_Q(\tau) \to \bar{G}_Q &= E\left\{\bar{X}(k, \bar{\Theta})\bar{X}^T(k, \bar{\Theta})\right\}, \\ H^*(\tau) &\to \{H^*(\tau) \to \bar{H} \,|\, \bar{G}_Q\bar{H} = \bar{p}\}, \end{aligned} \tag{A2-28}$$

where

$$\begin{aligned} \bar{x}(k) &= -\frac{\bar{B}(q^{-1})}{\bar{A}(q^{-1})}a(k), \\ \bar{d}(k) &= \frac{\bar{C}(q^{-1})}{\bar{A}(q^{-1})}\bar{e}_\theta(k), \\ \bar{X}(k) &= [\bar{x}(k)\ \bar{x}(k-1)\ldots\bar{x}(k-\hat{n}_Q)\ ]. \end{aligned} \tag{A2-29}$$

Using Eq. (A2-11), the following relation can be derived

$$E\left\{\left|\bar{e}_\theta(k) - \omega(k)\right|^2\right\} = E\left\{\left|\frac{1}{C(q^{-1})}\phi^T(k-1)\tilde{\theta}(k-1)\right|^2\right\} = 0. \tag{A2-30}$$

Going back to the definitions of $p(\tau)$ and $G_Q(\tau)$, Eq. (A2-27) can be rewritten as

$$E^{\hat{\Theta}}\left\{\dot{\hat{X}}(k,\hat{\Theta})\hat{d}(k,\hat{\Theta})\right\}+E^{\hat{\Theta}}\left\{\hat{X}(k,\hat{\Theta})\dot{\hat{d}}(k,\hat{\Theta})\right\}-E^{\hat{\Theta}}\left\{\dot{\hat{X}}(k,\hat{\Theta})\hat{X}^{T}(k,\hat{\Theta})\right\}H^{*}(\tau)- E^{\hat{\Theta}}\left\{\hat{X}(k,\hat{\Theta})\dot{\hat{X}}^{T}(k,\hat{\Theta})\right\}H^{*}(\tau)-G_{Q}(\tau)\dot{H}^{*}(\tau)=0. \tag{A2-31}$$

Using the fact that the expectation operator can be rewritten as

$$E^{\hat{\Theta}}\{\hat{X}(k,\hat{\Theta})\hat{d}(k,\hat{\Theta})\}=\lim_{N\to\infty}\frac{1}{N}\sum_{i=1}^{N}\hat{X}_j(k,\hat{\Theta})\hat{d}_j(k,\hat{\Theta}) \ , \tag{A-32}$$

which in turn can be rewritten in vector notation as

$$E^{\hat{\Theta}}\{\hat{X}(k,\hat{\Theta})\hat{d}(k,\hat{\Theta})\}=\lim_{N\to\infty}\frac{1}{N}\hat{\underline{X}}_N(k,\hat{\Theta})\hat{\underline{D}}_N(k,\hat{\Theta}) \ , \tag{A-33}$$

where $\hat{\underline{X}}_N(k,\hat{\Theta})=(1/N)[\hat{X}_1(k,\hat{\Theta})\ \hat{X}_2(k,\hat{\Theta})\ldots\hat{X}_N(k,\hat{\Theta})]$ and $\hat{\underline{D}}_N(k,\hat{\Theta})=[\hat{d}_1(k,\hat{\Theta})\ \hat{d}_2(k,\hat{\Theta})\ldots\hat{d}_N(k,\hat{\Theta})]$. Rewriting Eq. (A2-31) in vector notation yields

$$\hat{\underline{X}}_N(k,\hat{\Theta})\hat{\underline{D}}_N(k,\hat{\Theta})+\hat{\underline{X}}_N(k,\hat{\Theta})\hat{\underline{D}}_N(k,\hat{\Theta})-\hat{\underline{X}}_N(k,\hat{\Theta})\hat{\underline{X}}^{T}_{N}(k,\hat{\Theta})H^{*}(\tau)- \hat{\underline{X}}_N(k,\hat{\Theta})\dot{\hat{\underline{X}}}^{T}_{N}(k,\hat{\Theta})H^{*}(\tau)-G_{O}(\tau)\dot{H}^{*}(\tau)=0. \tag{A2-34}$$

Since $H^{*}(\tau)$ is a Wiener solution, it is equal to

$$H^{*}(\tau)=\left[\hat{\underline{X}}_N(k,\hat{\Theta})\hat{\underline{X}}^{T}_{N}(k,\hat{\Theta})\right]^{\#}\hat{\underline{X}}_N(k,\hat{\Theta})\hat{\underline{D}}_N(k,\hat{\Theta}) \ . \tag{A2-35}$$

Substituting Eq. (A2-35) into Eq. (A2-34) and utilizing properties of the pseudoinverse yields

$$G_{Q}(\tau)\dot{H}^{*}(\tau)=\hat{\underline{X}}_N(k,\hat{\Theta})\hat{\underline{D}}_N(k,\hat{\Theta})-\hat{\underline{X}}_N(k,\hat{\Theta})\hat{\underline{X}}^{T}_{N}(k,\hat{\Theta})H^{*}(\tau). \tag{A2-36}$$

Since $G_Q(\tau)\in L_\infty$ and $G_Q(\tau)\notin L_\infty$ and further, all the terms on the right hand side of Eq. (A2-36) are in L_1 that implies that $\dot{H}^{*}(\tau)\in L_1$. From Eq. (A2-27), it is known that $\dot{H}^{*}(\tau)\in L_\infty$. Therefore, $\dot{H}^{*}(\tau)\in L_2\cap L_\infty$. An alternative proof of this fact is given in [56].

Define the parameter estimation error vector as

$$\tilde{H}(\tau) = \hat{H}(\tau) - H^*(\tau). \tag{A2-37}$$

Then

$$\begin{aligned} \hat{d}(k) &= \hat{X}^T H^* + \hat{e}_Q, \\ \hat{d}(k) &= \hat{X}^T H^* + \xi. \end{aligned} \tag{A2-38}$$

Since H^* is a Wiener filter solution, the following relation holds

$$E[\hat{X}\xi] = 0. \tag{A2-39}$$

From Eq. (A2-38),

$$\hat{e}_Q = -\hat{X}^T H^* + \xi. \tag{A2-40}$$

Substituting Eq. (A2-40) into Eq. (A2-7) yields

$$f_Q = E[\hat{X}\hat{e}_Q] = E[\hat{X}(-\hat{X}^T H^* + \xi)] = -G_Q\tilde{H}. \tag{A2-41}$$

Therefore, from Eq. (A2-5)

$$\begin{aligned} \dot{\hat{H}} &= -\beta_Q R_Q(\tau) G_Q(\tau)\tilde{H}(\tau), \\ \dot{\tilde{H}} &= -\beta_Q R_Q(\tau) G_Q(\tau)\tilde{H}(\tau) - \dot{H}^*(\tau). \end{aligned} \tag{A2-42}$$

Define the positive definite function

$$V(\tilde{H}(\tau)) = \tilde{H}^T(\tau)\tilde{H}(\tau). \tag{A2-43}$$

Taking the time derivative of $V(\tilde{H}(\tau))$ and inserting Eq. (A2-41) yields

$$\dot{V}(\tilde{H}(\tau)) = -2\beta_Q R_Q(\tau)\tilde{H}^T(\tau) G_Q(\tau)\tilde{H}(\tau) - 2\tilde{H}^T(\tau)\dot{H}^*(\tau). \tag{A2-44}$$

Completing the squares in Eq. (A2-44) yields

$$\dot{V}(\tilde{H}(\tau)) = -2\beta_Q R_Q(\tau)\tilde{H}^T G_Q\tilde{H} - (\tilde{H}^T + \dot{H}^*)^T(\tilde{H}^T + \dot{H}^*) + \dot{H}^{*T}\dot{H}^*. \tag{A2-45}$$

Since $\dot{H}^{*}(\tau) \in L_2 \cap L_\infty$ and $G_Q(\tau) \in L_\infty$ and using the Schwartz inequality, from Eq. (A2-45), it can be concluded that $\dot{H}(\tau) \in L_2 \cap L_\infty$. Moreover, by Eq. (A2-42) it can be concluded that $\dot{\tilde{H}}(\tau) \in L_\infty$. Hence, by Barbalat's lemma, $\tilde{H}(\tau) \to 0$. Thus the domain of attraction of the ODE in Eq. (A2-5) is $D_{\bar{Q}}$ which is defined by

$$\dot{H}(\tau) \to \{H \,|\, G_Q H = \bar{p}\} \tag{A2-46}$$

where G_Q and $\bar{p}$ were defined in Eq. (A2-28). This establishes the first result of the theorem.

The proof of the remaining results in this theorem is based on Theorem 2 of Ljung [59] which states that the adaptive algorithm can only converge to the stable equilibrium points of the ODEs of Eq. (A2-4) and Eq. (A2-5). The conditions under which these equilibrium points are stable will be determined.

Proof of Part 2:

Denote the vector and the scalars

$$\begin{aligned} \bar{\Theta} &= [\bar{\theta}\ \bar{H}]^T, \\ \bar{F}_\theta &= \lambda_\theta g_\theta(\bar{\Theta}), \bar{F}_Q = \lambda_Q g_Q(\bar{\Theta}), \end{aligned} \tag{A2-47}$$

to be an equilibrium point of the ODEs in Eq. (A2-4) and Eq. (A2-5), and define the stationary polynomials

$$\begin{aligned} \bar{A}(q^{-1}) &= \hat{A}(\bar{\theta}, q^{-1}), \bar{B}(q^{-1}) = \hat{B}(\bar{\theta}, q^{-1}), \\ \bar{C}(q^{-1}) &= \hat{C}(\bar{\theta}, q^{-1}), \bar{D}(q^{-1}) = \hat{D}(\bar{\theta}, q^{-1}). \end{aligned} \tag{A2-48}$$

Now consider the stationary conditions

$$\begin{aligned} f_\theta(\Theta) &= E^{\breve{}}\left\{\phi(k-1,\Theta)e_\theta(k,\Theta)\right\} = E\{\phi(k-1)e_\theta(k)\} = 0, \\ f_Q(\bar{\Theta}) &= E^{\bar{\Theta}}\left\{\bar{X}(k,\bar{\Theta})\bar{e}_Q(k,\bar{\Theta})\right\} = E\{\bar{X}(k)\bar{e}_Q(k)\} = 0, \end{aligned} \tag{A2-49}$$

where

$$\begin{aligned}
\bar{x}(k) &= -\frac{\bar{B}(q^{-1})}{\bar{A}(q^{-1})}a(k), \\
\bar{d}(k) &= \frac{\bar{C}(q^{-1})}{\bar{A}(q^{-1})}\bar{e}_\theta(k), \\
\bar{X}(k) &= [\bar{x}(k)\ \bar{x}(k-1)\ldots\bar{x}(k-\hat{n}_Q)\ ], \\
\bar{\phi}(k) &= [-\bar{y}(k)\ldots+-\bar{y}(k-\hat{n}_A)\ u(k)\ldots u(k-\hat{n}_B)\ \bar{e}_\theta(k)\ldots\bar{e}_\theta(k-\hat{n}_C)\ ],
\end{aligned} \tag{A2-50}$$

and

$$\begin{bmatrix} A & 0 \\ \bar{A} & -\bar{C} \end{bmatrix}\begin{bmatrix} y \\ \bar{e}_\theta \end{bmatrix} = \begin{bmatrix} \dfrac{B_{acc}B\bar{Q}}{A_{acc}} + C \\ \dfrac{B_{acc}\bar{B}\bar{Q}}{A_{acc}} \end{bmatrix}\omega(k)\,. \tag{A2-51}$$

Solving for y and $\bar{e}_\theta$ from Eq. (A2-51) yields

$$\begin{aligned}
y &= \frac{B_{acc}B\bar{Q} + CA_{acc}}{A_{acc}A}\omega(k), \\
\bar{e}_\theta &= \frac{1}{A\bar{C}}\left(\bar{A}\left(\frac{B_{acc}B\bar{Q} + A_{acc}C}{A_{acc}}\right) - A\left(\frac{B_{acc}\bar{B}\bar{Q}}{A_{acc}}\right)\right)\omega(k).
\end{aligned} \tag{A2-52}$$

From Theorem 1, or alternatively Eq. (A2-30) and Eq. (A2-49), it can be concluded that $\bar{e}_\theta = \omega(k)$. Thus by Eq. (A2-52) the following equality must be satisfied

$$\frac{1}{A\bar{C}}\left(\bar{A}\left(\frac{B_{acc}B\bar{Q} + A_{acc}C}{A_{acc}}\right) - A\left(\frac{B_{acc}\bar{B}\bar{Q}}{A_{acc}}\right)\right) = 1. \tag{A2-53}$$

Since $C^*(q)$ is Hurwitz, $A^*(q)C^*(q)$ is also Hurwitz. Hence, Eq. (A2-53) states that the following equality holds

$$\frac{B_{acc}BQ + A_{acc}C}{A_{acc}A} = \frac{B_{acc}BQ + A_{acc}C}{A_{acc}\bar{A}}\,. \tag{A2-54}$$

Using the fact that $\bar{Q}$ minimizes $E\left\{\bar{X}(\bar{d} + \bar{X}^T\bar{H})\right\}$ and as a consequence of the right hand side of Eq. (A2-54), if $\hat{\theta} \to \{\bar{\theta}\,|\,\bar{B}/\bar{A} = B/A\}$, then according to the Principle of

Orthogonality

$$E\left\{\left[\frac{B_{acc}\bar{B}}{A_{acc}\bar{A}}\Omega^T(k)\right]\left[\frac{\bar{C}}{\bar{A}}\omega(k)+\frac{B_{acc}\bar{B}}{A_{acc}\bar{A}}\Omega^T(k)\bar{H}\right]\right\}=$$
$$E\left\{\left[\frac{B_{acc}B}{A_{acc}A}\Omega^T(k)\right]\left[\frac{\bar{C}}{\bar{A}}\omega(k)+\frac{B_{acc}B}{A_{acc}A}\Omega^T(k)\bar{H}\right]\right\}=0 \quad \text{(A2-55)}$$

where $\Omega^T(k) = [\omega(k)\ \omega(k-1)\ldots\omega(k-\hat{n}_Q)]$. Hence, it can be concluded that $\bar{Q} = Q^\circ$.

Proof of Part 3:

In order to establish sufficient conditions for the true parameter vector θ to be the only equilibrium point of the ODEs in Eq. (A2-4) and Eq. (A2-5), consider the case when $n_A = n_B = n_C = \hat{n}_A = \hat{n}_B = \hat{n}_C = \hat{n}_Q = n$ and define

$$\begin{aligned}&\tilde{\theta} = \theta - \bar{\theta},\\ &\tilde{A} = A - \bar{A},\ \tilde{B} = B - \bar{B},\ \tilde{C} = C - \bar{C}.\end{aligned} \quad \text{(A2-56)}$$

Eq. (A2-54) can be rewritten as follows

$$(B_{acc}BQ + A_{acc}C)\tilde{A} + AB_{acc}Q\tilde{B} + AA_{acc}\tilde{C} = 0\ , \quad \text{(A2-57)}$$

which can be in turn expressed as $\bar{T}\tilde{\theta} = 0$, where $\bar{T}$ is a Sylvester type matrix (see [56] for details). $\bar{T}$ will be of rank 3n if and only if $\hat{n}_Q \geq n$ and the following two sets of polynomials are coprime: $(B_{acc}\bar{B}\bar{Q} + A_{acc}\bar{C},\ \bar{A})$ and $(B_{acc}Q,\ A_{acc})$. The first condition is required because $\bar{T}$ is actually a $(2n + \hat{n}_Q)x3n$ matrix. If $\hat{n}_Q < n$, then T will have less rows than $3n$, and its rank will certainly be less than $3n$. Thus if the above conditions are satisfied, $\tilde{\theta} = 0$. Therefore $\bar{Q} = Q^\circ$, according to Part 2 of the theorem.

Proof of Part 4:

In order to show that the equilibrium point formed by the vector $\bar{\Theta} = [\bar{\theta}\ \bar{H}]^T$ and the scalars $\bar{F}_\theta = \lambda_\theta g_\theta(\bar{\Theta})$ and $\bar{F}_Q = \lambda_Q g_Q(\bar{\Theta})$ is a locally stable equilibrium state of the ODEs in Eq. (A2-4) and Eq. (A2-5), it is necessary and sufficient to show that the matrix

$$M(\bar{\Theta}) = \left[\begin{array}{c} g_\theta^{-1}(\hat{\Theta})\dfrac{\partial}{\partial\hat{\Theta}}f_\theta(\hat{\Theta}) \\ g_Q^{-1}(\hat{\Theta})\dfrac{\partial}{\partial\hat{\Theta}}f_Q(\hat{\Theta}) \end{array}\right]_{\hat{\Theta}=\bar{\Theta}} \tag{A2-58}$$

has all its eigenvalues in the left half plane [58].

To calculate the first entry of the matrix described by Eq. (A2-58), consider f_θ as described by Eq. (A2-6)

$$\begin{aligned} \frac{\partial}{\partial\bar{\Theta}}f_\theta(\hat{\Theta}) &= E\left[\left(\frac{\partial}{\partial\hat{\Theta}}\bar{\phi}\right)\bar{e}_\theta\right] + E\left[\phi\frac{\partial\bar{e}_\theta}{\partial\hat{\Theta}}\right], \\ &= E\left[\phi\frac{\partial\bar{e}_\theta}{\partial\hat{\Theta}}\right], \end{aligned} \tag{A2-59}$$

since $\bar{e}_\theta(k) = \omega(k)$ in the equilibrium state. Define the following symbols to be used in the calculation of $\partial\bar{e}_\theta/\partial\bar{\Theta}$

$$\begin{aligned} \omega_A(k-1) &= [\omega(k-1)\ldots\omega(k-n_A)]^T, \\ \delta\bar{A}(q^{-1}) &= (\delta\bar{a}_1)q^{-1} + \ldots + (\delta\bar{a}_{n_A})q^{-n_A}, \\ \delta\bar{A}_\theta &= [\delta\bar{a}_1\ldots\delta\bar{a}_{n_A}]^T. \end{aligned} \tag{A2-60}$$

Similar definitions can be used for the $\bar{B}$, $\bar{C}$, and $\bar{Q}$ polynomials. Hence

$$\begin{aligned} \frac{\partial\bar{e}_\theta}{\partial\bar{\Theta}} &= \frac{1}{A_a\bar{A}\bar{C}}[\delta\bar{A}(B_{acc}B\bar{Q} + A_{acc}C) + \bar{A}B_{acc}B\delta\bar{Q} - AB_{acc}\bar{Q}\delta\bar{B} - AB_{acc}\bar{B}\delta\bar{Q}]\bar{e}_\theta \\ &\quad -\frac{1}{A_a\bar{A}\bar{C}^2}[\bar{A}(B_{acc}B\bar{Q} + A_{acc}C) - AB_{acc}\bar{B}\bar{Q}]\delta\bar{C}\bar{e}_\theta \end{aligned} \tag{A2-61}$$

Using Eq. (A2-53) in Eq. (A2-61) yields

$$\frac{\partial \bar{e}_\theta}{\partial \bar{\Theta}} = \frac{1}{A_{acc}\bar{A}C}[\delta\bar{A}(B_{acc}B\bar{Q} + A_{acc}C) - AB_{acc}\bar{Q}\delta\bar{B} + (\bar{A}B_{acc}B - AB_{acc}\bar{B})\delta\bar{Q}]\bar{e}_\theta - \frac{1}{\bar{C}}\delta\bar{C}\bar{e}_\theta. \tag{A2-62}$$

Using the definitions in Eq. (A2-60) yields

$$\frac{\partial \bar{e}_\theta}{\partial \bar{\Theta}} = \frac{1}{\bar{C}}\left[\frac{(B_{acc}B\bar{Q} + A_{acc}C)}{A_{acc}A}\omega_A^T\right]\delta\bar{A}_\theta - \frac{1}{\bar{C}}\left[\frac{B_{acc}\bar{Q}}{A_{acc}A}\omega_B^T\right]\delta\bar{B}_\theta - \frac{1}{\bar{C}}\omega_C^T\delta\bar{C}_\theta + \left[\frac{(\bar{A}B_{acc}B - AB_{acc}\bar{B})}{A_{acc}A}\omega_Q^T\right]\delta\bar{H} \tag{A2-63}$$

Define

$$\begin{aligned} X_f(k) &= \frac{B_{acc}B}{A_{acc}A}\bar{e}_\theta(k) = \frac{B_{acc}B}{A_{acc}A}\omega(k), \\ \bar{X}_f(k) &= \frac{B_{acc}\bar{B}}{A_{acc}\bar{A}}\bar{e}_\theta(k) = \frac{B_{acc}\bar{B}}{A_{acc}\bar{A}}\omega(k), \\ \bar{\phi}_f(k) &= \frac{1}{\bar{C}}\phi(k), \end{aligned} \tag{A2-64}$$

where $\phi(k)$ is defined in Eq. (4-30). Using the fact that

$$\begin{aligned} y(k) &= \frac{1}{A_{acc}A}(B_{acc}B\bar{Q} + A_{acc}C)\omega(k), \\ u(k) &= \bar{Q}\frac{B_{acc}}{A_{acc}}\omega(k), \end{aligned} \tag{A2-65}$$

yields

$$\delta\bar{e}_\theta = -\bar{\phi}_f^T\delta\bar{\theta} + (X_f - \bar{X}_f)^T\delta\bar{H} \quad . \tag{A2-66}$$

Hence the first two entries of the matrix $M(\bar{\Theta})$ are

$$\begin{aligned} M_{11} &= -g_\theta^{-1}(\Theta)E[\bar{\phi}\bar{\phi}_f^T], \\ M_{12} &= -g_Q^{-1}(\bar{\Theta})E\left[\bar{\phi}(\bar{X}_f - X_f)^T\right]. \end{aligned} \tag{A2-67}$$

To calculate the second entry of the matrix described by Eq. (A2-58), consider f_Q as described by Eq. (A2-7)

$$\frac{\partial}{\partial\Theta}\bar{f}_Q(\hat{\Theta}) = E\left[\left(\frac{\partial}{\partial\hat{\Theta}}\bar{X}\right)\bar{e}_Q\right] + E\left[\bar{X}\frac{\partial\bar{e}_Q}{\partial\hat{\Theta}}\right]. \tag{A2-68}$$

First the perturbation of $\bar{X}$ is calculated. Since $\bar{X}$ is defined as

$$\begin{aligned} X(k) &= [\bar{x}(k)\ \bar{x}(k-1)\ldots\bar{x}(k-n_Q)]^t, \\ \bar{X}(k) &= \left[-\frac{B_{acc}\bar{B}}{A_{acc}\bar{A}}\,\omega(k)\ -\frac{B_{acc}\bar{B}}{A_{acc}\bar{A}}\,\omega(k-1)\ldots-\frac{B_{acc}\bar{B}}{A_{acc}\bar{A}}\,\omega(k-n_Q)\right]^T. \end{aligned} \tag{A2-69}$$

Hence

$$\begin{aligned} \delta\bar{X}(k) = \Bigg[&\frac{B_{acc}B}{A_{acc}\bar{A}^2}\,\delta\bar{A}\omega(k)\ -\frac{B_{acc}}{A_{acc}\bar{A}}\,\delta\bar{B}\omega(k)\ldots \\ &\frac{B_{acc}\bar{B}}{A_{acc}\bar{A}^2}\,\delta\bar{A}\omega(k-n_Q)\ -\frac{B_{acc}}{A_{acc}\bar{A}}\,\delta\bar{B}\omega(k-n_Q)\Bigg]^T. \end{aligned} \tag{A2-70}$$

Using the definitions from Eq. (A2-60), the following relation can be derived

$$\begin{aligned} \delta\bar{X}(k) = \Bigg[&\frac{B_{acc}B}{A_{acc}\bar{A}^2}\omega_A^T(k)\delta\bar{A}_\theta\ -\frac{B_{acc}}{A_{acc}\bar{A}}\,\omega_B^T(k)\delta\bar{B}_\theta\ \ldots \\ &\frac{B_{acc}\bar{B}}{A_{acc}\bar{A}^2}\,\omega_A^T(k-n_Q)\delta\bar{A}_\theta\ -\frac{B_{acc}}{A_{acc}\bar{A}}\,\omega_B^T(k-n_Q)\delta\bar{B}_\theta\Bigg]^T. \end{aligned} \tag{A2-71}$$

To calculate the $E[\bar{X}\delta\bar{e}_Q/\delta\bar{\Theta}]$ term, the following relation for $\bar{e}_Q(k)$ is used

$$\bar{e}_Q(k) = \left[\frac{CA_a - B_aB\bar{Q}}{A_aA}\right]\bar{e}_\theta(k). \tag{A2-72}$$

Taking the partial derivative on both sides yields

$$\delta\bar{e}_Q(k) = \frac{1}{\bar{A}}\omega_C^T\delta\bar{C}_\theta + \frac{B_{acc}Q}{A_{acc}\bar{A}}\omega_B^T\delta\bar{B}_\theta - \frac{CA_{acc}+B_{acc}Q}{A_{acc}\bar{A}^2}\omega_B^T\delta\bar{B}_\theta + \frac{B_{acc}B}{A_{acc}\bar{A}}\omega_Q^T\delta\bar{H} + \frac{\bar{C}A_{acc}+B_{acc}B\bar{Q}}{A_{acc}\bar{A}}\delta\bar{e}_\theta. \tag{A2-73}$$

Simplifying Eq. (A2-73) yields

$$\delta\bar{e}_Q(k) = \frac{1}{\bar{A}}\phi^T\delta\bar{\theta} + \frac{B_{acc}B}{A_{acc}\bar{A}}\omega_Q^T\delta\bar{H} + \frac{CA_{acc}+B_{acc}BQ}{A_{acc}\bar{A}}\delta\bar{e}_\theta. \tag{A2-74}$$

Using Eq. (A2-66) to simply Eq. (A2-74) even further yields

$$\delta\bar{e}_Q(k) = -\left(\frac{B_{acc}\bar{B}\bar{Q}}{A_{acc}\bar{C}\bar{A}}\right)\phi^T\delta\bar{\theta} + -\left(\bar{X}^T + \frac{\bar{C}A_{acc}+B_{acc}\bar{B}\bar{Q}}{A_{acc}\bar{A}}(\bar{X}_f - X_f)^T\right)\delta\bar{H}. \tag{A2-75}$$

Hence

$$M_{22} = -g_Q^{-1}(\bar{\Theta})E\left[\bar{X}\left(\bar{X}^T + \frac{\bar{C}A_{acc}+B_{acc}\bar{B}\bar{Q}}{A_{acc}\bar{A}}(\bar{X}_f - X_f)^T\right)\right]. \tag{A2-76}$$

If $B/A = B/A$ then $X_f = X_f$ and $M(\bar{\Theta}^*)$ becomes

$$M(\bar{\Theta}^*) = \begin{bmatrix} -g_\theta^{-1}(\bar{\Theta}^*)E[\bar{\phi}\bar{\phi}_f^T] & 0 \\ M_{21} & -g_Q^{-1}(\bar{\Theta}^*)E[\bar{X}\bar{X}^T] \end{bmatrix}. \tag{A2-77}$$

Since the adaptive system can only converge to the stable equilibrium points of the ODEs in Eqs. (A2-4) through (A2-7), $M(\bar{\Theta}^*)$ must be a stable matrix. Therefore since the eigenvalues of $-g_Q^{-1}(\bar{\Theta})E[\bar{X}\bar{X}^T]$ are in the left half plane, that implies that $1/\bar{C}$ must be SPR for the (1,1) entry to have all its eigenvalues in the left half plane. Note that $B/A = \bar{B}/\bar{A}$ is only a sufficient condition for $M(\bar{\Theta}^*)$ to be stable. This means that not all self-tuning adaptive systems necessarily satisfy this condition. Moreover, there could be other equilibrium points for which $M(\Theta)$ is also stable.

Proof of Part 5:

First factorize the zero polynomial as follows

$$\begin{aligned} B(q^{-1}) &= q^{-d}B'(q^{-1}), \\ B'(q^{-1}) &= B^{-}(q^{-1})B^{+}(q^{-1}), \end{aligned} \tag{A2-78}$$

where $B^{+}(q^{-1})$ and $B^{-}(q^{-1})$, respectively, contain all the roots of $B(q^{-1})$ which are strictly inside and outside the unit circle. Define

$$z(k) = \frac{B^{-*}(q^{-1})}{B^{-}(q^{-1})}y(k), \tag{A2-79}$$

where $1/B^{-}(q^{-1})$ can be interpreted as a bounded noncausal operator, and $B^{-*}(q^{-1})$ is Hurwitz and satisfies $\left|B^{-}(e^{j\omega})B^{-*}(e^{j\omega})\right| = 1$. Using Eq. (4-6) and the Diophantine equation

$$B^{-*}(q^{-1})C(q^{-1}) = A(q^{-1})S(q^{-1}) + q^{-d}B^{-}(q^{-1})R(q^{-1}), \tag{A2-80}$$

the following relation can be obtained

$$z(k) = \frac{S(q^{-1})}{B^{-}(q^{-1})}\omega(k) + q^{-d}\frac{A_{acc}(q^{-1})R(q^{-1}) + B^{-*}(q^{-1})B^{+}(q^{-1})\bar{Q}(q^{-1})}{A_{acc}(q^{-1})A(q^{-1})}\omega(k). \tag{A2-81}$$

Similarly, defining

$$\bar{z}(k) = \frac{\bar{B}^{-*}(q^{-1})}{\bar{B}^{-}(q^{-1})}y(k), \tag{A2-82}$$

and replacing the polynomials in Eq. (A2-81) with their estimates, the following relation can be obtained

$$\bar{z}(k) = \frac{\bar{S}(q^{-1})}{\bar{B}^{-}(q^{-1})}\omega(k) + q^{-d}\frac{A_{acc}(q^{-1})\bar{R}(q^{-1}) + \bar{B}^{-*}(q^{-1})\bar{B}^{+}(q^{-1})\bar{Q}(q^{-1})}{A_{acc}(q^{-1})\bar{A}(q^{-1})}\omega(k). \tag{A2-83}$$

Taking the expectation for $\bar{z}(k)$ and since $\bar{B}^{-*} = q^{\bar{n}_{B^{-}}}\bar{B}^{-}(q^{-1})$ is an unstable polynomial while $\bar{A}^{*} = q^{\bar{n}_A}\bar{A}(q^{-1})$ is stable, it leads to the following relation

$$E\{|\bar{z}(k)|^2\} = E\left\{\left|\frac{\bar{S}}{\bar{B}^-}\omega(k)\right|^2\right\} + E\left\{\left|q^{-d}\frac{A_{acc}\bar{R} + \bar{B}^{-*}\bar{B}^{+}\bar{Q}}{A_{acc}\bar{A}}\omega(k)\right|^2\right\}. \quad \text{(A2-84)}$$

If $\bar{Q}(q^{-1})$ is not restricted to be a FIR filter, then there exists a causal, stable transfer function $\bar{Q}_t^{\circ}(q^{-1})$ which minimizes $E\{|\bar{z}(k)|^2\}$ and $\bar{Q}_t^{\circ}(q^{-1})$ is such that

$$\frac{A_{acc}\bar{R} + \bar{B}^{-*}\bar{B}^{+}\bar{Q}_t^{\circ}}{A_{acc}\bar{A}} = 0. \quad \text{(A2-85)}$$

This results in $\bar{z}(k) = (\bar{S}(q^{-1})/\bar{B}^{-}(q^{-1}))\omega(k)$. From Eq. (A2-82), it can be seen that $\bar{Q}_t^{\circ}(q^{-1})$ also minimizes $E\{|y(k)|^2\} = E\left\{\left|((A_{acc}\bar{C} + \bar{B}\bar{Q})/A_{acc}A)\omega(k)\right|^2\right\}$ since the variance of $\bar{z}(k)$ is the same as that of $y(k)$. Now assuming that $\bar{Q}(q^{-1})$ is a FIR filter, it was shown in the proof of Theorem 2 that the FIR filter $\bar{Q}(q^{-1})$ minimizes $\left\|(A_{acc}C + BQ)/A_{acc}A\right\|_2$. Therefore, if $\hat{n}_Q$ is large enough, then $\bar{Q}(q^{-1}) \rightarrow \bar{Q}_t^{\circ}(q^{-1})$, since $\bar{Q}_t^{\circ}(q^{-1})$ is a causal, stable transfer function. It follows from Eq. (A2-85) that

$$\frac{A_{acc}\bar{R} + \bar{B}^{-*}\bar{B}^{+}\bar{Q}}{A_{acc}\bar{A}} \approx 0. \quad \text{(A2-86)}$$

Moreover, since $\bar{B}^{-}(q^{-1}) = B^{-}(q^{-1})$, then $z(k) = \bar{z}(k)$ and therefore

$$\left[\frac{S}{B^-} - \frac{\bar{S}}{\bar{B}^-}\right] + \left[q^{-d}\frac{A_{acc}R + B^{-*}B^{+}Q}{A_{acc}A}\right] \approx 0. \quad \text{(A2-87)}$$

Taking the norm of Eq. (A2-87) yields

$$\left\|\frac{S}{B^-} - \frac{\bar{S}}{\bar{B}^-}\right\|_2^2 + \left\|\frac{A_{acc}R + B^{-*}B^{+}Q}{A_{acc}A}\right\|_2^2 \approx 0. \quad \text{(A2-88)}$$

Noting that both $B^{-*}(q^{-1}) = q^{n_{B^-}}B^{-}(q^{-1})$ and $\bar{B}^{-*}(q^{-1}) = q^{\bar{n}_{B^-}}\bar{B}^{-}(q^{-1})$ are unstable polynomials, whereas $A^{*} = q^{n_A}A(q^{-1})$ is stable, it follows that

$$\frac{S}{B^{-}} - \frac{\bar{S}}{\bar{B}^{-}} \approx 0,$$
$$\frac{A_{acc}R + B^{-*}B^{+}Q}{A_{acc}A} \approx 0. \tag{A2-89}$$

Comparing Eq. (A2-89) and Eq. (A2-86), it can be concluded that $\bar{Q}(q^{-1})$ also minimizes $\left\|(A_{acc}C + BQ)/A_{acc}A\right\|_2$, i.e. $\bar{Q}(q^{-1}) = Q^{\circ}(q^{-1})$.

Proof of Part 6:

The proof of this part of Theorem 2 is given in [56].

APPENDIX B - PROGRAMS

B1. DSP PROGRAM OF THE ADAPTIVE ACCELEROMETER SERVO

The following code is a modified version of the DSP code used to run the adaptive accelerometer servo. The code was modified such that the variables more closely match the notation in this dissertation.

```
#include<intpt40.h>        // Realtime interrupt support functions.
#include<carrier.h>        // Pointers to the DSPLINK registers.
#include<stdio.h>

/* Function Prototypes */
void c_int04(void);        // Function prototype for ISR.

/* Define Constants */
#define NA 4               // Order of estimation of plant
                              denominator.
#define NB 4               // Order of estimation of plant numerator.
#define N  8               // Total order of estimation of plant
                              parameters.
#define Nq 10              // Total order of estimation of FIR
                              filter.
#define DELAY 1080         // Number of servo sectors to wait before
                              starting adaptive algorithm.
#define Nid 5400           //  Number of servo sectors to run the
                               plant estimation algorithm.
#define Betath 1
#define Betaq  1
#define lambdath 0.1
#define lambdaq  0.1

/* Define Gobal Variables */
float th[N],phi_th[N];     //  Parameter and regressor vector for
                               plant identification algorithm.
float h[Nq],phi_h[Nq];     //  Parameter and regressor vector for
                               FIR filter identification algorithm.
float phi_x[Nq];
float phi_c[Nq], phi_yhat[N];

long tempA, tmp1, tempD;
int  out, rec, cntdelay;
```

```
float yk,uk,yhat,tempC,tempB;
float yk_r,yhat_k;
float yhat_id, yhat_n, yhat_d;
float ethhat, eqhat;
float Fh, Fq;

/* Main Program */

main(void)
{
   /* Define Local Variables */

   volatile unsigned int temp;
   int i=0,j=0;
   float temp;

   /* Initialize the variable */

   for (i=0;i<N;i++)
   {
      th[i] = 0;
      phi_th[i] = 0;
      phi_yhat[i] = 0;
   }

for (i=0;i<Nq;i++)
   {
      h[i] = 0;
      phi_h[i] = 0;
      phi_c[i] = 0;
   }

   out     = 0; rec    = 0; cntdelay  = 0; id     = 1;
   yk_r    = 0; eqhat  = 0; ethhat    = 0; yhat_k = 0;
   yhat_id = 0; yhat_n = 0; yhat_d    = 0; yk     = 0;
   uk      = 0; Fth    = 1; Fq        = 1;

/* Need to perform an IACK instruction to allow external interrupts
   through to the ‘C40. */

   asm(“Push AR0”);
   asm(“Push DP”);
   asm(“LDI 030H,AR0”);
   asm(“LSH 16,AR0”);
   asm(“IACK *AR0”);
   asm(“POP DP”);
```

```
      asm("POP AR0");

      INT_DISABLE();             // Disable all interrupts.

   /* Set the ISR to be c_int04.  The function c_int04 will contain
      the C code to implement the adaptive algorithm. */

      install_int_vector((void *)c_int04, 0x04);
      load_iif(0x00B0);          // Set ISR to be level triggered.

      temp = *DM1_RESET;         // Reset Burr Brown board.

   /* Set ADCs to sample when external trigger occurs and DACs to
      trigger off internal clock. */

      *DM1_ROUTE = 0x000E0000;
      *DM1_AMELIA_CTRL = 0x00A20000;

   /* Set the ISR to run when ADCs are finished. */
      *DM1_INT_MASK = 0x00010000;

   /* Set the internal clock to 200kHz. */
      *DM1_INT_MASK = 0xFFC40000;
      *DM1_CONFIGURATION = 0x8DFF0000; // Load configuration.
      INT_ENABLE();                    // Enable all interrupts.

   /* Run main program until program is stopped from DSP emulator. */

      while(1) ;

   } /* end of main() */

   /* Interrupt Service Routines */

   void c_int04(void)

   /* This is the interrupt service routine for the IIOF1 interrupt.
    This corresponds to the input buffer from the A\D convertor
    being full. */

   {
   volatile long clear;

         clear = *DM1_INT_STATUS;  // Read Interrupt Status Register to
                                      clear.
         tempA = *DM1_CH0_IN_DATA; //Read Channel 0 Input Data Register
```

```
                                (PES).
         tempB = *DM1_CH1_IN_DATA; // Read Channel 0 Input Data Register
                                (ACC).
         out++;                   // Increment Trigger counter.

         /* Check to see if first Trigger, if so reset interrupt and wait
            for next Trigger to run parameter adaptation algorithms. */

         if (out == 2)
         {
            /* Read in PES from Channel 0 (A) */
            temp  = tempA>>16;             // Shift down 16-bits.
            yk = -(float)(temp)*3/(0x7FFF);// Multiply by ADC gain.

            /* Read in Accelerometer signal from Channel 1 (B) */
            temp  = tempB>>16;             // Shift down 16-bits.
            ak = -(float)(temp)*3/(0x7FFF);// Multiply by ADC gain.

            /* Calculate repetitive component in both PES and ACC
               signals before implementing adaptive servo.*/

            if (!rdone)
            {
               if (k<100*54)
               {
                  if (j==54) j = 0;
                  rep[j]  = rep[j]   + yk;
                  rep_a[j]= rep_a[j] + ak;
                  j++;
                  k++;
               }

               if (k==100*54)
               {
                  for(i=0;i<54;i++)
                  {
                     rep[i] = rep[i]/100;
                     rep_a[i] = rep_a[i]/100;
                     rdone = 1;
                  }
               }
            }
            else
            {
               if (m==54) m = 0;       // Substract out repetitive
                                          components.
```

```
yk_r = yk - rep[m];
ak   = ak - rep_a[m];
m++;
if (cntdelay < DELAY)   // Wait certain DELAY before
                           starting adaptive servo.
{
   cntdelay++;
   tempC = (yk_r/3*32767);
   tempD = ((long)(tempC))<<16;
   *DM1_CH0_OUT_DATA = tempD; // Output data to channel A
}
else
{
if (id<Nid)
{
   /* DO parameter identification algorithm first */

   /* Calculate the random signal to send to VCM. */

   tempB = (float)(rand());
   uk = ((tempB/RAND_MAX)*5-2.0);

   /* Send out the control signal to Channel 1 (B). */
   tempC = (uk/3*32767);      // Multiply by DAC gain.
   tempD = ((long)(tempC))<<16;// Shift left 16 bits.
   *DM1_CH1_OUT_DATA = tempD;  // Output  to channel B

   /* Send out the PES to Channel 0 (A). */
   tempC = (yk_r/3*32767);
   tempD = ((long)(tempC))<<16;// Shift left 16 bits.
   *DM1_CH0_OUT_DATA = tempD;  // Output  to channel A

   /* Do the Plant Estimation Algorithm. */

   /* Calculate the effect of the controller using the
      estimated plant parameters, Ahat and Bhat. */

   /* Calculate the denominator part first. */

   yhat_d = (th[0]*phi_th[0] + th[1]*phi_th[1] +
            th[2]*phi_th[2] + th[3]*phi_th[3]);

   /* Calculate the numerator portion. */

   yhat_n = (th[4]*phi_th[4] + th[5]*phi_th[5] +
           th[6]*phi_th[6] + th[7]*phi_th[7]);
```

```
      yhat_id  = yhat_n + yhat_d;

      /* Do the plant estimation algorithm. */
      /* Calculate the FIR estimation error */
      ethhat = yk_r - yhat_id;

      /* Update the FIR filter parameter vector */
      th[0]  = th[0] + Betath*phi_th[0]*ethhat/Fth;
      th[1]  = th[1] + Betath*phi_th[1]*ethhat/Fth;
      th[2]  = th[2] + Betath*phi_th[2]*ethhat/Fth;
      th[3]  = th[3] + Betath*phi_th[3]*ethhat/Fth;
      th[4]  = th[4] + Betath*phi_th[4]*ethhat/Fth;
      th[5]  = th[5] + Betath*phi_th[5]*ethhat/Fth;
      th[6]  = th[6] + Betath*phi_th[6]*ethhat/Fth;
      th[7]  = th[7] + Betath*phi_th[7]*ethhat/Fth;

      /* Update the regressor vector for the estimated
       PES under the influence of just the c+ontrol. */

      phi_th[7] = phi_th[6];
      phi_th[6] = phi_th[5];
      phi_th[5] = phi_th[4];
      phi_th[4] = uk;
      phi_th[3] = phi_th[2];
      phi_th[2] = phi_th[1];
      phi_th[1] = phi_th[0];
      phi_th[0] = -yk_r;

      /* Update the FIR filter adaptation gain */
      Fth    = Fth + lambdath*(phi_th[0]*phi_th[0] +
                               phi_th[1]*phi_th[1] +
                               phi_th[2]*phi_th[2] +
                               phi_th[3]*phi_th[3] +
                               phi_th[4]*phi_th[4] +
                               phi_th[5]*phi_th[5] +
                               phi_th[6]*phi_th[6] +
                               phi_th[7]*phi_th[7]);

      id++;
      }
   else           // Do FIR filter adaptation and control
                     after the plant estimation is done.
   {
      uk = (h[0]*ak + h[1]*phi_c[0] + h[2]*phi_c[1] +
           h[3]*phi_c[2] + h[4]*phi_c[3] + h[5]*phi_c[4] +
           h[6]*phi_c[5] + h[7]*phi_c[6] + h[8]*phi_c[7] +
```

```
     h[9]*phi_c[8]);

/* Limit the maximum and minimum value of the control
   signal to prevent damage to the VCM driver. */

if (uk > 1) uk = 1;
if (uk < -1) uk = -1;

/* Send out the control signal to Channel 1 (B). */
tempC = (uk/3*32767);       // Multiply by DAC gain.
tempD = ((long)(tempC))<<16;//  Shift left 16 bits.
*DM1_CH1_OUT_DATA = tempD;  // Output data to channel B

/* Send out the PES to Channel 0 (A). */
tempC = (yk_r/3*32767);    // Multiply by DAC gain.
tempD = ((long)(tempC))<<16;// Shift left 16 bits.
*DM1_CH0_OUT_DATA = tempD;  // Output  to channel A

/*  Update the Vector of past accelerometer
    values for the controller */

phi_c[8] = phi_c[7];
phi_c[7] = phi_c[6];
phi_c[6] = phi_c[5];
phi_c[5] = phi_c[4];
phi_c[4] = phi_c[3];
phi_c[3] = phi_c[2];
phi_c[2] = phi_c[1];
phi_c[1] = phi_c[0];
phi_c[0] = ak;

/* Calculate the effect of the controller using the
   estimated plant parameters, Ahat and Bhat. */

/* Calculate the denominator part first. */

yhat_kd = (th_id[0]*phi_yhat[0] +
         th_id[1]*phi_yhat[1] +
         th_id[2]*phi_yhat[2] +
         th_id[3]*phi_yhat[3]);

/* Calculate the numerator part. */

yhat_kn = (th_id[4]*phi_yhat[4] +
         th_id[5]*phi_yhat[5] +
         th_id[6]*phi_yhat[6] +
```

```
                th_id[7]*phi_yhat[7]);

yhat_k  = yhat_kn + yhat_kd;
/* Update the regressor vector for the estimated PES
   under the influence of just the control signal. */

phi_yhat[7] = phi_yhat[6];
phi_yhat[6] = phi_yhat[5];
phi_yhat[5] = phi_yhat[4];
phi_yhat[4] = uk;
phi_yhat[3] = phi_yhat[2];
phi_yhat[2] = phi_yhat[1];
phi_yhat[1] = phi_yhat[0];
phi_yhat[0] = -yhat_k;

/*  Calculate the estimate of disturbance dhat */
dhat = yk_r - yhat_k;

/* Do the FIR Filter algorithm */
/* Pre-filter by the accelerometer signal
   by the estimated plant parameters */
xd_k =  (th_id[0]*phi_x[0] + th_id[1]*phi_x[1] +
       th_id[2]*phi_x[2] + th_id[3]*phi_x[3]);
xn_k =  (th_id[4]*phi_xn[4] + th_id[5]*phi_xn[5] +
       th_id[6]*phi_xn[6] + th_id[7]*phi_xn[7]);
x_k  =  xd_k + xn_k;

/* Calculate the FIR estimation error */
eqhat = dhat - (phi_x[0]*h[0] + phi_x[1]*h[1] +
            phi_x[2]*h[2] + phi_x[3]*h[3] +
            phi_x[4]*h[4] + phi_x[5]*h[5] +
            phi_x[6]*h[6] + phi_x[7]*h[7] +
            phi_x[8]*h[8] + phi_x[9]*h[9]);

/* Update the regressor vector for calculation of x.*/

phi_xn[7] = phi_xn[6];
phi_xn[6] = phi_xn[5];
phi_xn[5] = phi_xn[4];
phi_xn[4] = ak;
phi_x[9] = phi_x[8];
phi_x[8] = phi_x[7];
phi_x[7] = phi_x[6];
phi_x[6] = phi_x[5];
phi_x[5] = phi_x[4];
phi_x[4] = phi_err[3];
```

```
                    phi_x[3] = phi_x[2];
                    phi_x[2] = phi_x[1];
                    phi_x[1] = phi_x[0];
                    phi_x[0] = -x_k;

                    /* Update the FIR filter parameter vector */

                    h[0]  = h[0] + Bethaq*phi_x[0]*eqhat/Fq;
                    h[1]  = h[1] + Bethaq*phi_x[1]*eqhat/Fq;
                    h[2]  = h[2] + Bethaq*phi_x[2]*eqhat/Fq;
                    h[3]  = h[3] + Bethaq*phi_x[3]*eqhat/Fq;
                    h[4]  = h[4] + Bethaq*phi_x[4]*eqhat/Fq;
                    h[5]  = h[5] + Bethaq*phi_x[5]*eqhat/Fq;
                    h[6]  = h[6] + Bethaq*phi_x[6]*eqhat/Fq;
                    h[7]  = h[7] + Bethaq*phi_x[7]*eqhat/Fq;
                    h[8]  = h[8] + Bethaq*phi_x[8]*eqhat/Fq;
                    h[9]  = h[9] + Bethaq*phi_x[9]*eqhat/Fq;

                    /* Update the FIR filter adaptation gain */

                    Fq      = Fq + lambdaq*(phi_x[0]*phi_x[0] +
                                        phi_x[1]*phi_x[1] +
                                        phi_x[2]*phi_x[2] +
                                        phi_x[3]*phi_x[3] +
                                        phi_x[4]*phi_x[4] +
                                        phi_x[5]*phi_x[5] +
                                        phi_x[6]*phi_x[6] +
                                        phi_x[7]*phi_x[7] +
                                        phi_x[8]*phi_x[8] +
                                        phi_x[9]*phi_x[9]);
                    }
               }
               out = 0;    //  Reset Trigger count of done adaptive scheme.
          }

}
```

B2. LATTICE CHIP PROGRAM

The following code is the Lattice chip program used to implement the state transition diagram given in Section 3.2.2.

```
MODULE TRIGGER
```

```
TITLE 'Trigger for DSP A/D'
"Define the Inputs to the Lattice Chip
"Inputs.
    clock          pin; " 10 MHz external clock signal
    D11..D0         pin;" Inputs connected to DIP switch to set the
                        " delay values.
    high_c, low_c  pin; " Comparitor output signals which determine
                        " when the servo sector is reached.
"Outputs.
    AD_trig        pin istype 'com, buffer';  " Trigger output signal
                                              " used to trigger the ISR for
                                              " the C40.

    S2..S0         pin istype 'reg, buffer';  " Holds current state.

"Nodes.
    C8..C0         node istype 'reg, buffer'; " Delay counter.

"Set declarations.
    count  = [C8..C0];                  " Delay counter set.
    st_reg = [S2..S0];                  " State registers.
    delay1 = [0,D7..D4, 1, 1, 1, 1];    " First delay time.
    delay2 = [0,D3..D0, 1, 1, 1, 1];    " Second delay time.
    delay3 = [0,D11..D8,1, 1, 1, 1];    " Third delay time.

   " Assign grey code values to the states to minimize the occurance
   " of glitches.

   ST0 = 0; ST1 = 1; ST2 = 3; ST3 = 2; ST4 = 6; ST5 = 4;
   ST6 = 5; ST7 = 7;

Equations
    count.clk  = clock;" Both the count and state registors.
    st_reg.clk = clock;" are updated with the clock signal.

State_Diagram st_reg;
   " In state ST0, wait for high_c (high comparator) to transition.
   " high.

   State ST0:

      AD_trig = 0;
      count := 0;
      if (high_c) then ST1;" If high_c transitions high, go to ST1
      else ST0;            " else stay in ST0.
```

```
      " State ST1 waits for low comparator and prepares delay counter.

      State ST1:

         AD_trig = 0;
         if (low_c) then ST2 with count := 0;" If low_c transitions
         else ST1;                             " high, go to ST2 else
                                               " stay in ST1.

      " State ST2 runs first delay counter.

      State ST2:

         AD_trig = 0;
         if (count == delay1) then ST3 with count := 0;
         else ST2 with count := count + 1;" Wait for delay1 before
                                          " going to ST3.

      " In state ST3 send first low pulse for a fixed time.

      State ST3:

         AD_trig = 1;
         if (count == delay2) then ST4 with count := 0;
         else ST3 with count := count + 1;" Wait for delay2 before
                                          " going to ST4.

      " In state ST4 send pulse high again.

      State ST4:

         AD_trig = 0;
         if (count == delay3)  then ST5 with count := 0;
         else ST4 with count := count + 1;" Wait for delay3 before
                                          " going to ST5.

      " In state ST5 send second low pulse for a fixed time.

      State ST5:

         AD_trig = 1;
         if (count == delay2) then ST0 with count := 0;
           else ST5 with count := count + 1;" Wait for delay2 before
                                            " going to ST0.

   END
```